PROPAGATION OF LASER RADIATION THROUGH ATMOSPHERIC TURBULENCE

by

James R. Dunphy

Submitted in Partial Fulfillment
of the Requirements for the
Degree of Doctor of Philosophy
at the
Oregon Graduate Center

September 1974

APPROVAL SHEET

This Ph. D. dissertation has been examined and approved by the following persons:

J. Fred Holmes
Associate Professor
Examining Committee Member

G. J. Throop
Assistant Professor
Examining Committee Member

J. Richard Kerr
Professor
Thesis Advisor
Examining Committee Member

C. McIntyre
Assistant Professor
Student Program Committee Member
Examining Committee Member

TABLE OF CONTENTS

TABLE OF CONTENTS (Cont'd)

PAGE

TABLE OF CONTENTS (Cont'd)

PAGE

ABSTRACT

This study is concerned with the propagation of visible and middle infra-red laser radiation through the turbulent atmosphere. An experimental approach was used to investigate the spatial and temporal disturbances induced on a laser's intensity distribution. The measurements were made for propagation over very homogeneous paths so that the results could be compared directly with available theories. Included are unique measurements of (I) the scintillation of quasi-point laser sources for large integrated-path turbulence, (II) the propagation effects of a large, passive, focused beam wave, and (III) the characteristics of a large, focused beam wave which has had atmospherically induced wander cancelled through the use of a reciprocity tracker.

The large integrated-path turbulence measurements allowed detailed examination of saturation phenomena. The log-amplitude variance at 10.6 μm was observed to saturate for the first time. Further, the covariance function at 4880 Å was discovered to be drastically modified by conditions of strong turbulence. It was experimentally established that the correlation at short distances was drastically reduced with the onset of saturation. Concurrently, a residual correlation appeared at large distances. This change in the covariance function resulted in aperture averaging for "point" receivers, and caused the bandwidth of the

electronic processing equipment (which was quite adequate under conditions of weak turbulence) to be much too narrow in this case. Taking into consideration the spatial and temporal filtering, the experimental measurements were found to be in good agreement with recent theoretical models for optical propagation subject to strong atmospheric perturbations.

When the large, passive focused beam wave was studied at 4880 Å, no advantage was found over the fade characteristics of a quasi-point source. In fact, during weak turbulence the beam wave fading was worse than that of the point source. This resulted from atmospherically induced wander which randomly steered the beam (nearly diffraction-limited over a 1.4 km path) about the receiver in the target plane. This fact points out a serious deficiency in the first-order theoretical approaches to beam wave propagation: the wander phenomenon is not included in their descriptions. In addition, later experiments showed that scintillation measurements on the main lobe of a beam wave provided negligible transmitter aperture averaging, even when wander was cancelled. Hence it is suggested that large, beam wave transmitter aperture averaging cannot be achieved at visible wavelengths for reasonable apertures and path-lenths.

Subsequently, a more comprehensive, unified theory was investigated experimentally. This theory is the extended Huygens-Fresnel method, and its analysis applies not only to beam wave propagation but also to

imaging through turbulence and the operation of optical heterodyne receivers in the atmosphere. Data related to the on-axis mean irradiance and fading for the passive beam and for the beam with wander cancellation was collected at 6328 Å over a 1.6 km path. Comparison of this data with detailed numerical and assymptotic evaluations of the extended Huygens-Fresnel predictions confirmed fundamental dependencies on the ratio of the gaussian beam diameter to the transverse coherence scale size, D_g/ρ_o. The results suggest that D_g/ρ_o of order unity is a special combination of beam-geometry and turbulence conditions that generates maximum beam wandering. Consequently, tracking provided (1) a maximum increase in the on-axis mean irradiance and (2) a maximum decrease in the fading during this condition. Furthermore, this experiment verified that the on-axis mean irradiance and fading are nearly universal functions of D_g/ρ_o.

These results are extremely useful when considering applications utilizing lasers, imaging, or optical heterodyne receivers over horizontal and vertical paths through the atmosphere.

ACKNOWLEDGMENTS

I would like to express my most sincere appreciation and love to my family, each of whom sacrificed much so that this goal might be achieved.

In addition, I thank Dr. J. Richard Kerr for his energy and direction as supervisor of my program. He also secured the grants from the Advanced Research Projects Agency of the Department of Defense (Contract numbers N00014-68-A-0461-0001, F30602-72-C-0470, and F30602-74-C-0082) which supported this work.

LIST OF FIGURES

LIST OF FIGURES (cont'd)

LIST OF FIGURES (cont'd)

LIST OF FIGURES (cont'd)

LIST OF FIGURES (cont'd)

LIST OF TABLES

INTRODUCTION

When one is faced with the task of designing an optical system operating in the atmosphere, regardless of the application, there are two primary quantities of interest: the mean power that can be delivered to the target, $\bar{P}_t$, and the mean square fluctuation in that power, σ_p^2. In general the mean power at the target can be described as

$$\bar{P}_t = P_o \cdot T_o \cdot T_1 \cdot T_2 \cdot T_3 \cdot T_4 \qquad (1)$$

where P_o is the initial power of the transmitter, T_o is the loss due to optical components in both the receiver and the transmitter, and T_1 takes into account the relative sizes of the receiving and transmitting apertures. T_2 relates to absorption by the atmosphere, T_3 considers power loss due to beamspread induced by clear air turbulence, and T_4 adjusts the calculation for power reduction due to beamspread caused by aerosol scattering. For propagation over a short (1-4 miles) path near the ground the main difficulty encountered is the mean power loss due to turbulence induced beamspread, T_3.

The ripple about this average power is estimated by

$$\sigma_p^2 = A_1 \sigma_{st}^2 + A_2 \sigma_{sc}^2 \qquad (2)$$

In this expression σ_{st}^2 and σ_{sc}^2 are the mean square fluctuations due to atmospherically induced beam wander and scintillation, respectively.

Here, $A_1 = 0$ and $A_2 = 1.0$ for point transmitters and receivers and are different for finite or complicated aperture elements.

The importance of the effect of these parameters can be illustrated by considering lasers in optical communication systems. The laser brings with it the potential of a wide transmission bandwidth that could yield very high information rates.[1,2] A prominent factor inhibiting the realization of wideband laser systems is the information capacity of the atmospheric channel through which the optical carrier propagates. Shannon[3] explains that the information capacity of a channel is

$$C = W \log_2 \left(\frac{P + N}{N} \right) \qquad (3)$$

where C is given in bits per second, W is the transmission bandwidth, P is the average power at the receiver, and N is the noise added to the signal. From this expression it can be seen that the advantage of a wide transmission bandwidth can be defeated if the channel induces significant reductions in P and increases in N. Mechanisms for these detrimental effects on a laser communications channel through the atmosphere do exist as suggested by the parameters of Eqs. 1 and 2. Detail on how the atmospheric channel increases the bit error rate can be found as indicated by Fried and Schmeltzer.[4] Adaptive or diversity techniques[5] promise schemes for counteracting the atmosphere's degradation of channel capacity. However, the atmospheric channel must be fully characterized in terms

of its statistical effects on the laser beam before these enhancement methods can be properly applied. This characterization, that is the knowledge of $\bar{P}_t$ and σ_p^2 , requires intimate coupling of theoretical and experimental investigations.

The theoretical representation of the atmospheric propagation channel is obtained upon combination of two models: a model for the clear, turbulent atmosphere, and a propagation model for electromagnetic radiation. The propagation model is derived by considering Maxwell's equations. A vector wave equation is generated which is specialized to a reduced scalar wave equation.[6] This wave equation contains a parameter that ties together the medium and the EM wave. It is the index of refraction, n. In the atmosphere this index of refraction changes dynamically with time.

The model for the atmospheric changes in index of refraction is usually generated in a spatial domain rather than a time domain. The spatial modulation of the index of refraction is caused by a spatially changing temperature and humidity field. When the random distribution of n is translated through the propagation path, the perturbations in the EM field's amplitude and phase should be calculable.

Details for these calculations are reviewed by Wheelon,[7] Chernov[8] and Tatarskii[9] for the period prior to 1960. Since these, Tatarskii,[10] Strohbehn,[11] Brown,[6] and Lawrence and Strohbehn[12] have provided

reviews for work up to 1970. The array of directions for calculating details of the intensity distribution is illustrated by Fig. 1 and is the result of various approximations related to the field of the EM wave and/or the strength of the index of refraction fluctuations.

One of the most successful theories has been the method of smooth perturbations, commonly called the Rytov approach. Application of this scheme has led to solutions for the propagation of plane and spherical waves, as well as finite laser beams. However, under conditions of strong atmospheric perturbation, this theoretical approach breaks down. It is the goal of this dissertation to (1) fully characterize the extent of the breakdown of the method of smooth perturbations via experimental techniques; (2) to investigate the ability of a finite laser source to overcome the optical carrier degradation experienced by point sources; and (3) to design and operate an active transmitter directed towards cancelling a distinct atmospheric effect (wander) on finite sources. In particular, the accomplishment of (3) will provide unique measurements of the statistical properties of a finite laser source that has propagated through the turbulent atmosphere.

Information for the achievement of this goal is presented in three major sections: (I) optical propagation subject to strong turbulence (point source), (II) propagation of a passive, focused beam wave, and (III) propagation of a focused beam wave with wander cancellation.

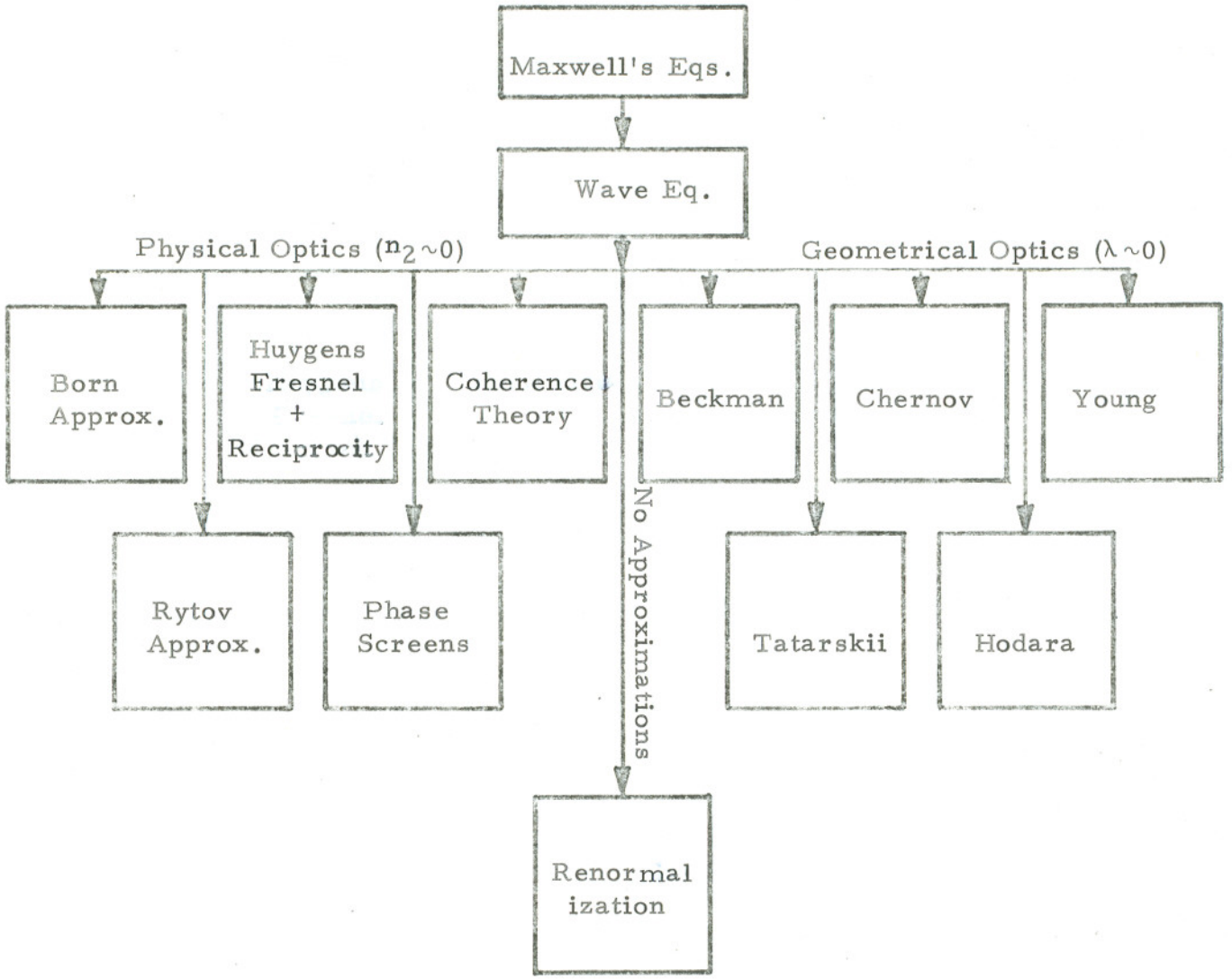

Figure 1. Array of theoretical directions. The work done within the geometrical optics limit is listed by authors utilizing various techniques. Physical optics methods actually apply very distinctive models which are discussed by many authors. The renormalization techniques are sufficiently general to preclude approximations. See text for references.

CHAPTER I. OPTICAL PROPAGATION SUBJECT TO STRONG TURBULENCE (POINT SOURCE)

INTRODUCTION

The propagation characteristics of classical wavefronts (plane, spherical) are well understood for the case of weak turbulence. The successful theoretical description is called the Rytov approximation or the method of smooth perturbations. The log-amplitude variance, covariance and probability distribution have been indicated as fundamental quantities for theoretical and experimental investigations.[9] The log-amplitude variance, σ_χ^2, increases proportionally with the strength of turbulence.[10,13,14] Normalized curves detailing the log-amplitude covariance function are provided by Fried[13,14] and are not expected to depend on the strength of turbulence. In addition the probability distribution of the log-amplitude is found to be gaussian.[10]

Experimental investigations[15,16] confirm the validity of the above predictions only if the theoretical value of σ_χ^2 is less than 0.3-0.5. Earlier experimental efforts to characterize the statistics of the breakdown region have been questioned due to possible bias induced by either inhomogeneous propagation paths or finite beam wave effects.[17]

It is the goal of this chapter to describe large path-integrated turbulence propagation measurements that are free from the influences

mentioned above. The results of these experiments will serve as a test for the extensions of turbulent propagation theory to conditions of strong perturbation. A brief summary of these extensions follows.

We note here that these experiments were completed in Oct. 1972 and the results published in Mar. 1973.[18] Hence Section I.A. provides a summary of theory available up to the publication time of the experimental results. Section I.B. summarizes the experimental results, while Section I.C. provides a comprehensive update of extensions to the theory of propagation under strong turbulence.

I.A. THEORY FOR THE STRONG TURBULENCE REGIME

In the introduction to this chapter, we indicated that the method of smooth perturbations breaks down for strong fluctuations in the atmosphere's index of refraction, or for large path-accumulated turbulence levels. In answer to this failure there is work in the literature proposing new approaches, which will not be hindered by limits on the strength of perturbations. These methods can be lumped into four basic groups: (1) renormalization techniques, (2) direct moment equation techniques, (3) modified versions of the method of smooth perturbations and (4) heuristic or conceptual models. Each is now introduced. A summary of their implications on experimental work is given later.

One of the earliest extensions of propagation theory under strong perturbations was the renormalization method.[15,19-25] The goal of this procedure is to obtain the optical field while maintaining all terms in the perturbation expansion, rather than truncating the series solution after the second term (the Born and Rytov approximations). Keeping track of the interaction of series terms when calculating the field and its higher moments requires a very efficient cataloguing device called diagrammatic summation. Renormalization methods promise complete solution of the propagation problem for virtually any wavefront; however, the resulting expressions are so involved that many approximations are required to provide useful results. In addition the complication of this route provides little feedback for physical reasoning.

In contrast to the renormalization schemes, moment equation techniques tend to yield to physical reasoning or insight and produce useable expressions. Under the broad heading of moment techniques is included theoretical methods which take into consideration the accumulative effect of the optical field propagating through perturbing slabs of atmosphere. From a basic reduced wave equation, partial differential equations are derived which are satisfied by high order moments of the optical field[26-29] or mutual coherence function.[30-33] Methods utilizing Huygens-Fresnel expressions[34,35] and transport theory[36,37] are also moment techniques, all of which are expected to produce integral solutions for high order

moments that are valid regardless of the atmosphere's strength of turbulence or the propagation distance (strong accumulative turbulence).

The third approach to saturation is to make a direct modification to the method of smooth perturbations. In one case Tatarskii[38] extends the Rytov method to include the third order of the perturbation series. On the other hand, Ishimaru[39] is able to produce equations exhibiting saturation by taking into account the inhomogeneity of the turbulent field. The result is accomplished by considering transverse correlation in the perturbing medium, rather than just inhomogeneity in the direction of propagation.

Finally, there are heuristic and physical arguments dealing with the problem of saturation. For instance, Torrieri and Taylor[40,41] present a phasor model. Young[42-44] suggests spatial filtering and MTF changes as giving rise to the saturation phenomenon, while Kerr[17] presents dimensional arguments.

Probably one of the most exciting results of theoretical extensions developed to meet the needs of the saturation problem is the equivalence of the renormalization and the moment techniques.[45,46] This fact encompasses many approaches as mentioned above and lends support to the potential validity of the net predictions. These predictions are reviewed in the following subsections.

I.A.1. Log-Amplitude Variance

One of the primary theoretical results of interest is the log-amplitude variance, σ_χ^2. For the most part, the renormalization proponents can only show that their techniques work in the limit of weak perturbation.[21] Two exceptions, due to deWolf, do give specific information. For instance, deWolf[15] shows that the log-intensity variance, $\sigma_{\ln I}^2$, has the form

$$\sigma_{\ln I}^2 = \ln[\,2 - e^{-\sigma_{\ln I_{Rytov}}^2}\,] \qquad (4)$$

ln 2 is the saturation value obtained in the limit of strong turbulence, that is, as $\sigma_{\ln I_{Rytov}}^2 \to \infty$, where he defines $\sigma_{\ln I_{Rytov}}^2$ as the Rytov prediction for the variance of the log irradiance. This implies $\sigma_\chi^2 = 0.17$. In a later effort, deWolf[25] distinguishes three regions; the first corresponds to the Rytov result. Then σ_χ^2 saturates to a peak of order unity at a theoretical Rytov value dependent on the optical wavelength and the inner scale of the turbulent spectrum. In region two, just beyond the saturation peak, σ_χ^2 supersaturates and decreases as the theoretical Rytov log-amplitude variance to the (-1/6) power. Finally, in the third region (which may not be measureable for optical experiments) the curve of σ_χ^2 vs. the Rytov value humps back up to the original saturation value of order unity.

Within the group applying moment equation techniques, Sancer and Varvatsis[26] found that the variance in the log-irradiance ($\sigma_{\ln I}^2$) should

peak to unity and then supersaturate smoothly to an assymptote of $\ln 2$. In terms of the log-amplitude variance this calls for a peak of 0.25 and a final assymptote of 0.17. In a two-dimensional analysis Brown[29] shows that the normalized variance in the linear irradiance, σ_I^2, peaks at 1.3 and supersaturates to 1.0. When these values are translated to the log-amplitude terminology σ_χ^2 peaks at 0.21 with a final assymptote of 0.17. In contrast to deWolf's renormalization result of a wavelength dependent saturation condition, Brown finds saturation to take place independent of wavelength. Interestingly, Brown does find that the approach to the saturation assymptote can involve a peak or be smooth depending on the optical wavelength and the outer scale of the turbulent spectrum. In a third moment-technique-related analysis, Tatarskii[31] finds saturation dependent on two scales that are related to transverse correlation in the optical field, but the physical significance of these is not totally clear.

The Tatarskii[38] modification to the method of smooth perturbation also gives an assymptote to the log-amplitude variance for infinite strength of turbulence, but its value is dependent on an undetermined constant. deWolf[15] makes many comments on the application of Tatarskii's final expression.

Details already given above are supported by the heuristic treatments. Torrieri and Taylor[40,41] find that the $\sigma_{\ln I}^2$ saturates at 0.69 ($\sigma_\chi^2 = 0.17$). Kerr's dimensional analysis confirms Brown's result that saturation is wavelength independent.

I.A.2. Log-Amplitude Covariance

The only development providing significant detail related to the log-amplitude covariance as a function of increasing turbulence is Brown.[29] This two dimensional analysis yields that the initial width of correlation decreases drastically for increasing turbulence. Concurrent with the initial decorrelation is a growth in residual correlation at large separations. This may be a drastic enough effect to imply the existence of two correlation scales. The implications are that the log-amplitude covariance scale size shrinks while large patches of correlated energy grow.

I.A.3. Log-Amplitude Probability Distribution

Heuristic efforts indicate that the log of the intensity or amplitude is normally distributed prior to saturation, while in actual saturation a Rayleigh distribution is suggested. Others agree with this distribution during saturation.[15,21,22,26] deWolf[25] produces further detail by showing that the log-intensity (or log-amplitude) is normally distributed before and during the initial stages of saturation. But in the "ultra-saturated" state, the intensity is exponentially distributed (amplitude is Rayleigh distributed). Strohbehn and Wang[33] afford a method to theoretically test for log-normality of the field's amplitude fluctuations but could not make an exact conclusion . Tatarskii's modification of the method of smooth perturbation assumes the amplitude to be log-normal. Finally deWolf[15,23] demands that good

data beyond the 10-90% region of the cumulative probability distribution is required for a definitive conclusion based on experimental techniques.

With these characteristic indicators of the scintillation statistics during saturated conditions, the following experiments were performed.

I.B. SCINTILLATION MEASUREMENTS FOR LARGE INTEGRATED-PATH TURBULENCE

The purpose of these experiments was to measure the properties of scintillations over the longest, lowest path that can be reasonably achieved, in order to encounter the highest-possible integrated-path turbulence level. The experiments were conducted with simultaneous coincident virtual-point sources at visible and middle-infrared wavelengths. The measurements are itemized in Table I and include turbulence strength, meteorological parameters, and scintillation statistics. The turbulence and scintillation quantities are defined in Ref. 12.

The general instrumentation is described in Ref. 16 and the experimental parameters are summarized in Table II. The long-term vertical beam bending due to thermal gradients was quite significant. Hence, the transmitter site incorporated a 7-m-high steel tower sunk into a massive concrete base, isolated from the instrument shack, with a provision for changing the outgoing-beam height and vertical angle. The output window was a movable BaF flat.

Table I. Experimental Measurements

Strength of turbulence (C_n^2) from microthermal probes
Vertical temperature gradient
Wind velocity
Log-amplitude variance
Log-amplitude covariance
Log-amplitude probability distribution
Scintillation spectrum
Receiver-aperture smoothing

Table II. Experimental Parameters

Path length: 6.0 km
Path description: Farm land, flat to within $\pm$ 0.5 m
Transmitter height: 6.1 m
Receiver height: 3.5 m
Wavelengths (simultaneous, coincident): 4880 Å, 10.6 μm
Transmitter-beam configuration: Virtual-point sources (Fresnel number $<10^{-3}$)
Receiver aperture: 6 mm
Receiver dynamic range: >80 dB
Receiver averaging time: 60 s
Aperture-smoothing receiver: 0.6-32 cm
Resolution of spectral measurements: 1 Hz
Receiver bandwidth: 1 kHz
Microthermal-probe separation for C_n^2: 10 cm
Microthermal-probe height: 1.8 m
Microthermal averaging time: 300 s

Initial beam steering employed 4880 Å by use of a coaxial sighting telescope and precision mirror rotators, including a remote-control unit on the tower-mounted output mirror. The 10.6-μm beam was then made precisely coaxial with the visible beam; the atmospheric refraction was found to be substantially the same at both wavelengths. The effects of atmospherically induced short-term wander were circumvented by diverging the beams sufficiently to make their radii at the receiver about an order of magnitude greater than the expected wander. Under very low turbulence the beam radii were measured to be approximately 2.5 m and 7.5 m at 4880 Å and 10.6 μm, respectively.

The major objectives of these experiments were measurement of saturation[12] of log-amplitude variance and related effects at 10.6 μm, investigation of scintillation statistics at a visible wavelength far into the saturation region, and examination of large-integrated-path turbulence effects on scintillation correlation scales and hence, receiver-aperture smoothing. In the following sections, we discuss log-amplitude variance, covariance, scintillation spectra, probability distributions, and receiver aperture smoothing.

I.B.1. Log-Amplitude Variance

Experimental log-amplitude variances σ_E^2 were obtained from probability distributions. A typical diurnal behavior for a cloudless day

is shown in Fig. 2. The unusually high values of σ_E^2 for 4880 Å in the early morning were due to poorly developed turbulence structure,[16] and there is evidence that the presence of light ground fog during that period further increased these anomalous fluctuations. The data show that for this very-long low-path configuration the variance at 4880 Å was nearly always saturated. As discussed below, the lower extreme of these variances is not indicative of an asymptote for high turbulence. Outside of the anomalous-turbulence period, the 10.6-μm variances were seen to saturate in midmorning.

The variances measured at 10.6 μm are shown in Fig. 3 vs the strength of turbulence taken at a height of 1.8 m, and saturation is clearly indicated. As discussed below, the abscissa is not highly meaningful without a correction due to variable beam refraction. The saturation level appears to be somewhat lower than the 0.6 value typical of shorter wavelengths,[12,16] according to a recent theoretical treatment, this may very likely be due to the effects of the finite outer scale of turbulence.[29] When turbulence scales may be neglected, the saturation level is expected to be wavelength independent.[16]

Similar data are given in Fig. 4 for 4880 Å. The logarithmic slope beyond saturation is near the (-1/6) value predicted by deWolf.[25] However, as discussed below and in Secs. 2-5, corrections are required for beam refraction and covariance scale effects, and the agreement is probably fortuitous.

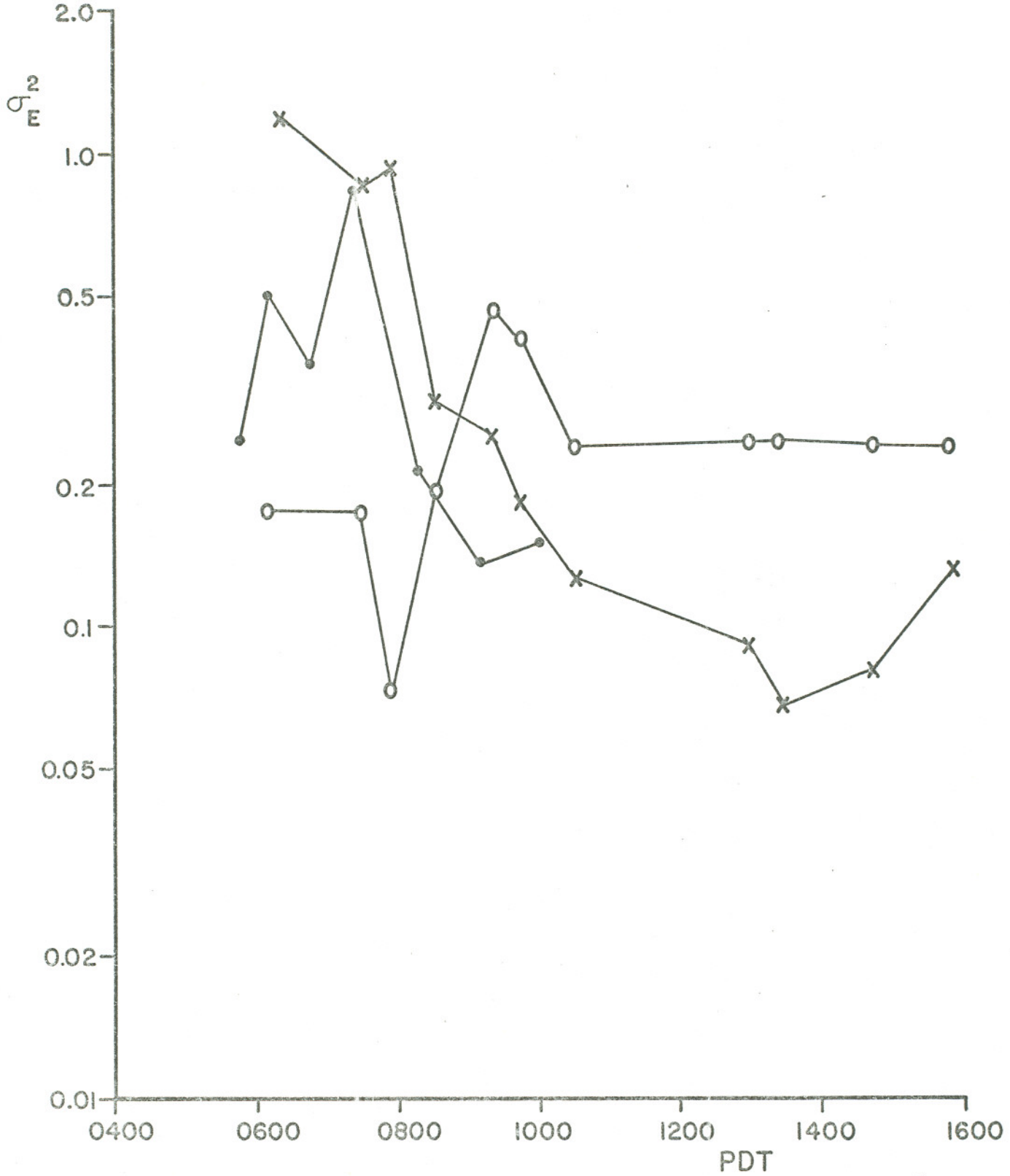

Figure 2. Experimental log-amplitude variance vs time of day. (X): 4880 Å on 14 September 1972; (O): 10.6 μm on 14 September 1972; (●): 4880Å on 29 August 1972. The weather was clear except for a trace of ground fog from 0600 to 0700 on 14 September. During the neutral period, typically 0700-0800, the turbulence was poorly developed.

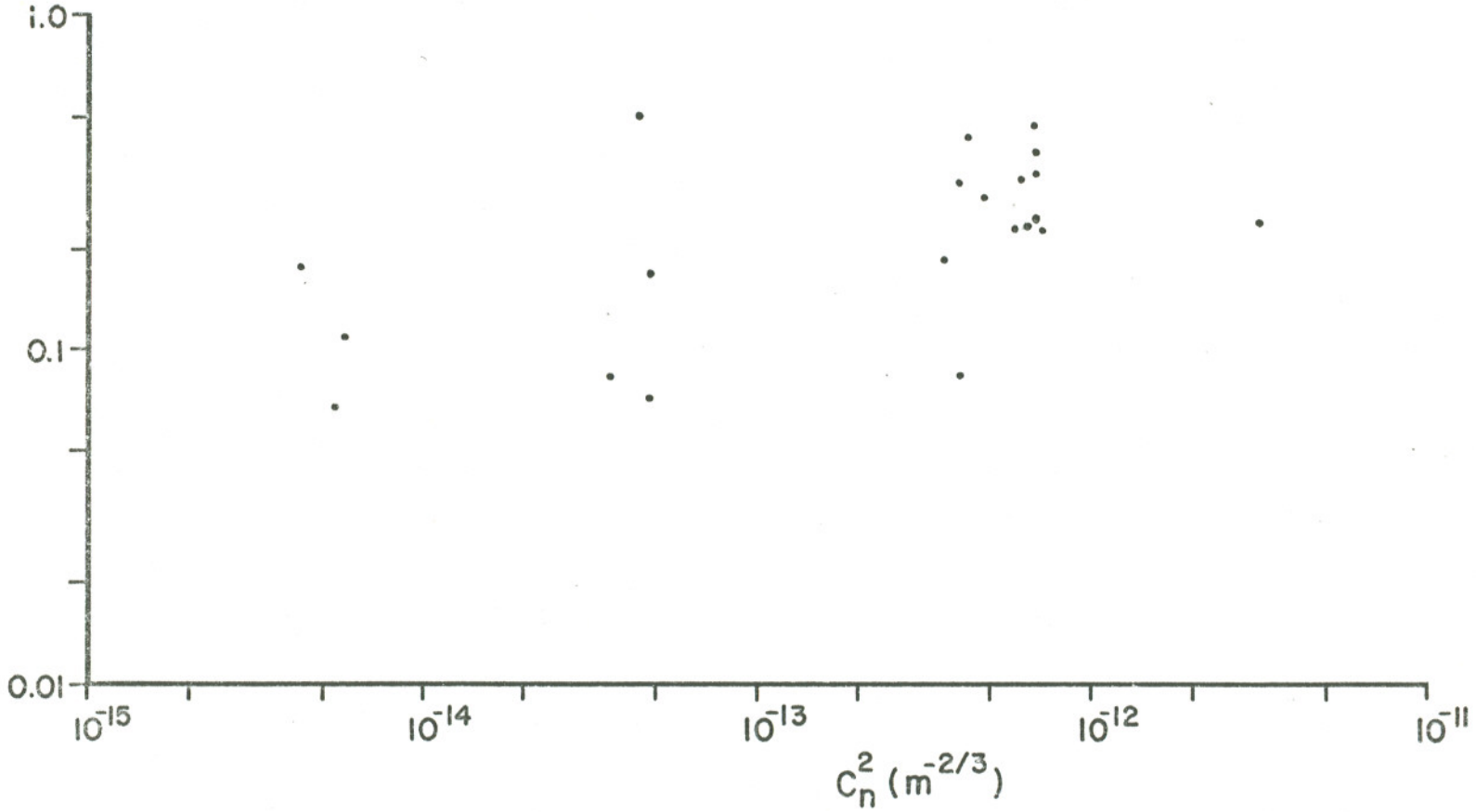

Figure 3. Log-amplitude variance at 10.6 μm vs strength of turbulence at 1.8-m height. The data points include several clear days of operation.

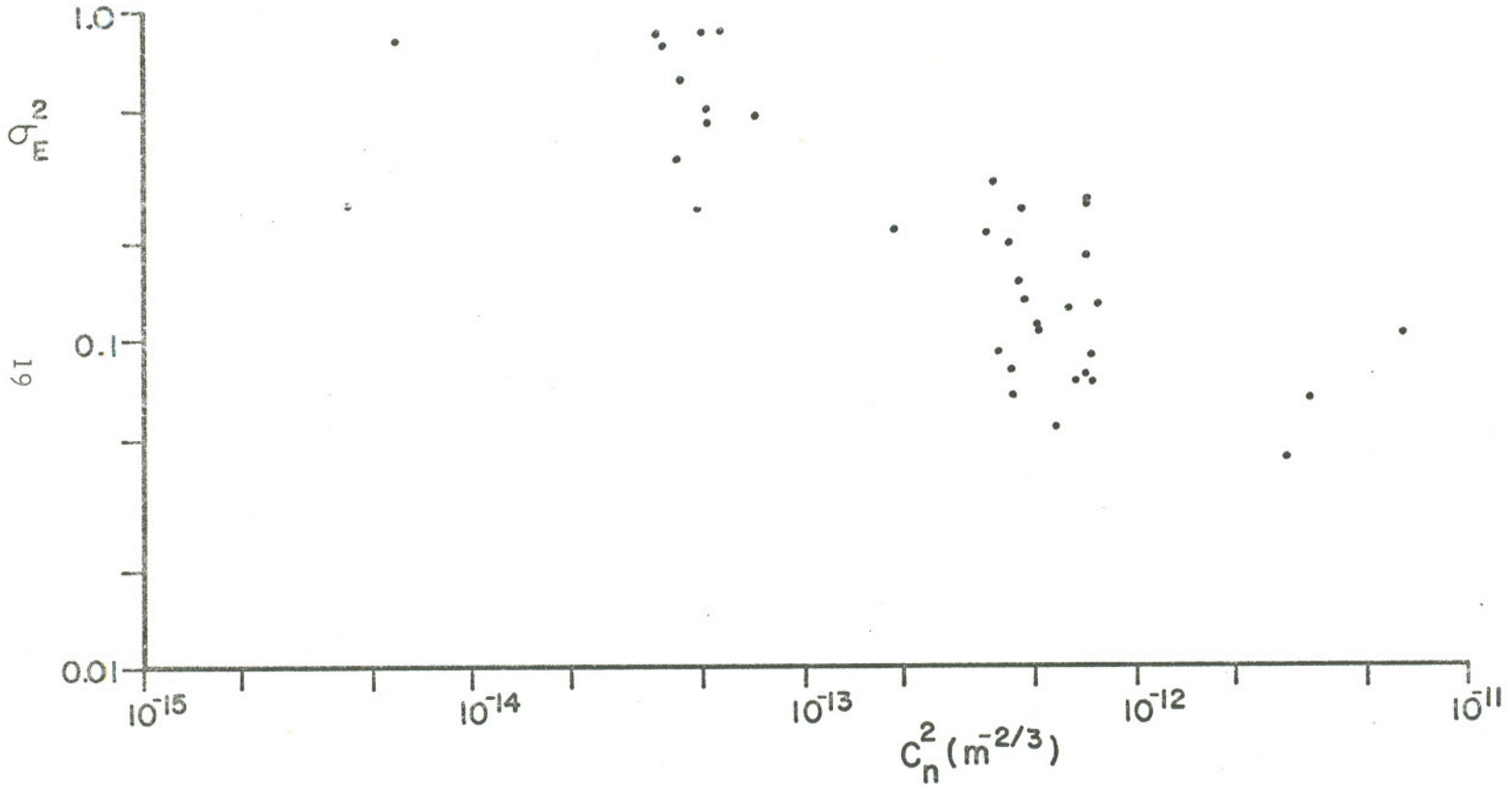

Figure 4. Same as Fig. 3 for 4880 Å.

Since the strength of turbulence depends significantly upon the height above ground, a more-meaningful presentation of the data is obtained by correcting for beam refraction and earth curvature. A useful abscissa is then the theoretical variance σ_T^2, as predicted from the Rytov or first-order theory.[12] If we define the pathlength variable as x, we may write[12,47]

$$\sigma_T^2 = 0.56k^{7/6}\int_0^L C_n^2(x)\left(\frac{x}{L}\right)^{5/6}(L-x)^{5/6}\,dx \quad , \qquad (5)$$

where L is the total path length, and k is the optical/infrared wave number. In accordance with Wyngaard, Izumi, and Collins,[48] the height (z) dependence of C_n^2 is taken as $z^{-4/3}$. We may then account for beam refraction and earth curvature by writing

$$\sigma_T^2 = 0.56k^{7/6}z_o^{4/3}C_n^2(z_o)L^{-5/6}\int_0^L z(x)^{-4/3}x^{5/6}(L-x)^{5/6}\,dx \qquad (6)$$

where z is the beam height and z_o is a reference height.

It still remains to determine z(x), which depends upon the vertical gradient in the refractive index and, hence, on the temperature gradient. Our measurements of the vertical temperature distribution show that the temperature can be reasonably represented as linear over the range involved. The gradient β is small and the resultant refractive index may also be approximated as being linear with height:

$$\frac{dn(z)}{dz} \sim \beta \qquad (7)$$

The trajectory of the beam through such a medium is parabolic.

After a period of trial and error, the receiver and transmitter were fixed at suitable constant heights. Using these heights as boundary conditions and incorporating the earth's curvature, the path may be found for each measured value of β. Representative profiles are given in Table III. The lowest midpath beam heights under negative-gradient conditions, which occurred during the high-turbulence part of the day, were comfortably above ground cover and agreed with visual observations.

Table III. Beam Height (in meters) vs Temperature Gradient and Distance

Thermal Gradient (°K/m)	Distance from transmitter (km)						
	0	1	2	3	4	5	6
+0.4	6.1	7.3	7.8	7.7	6.9	5.5	3.5
-0.06	6.1	5.0	4.2	3.6	3.3	3.3	3.5
-0.2	6.1	4.5	3.3	2.7	2.5	2.3	3.5

With the insertion of the proper trajectories into Eq. 6, the plots of Figs. 5 and 6 are obtained for 10.6 μm and 4880 Å, respectively. A linear-regression analysis for Fig. 6 yields a log-log slope of -0.48 with a correlation coefficient of 0.78. The 90% confidence limits for the slope can be expressed as

$$-0.60 < -0.48 < -0.36.$$

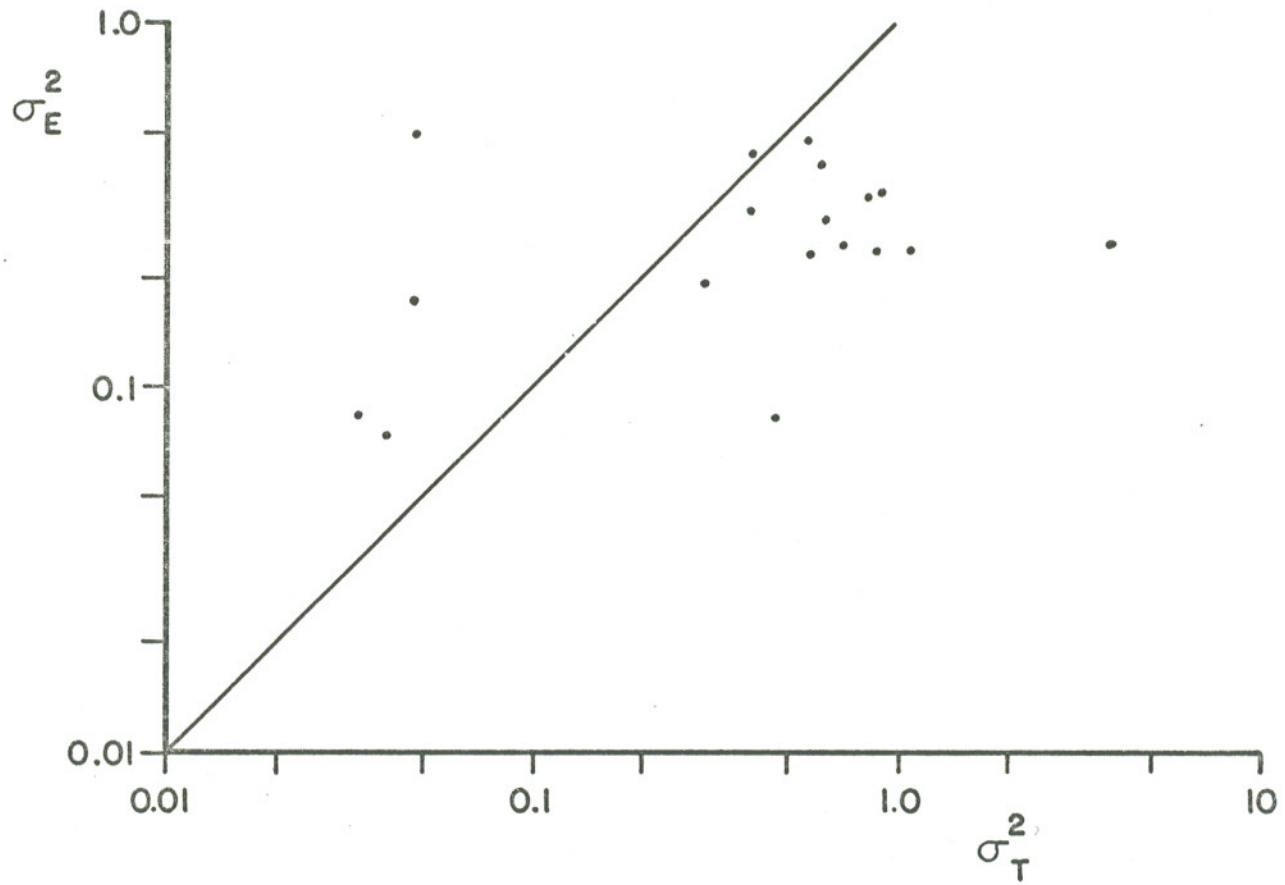

Figure 5. Experimental vs theoretical (Rytov) log-amplitude variance for 10.6 μm. The abscissa is corrected for beam refraction and earth-curvature effects. The line indicates the ($\sigma_E^2 = \sigma_T^2$) condition.

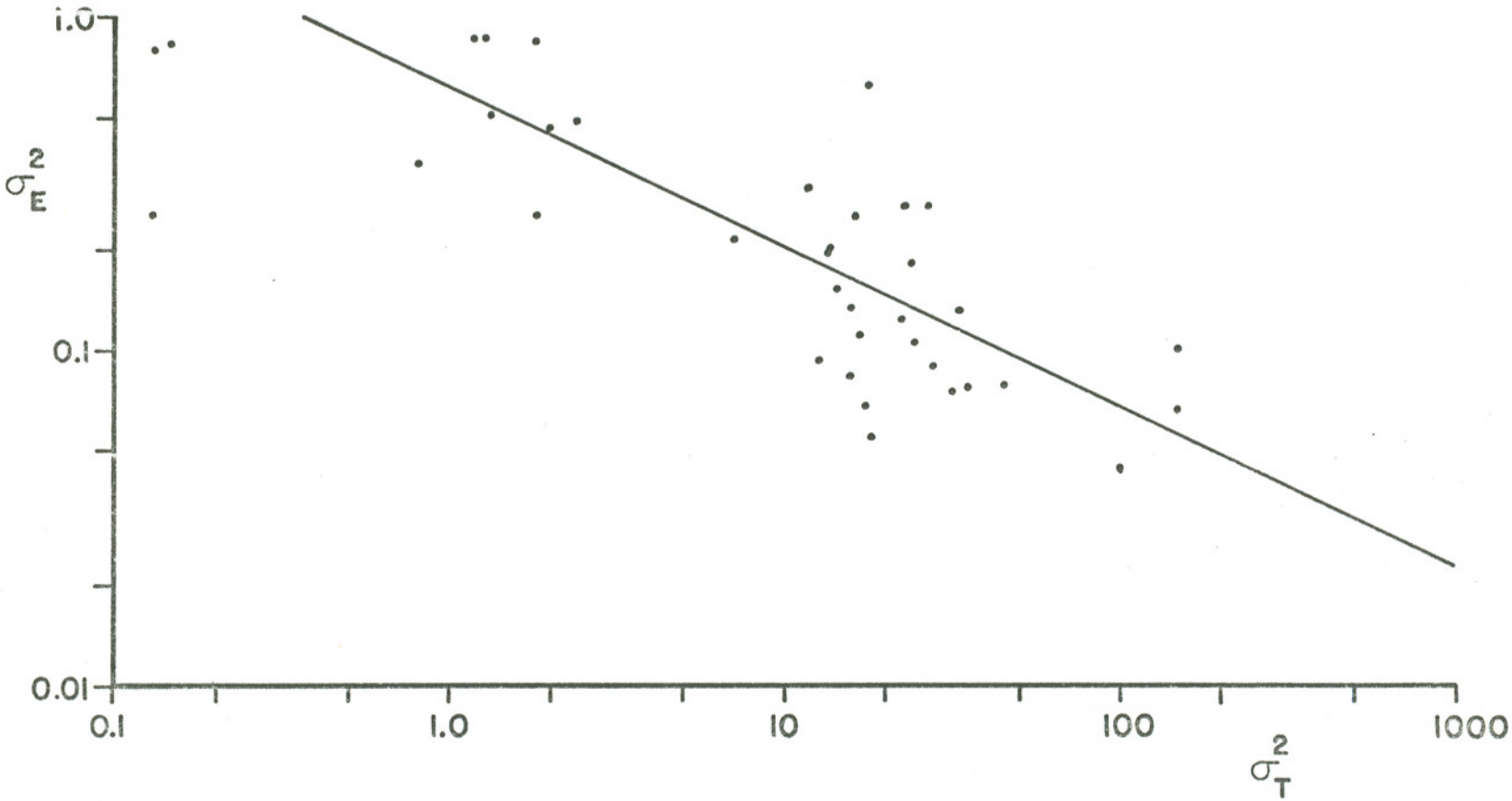

Figure 6. Same as Fig. 5, for 4880 Å. The equation of the linear regression line is $\log_{10}\sigma_E^2 = (-0.22) - (0.48)\log_{10}\sigma_T^2$, with a correlation coefficient of 0.78.

In addition, no asymptote was observed. A plot of the experimental variance at 4880 Å vs that at 10.6 μm is shown in Fig. 7. Similar plots for shorter wavelengths appear in Refs. 16 and 49 and illustrate the failure of the $k^{7/6}$ dependence of Eq. 5 under saturated conditions.

It is of interest to compare the analytical predictions with the results shown in Fig. 6. de Wolf[25] has derived a much smaller slope and the existence of an asymptote. However, his results predict that the onset of saturation is inner-scale (ℓ_o) dependent, with saturation at vanishingly small turbulence levels when ℓ_o approaches zero. Since the experimentally observed saturation curves are apparently universal,[12,16] and the inner scale is very small ($<<$ 1 mm) under the relevant conditions of well-developed turbulence,[16] this prediction does not appear to agree with experiments.

A new and highly physical treatment by Yura[50] predicts a fall-off that is ℓ_o dependent, with no fall-off for ℓ_o approaching zero. This again appears to disagree with measurements. In any event, if ℓ_o is significant in determining saturation behavior, corroborating experiments in a real atmosphere will be very difficult.

Finally, an apparent contribution to the log-amplitude variance at 4880 Å is due to very small scintillation-correlation scales (high scintillation frequencies), and both electronic and 6-mm receiver-aperture filtering have reduced this component in the present data. A correction for this

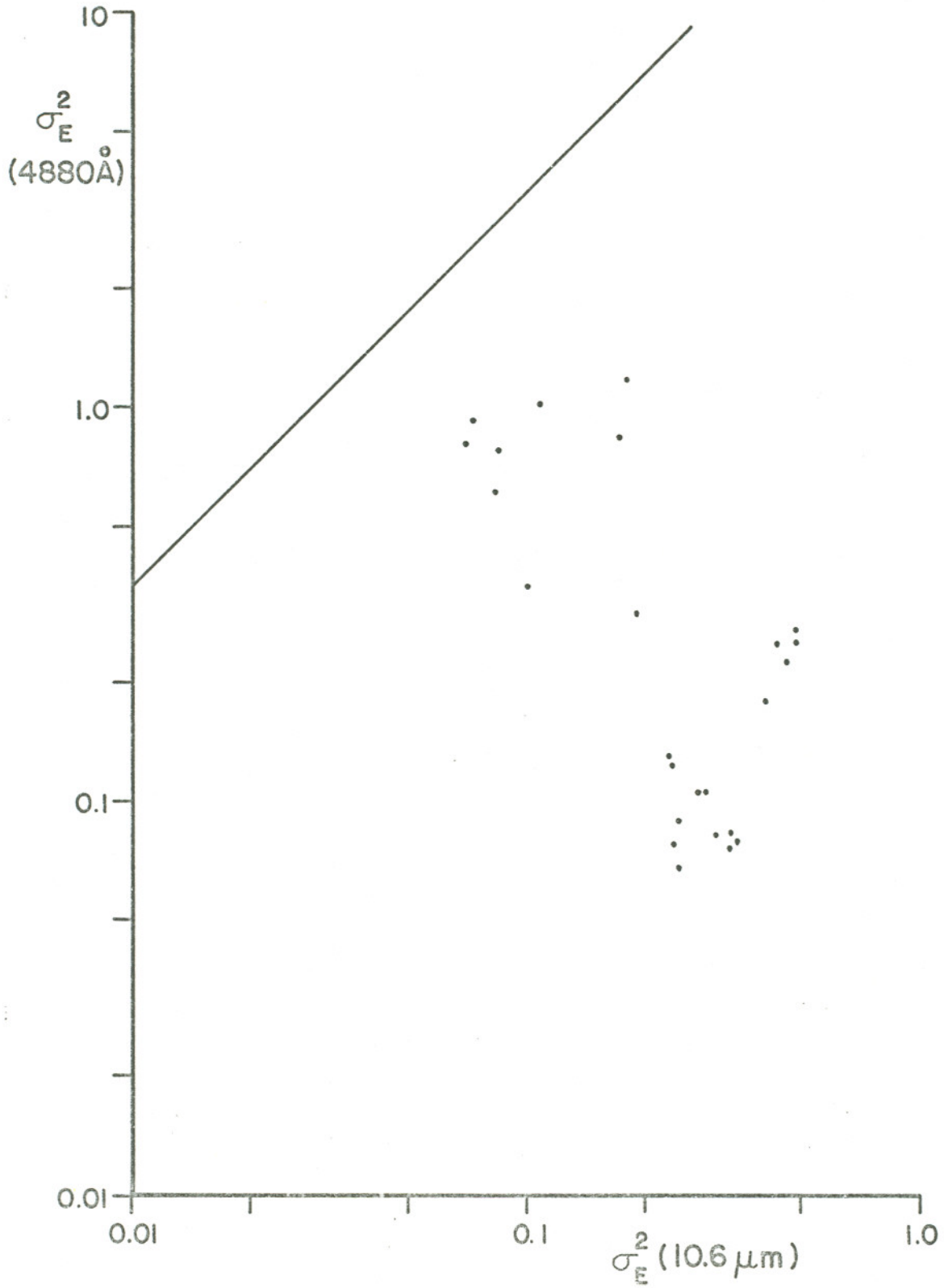

Figure 7. Experimental variances at 4880 Å vs those at 10.6 μm. The line represents a $k^{7/6}$ dependence.

effect will decrease the magnitude of the slope in Fig. 6 to some extent. There is also a possibility that humidity variations could affect the data, especially at 10.6 μm.[51] For instance, the prematurely high scintillation levels of Fig. 5 might be an effect due to very slight traces of early morning ground fog. However, the hot dry midday conditions were the target of main interest, and since our path was removed from any bodies of water, the effect of humidity fluctuations on these data are not expected to be significant.

I.B.2. Log-Amplitude Covariance

The transverse log-amplitude correlation length r_a, which is defined from the 1/e point of the measured covariance curve, is shown as a function of C_n^2 in Fig. 8. A significant effect is observed at stronger turbulence levels, where r_a is seen to decrease at 10.6 μm and to increase at 4880 Å. This agrees with a trend observed in earlier work.[16]

In order to understand better the significance of these results, it is necessary to consider the detailed shape of the covariance curves. Typical curves for 10.6 μm are shown in Fig. 9. At low C_n^2, the function approximates the theoretical prediction, except for large separations, where outer-scale effects may enter. However, as C_n^2 increases, two new and highly disparate scale lengths emerge such that for strong turbulence the scintillation patches are quite small, with a significant residual correlation

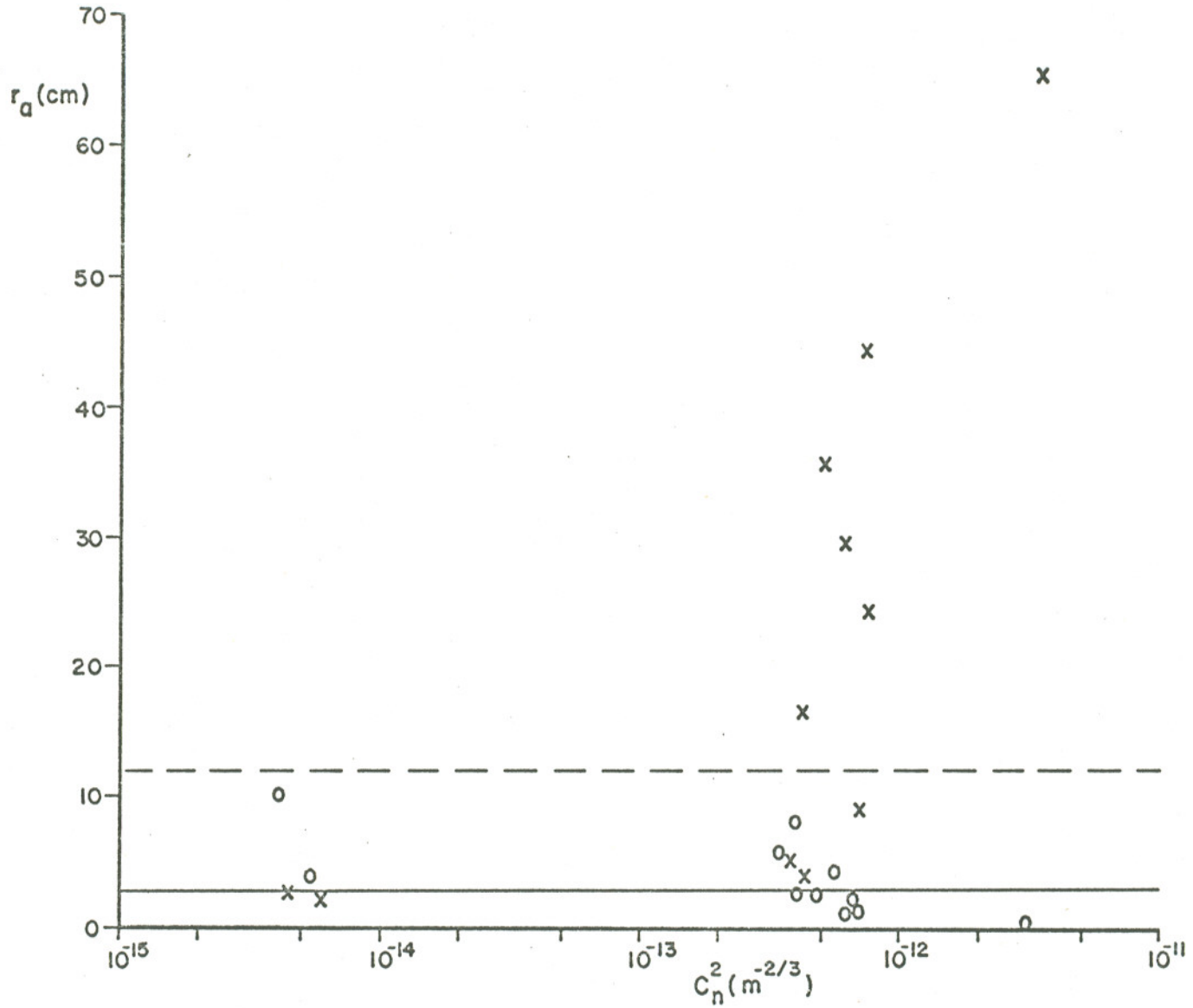

Figure 8. Transverse log-amplitude covariance length vs strength of turbulence. The experimental and theoretical (Rytov) values are for 4880 Å (X, ——) and 10.6 μm (O, ----).

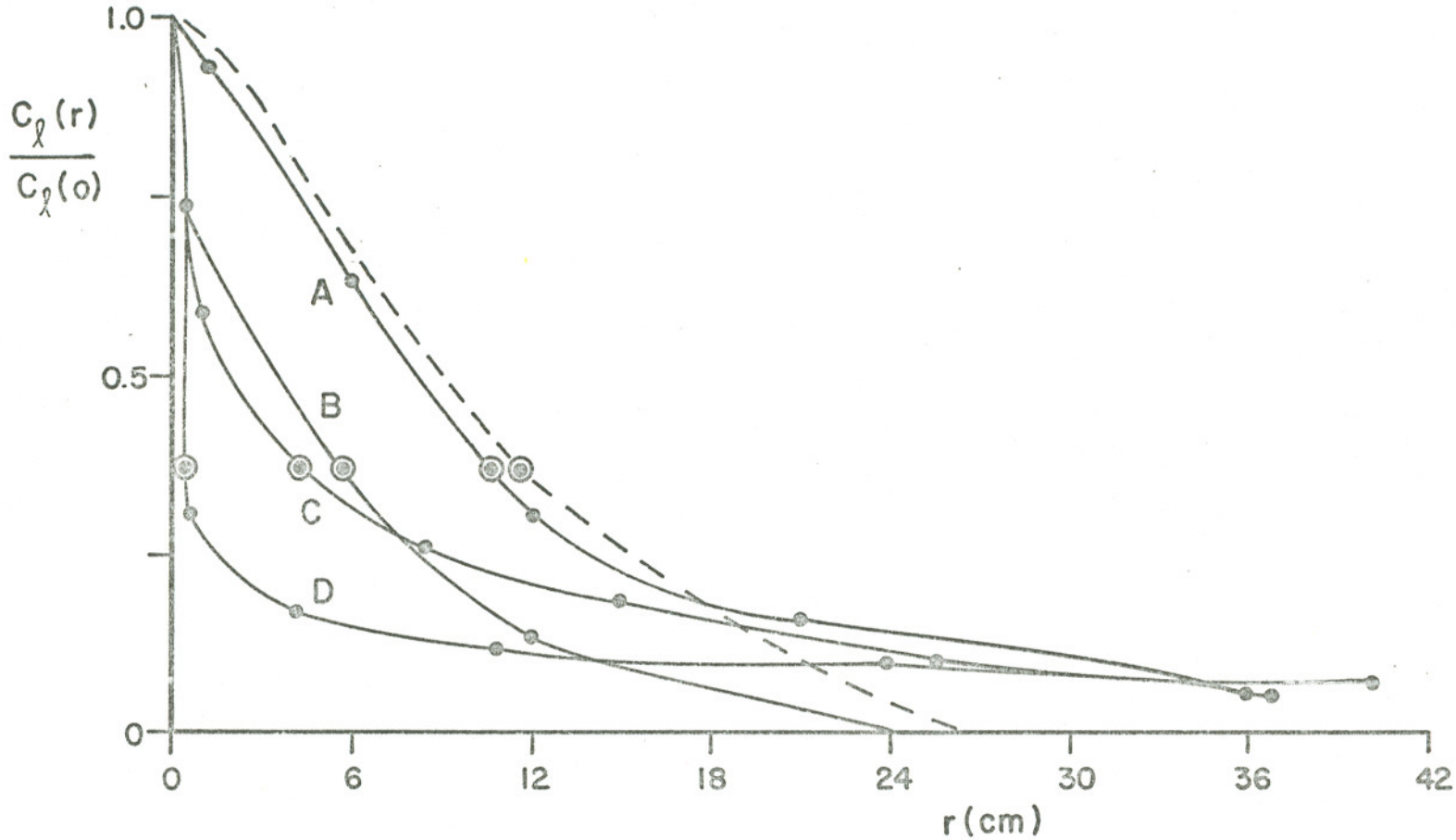

Figure 9. Normalized covariance curves for 10.6 μm. The normalizing quantity $C_1(0)$ is identical to σ_E^2, and the 1/e points are indicated. The broken line represents the theoretical (Rytov) function.

Curve	C_n^2	σ_T^2
A	4.2×10^{-15}	2.6×10^{-3}
B	3.6×10^{-13}	3.0×10^{-1}
C	5.9×10^{-13}	5.9×10^{-1}
D	3.2×10^{-12}	3.9

over large separations. This unusual manifestation of multiple scattering is predicted in a recent two-dimensional analysis by Brown[29] and in a new analysis by Yura.[50]

This effect is even more pronounced at 4880 Å, as shown in Fig. 10. The effect is so extreme as to suggest that significant spatial and electronic filtering of the small scintillation patches is occurring at high-turbulence levels; this is confirmed in Sec. 3 and indicates that, e.g. for curve D, a very sharp initial fall-off has been obscured and that the normalization is incorrect. This explains the behavior seen in Fig. 8. Visually, at high turbulence levels the very large correlation patches are observed, and the very small patches are washed out by eye response. These results imply very poor receiver-aperture smoothing.

I.B.3. Scintillation Spectra

The scintillation power spectra of the linear irradiance at 10.6 μm are shown in Fig. 11 for the same turbulence levels as in Fig. 9 and corroborate the behavior shown in Fig. 9. As the turbulence increases, much more energy appears at high frequencies; a concurrent shift to low frequencies is obscured by the low-frequency cutoff of the spectrum analyzer.

The results at 4880 Å (Fig. 12) apparently fail to encompass sufficient low- and high-frequency ranges to manifest the extreme scales shown in Fig. 10. An exception is the transitional curve B. A similar plot,

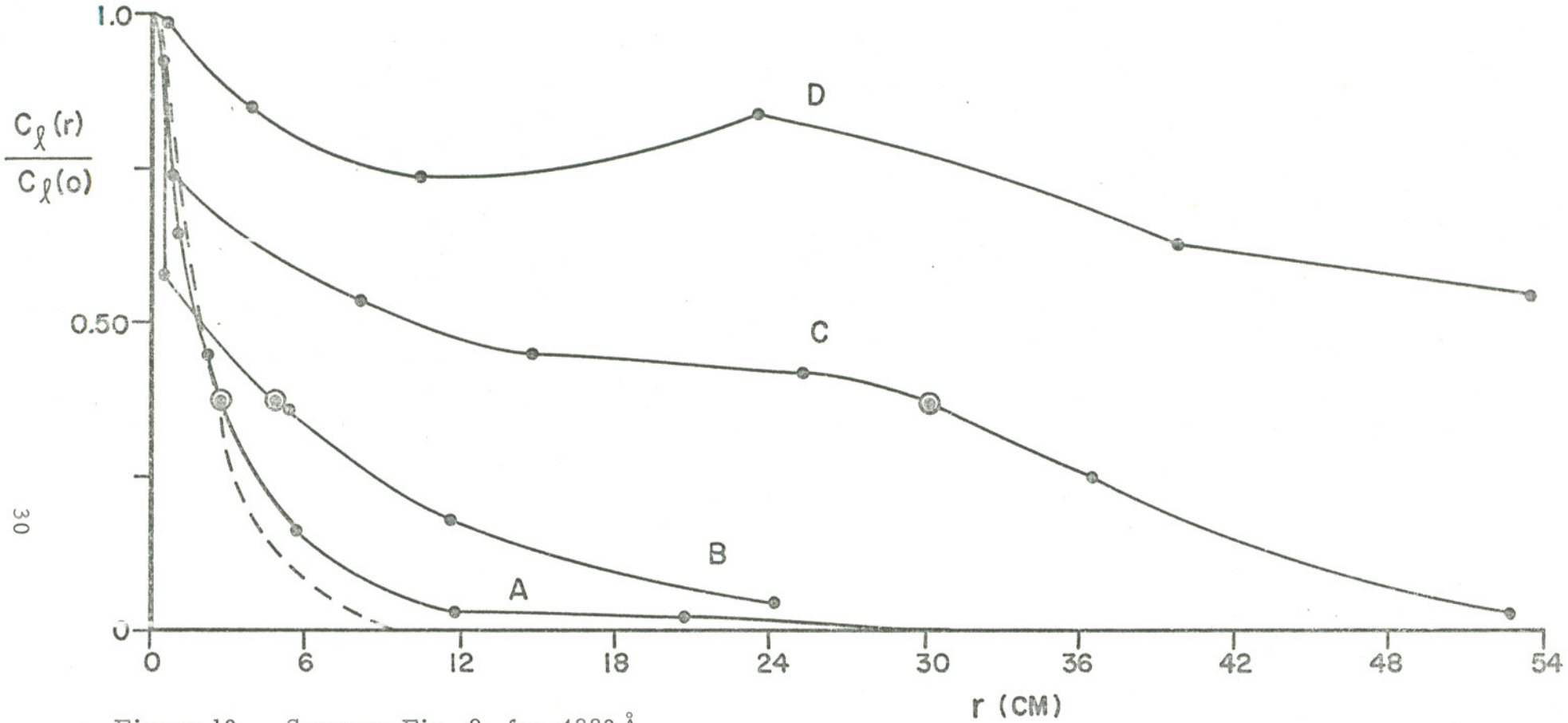

Figure 10. Same as Fig. 9, for 4880 Å.

Curve	C_n^2	σ_T^2
A	4.5×10^{-15}	1.0×10^{-1}
B	3.8×10^{-13}	1.2×10^{1}
C	6.3×10^{-13}	2.3×10^{1}
D	3.4×10^{-12}	1.5×10^{2}

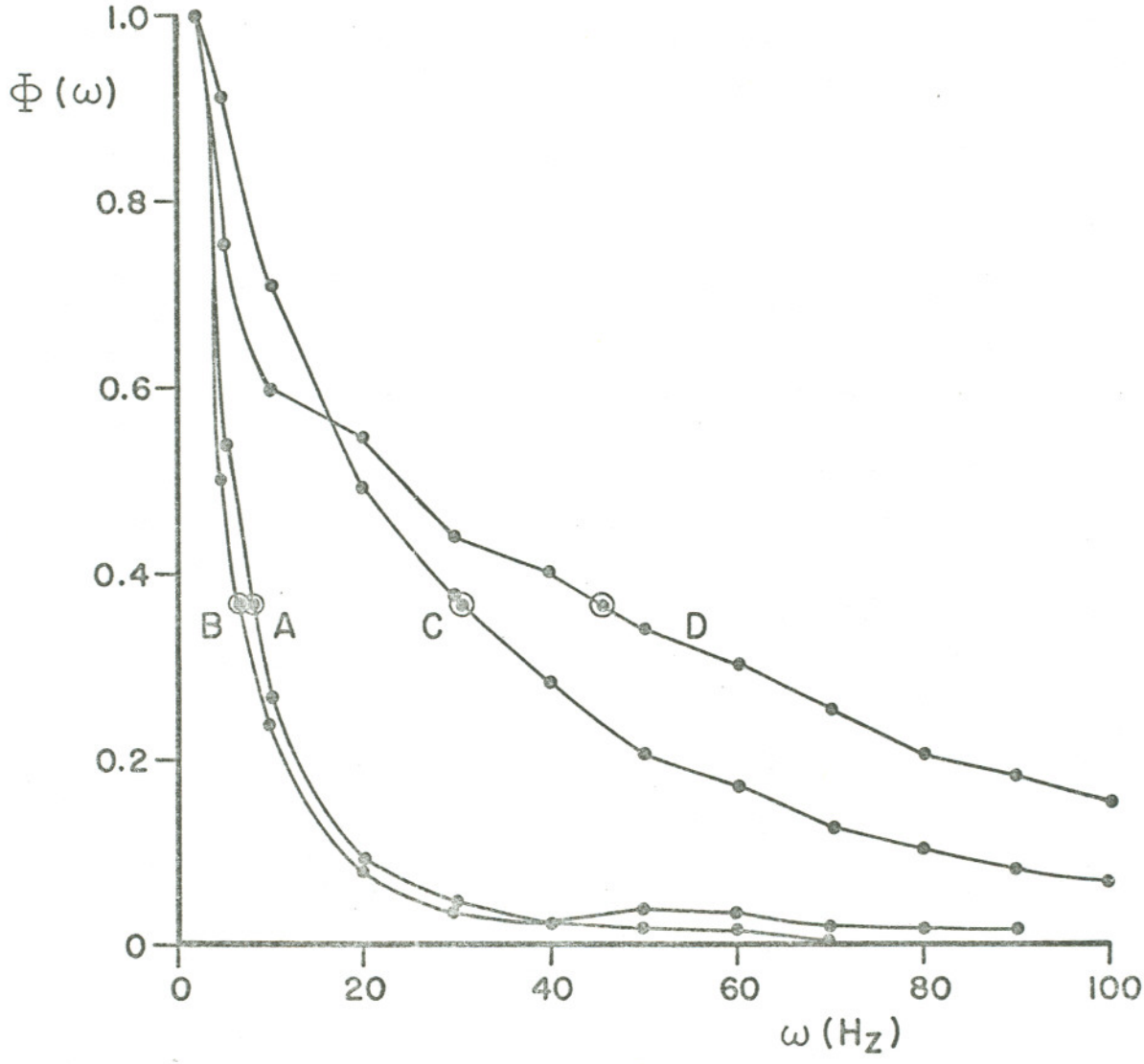

Figure 11. RMS scintillation spectra at 10.6 μm for the C_n^2 values of Fig. 9. The 1/e frequencies are indicated.

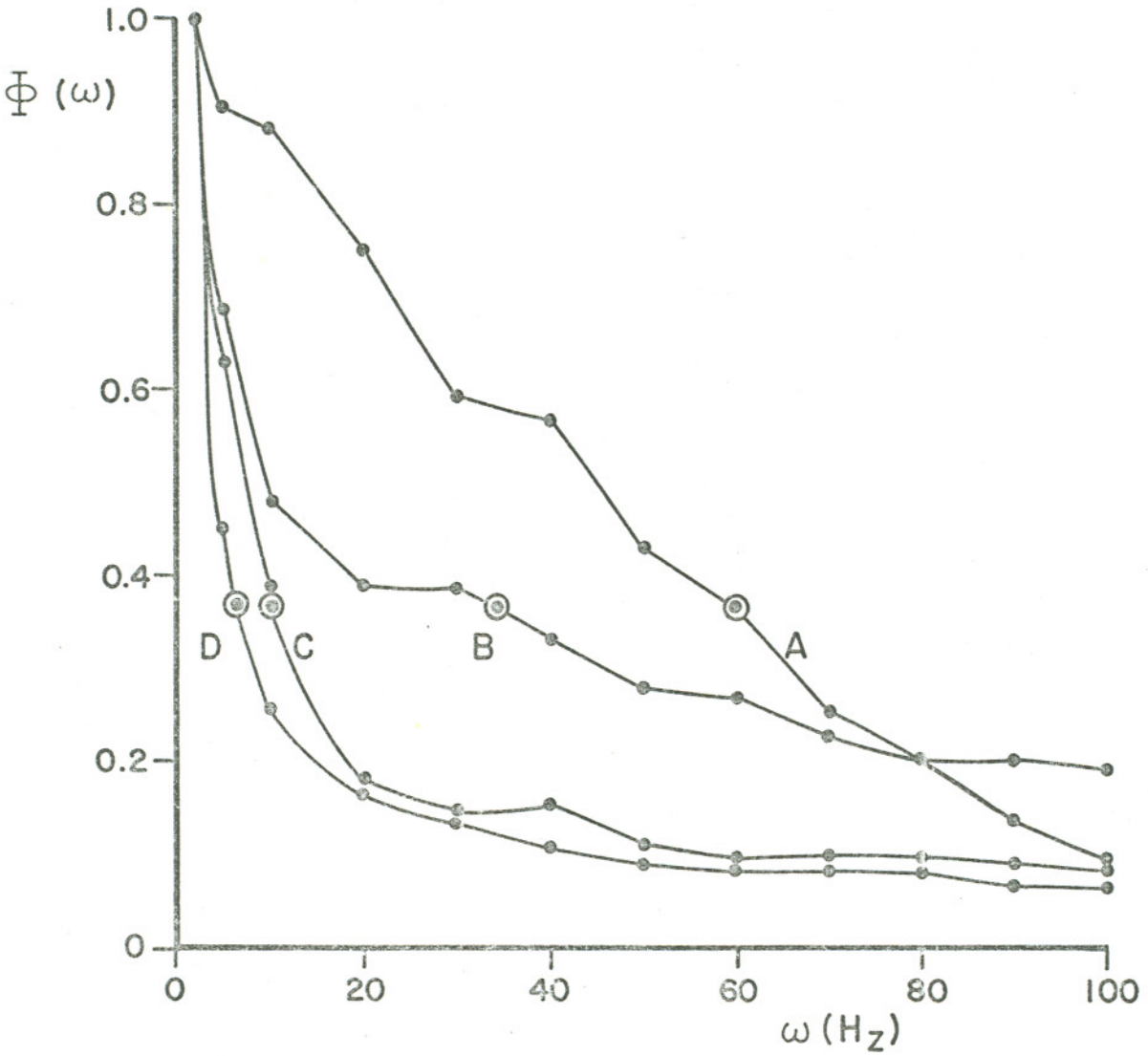

Figure 12. RMS scintillation spectra at 4880 Å for the C_n^2 values of Fig.10.

extending to 1 kHz, is not substantially different, and quantitative spectral results above that frequency were not obtained, because of electronic and spatial (6-mm-receiver) filtering.

The fact that, at these very large integrated-path turbulence levels, substantial scintillations occur at frequencies above 1 kHz was verified by direct observation of the signal (Fig. 13). This interesting behavior confirms that the initial part of curve D in Fig. 10 has been obscured by instrumental effects. A similar display at 10.6 μm is given in Fig. 14. The emerging low-frequency components were also readily visible on appropriate time scales.

The spectral results in Figs. 11 and 12 are of only semiquantitative significance because the wind velocity was variable during the time periods spanned. An attempt to normalize out this effect, as in Ref. 16, was unsuccessful, owing to the complicated nature of the covariance and spectral curves and the corresponding inadequacy of single-parameter descriptions (e.g. r_a).

I.B.4. Probability Distributions

Theoretical treatments predict Rayleigh-amplitude statistics at large turbulence strengths.[23] Our experimental results (Fig. 15) confirm that the scintillations remain substantially log-normal, with no indication of Rayleigh behavior. This agrees with more-recent treatments.[25] In the

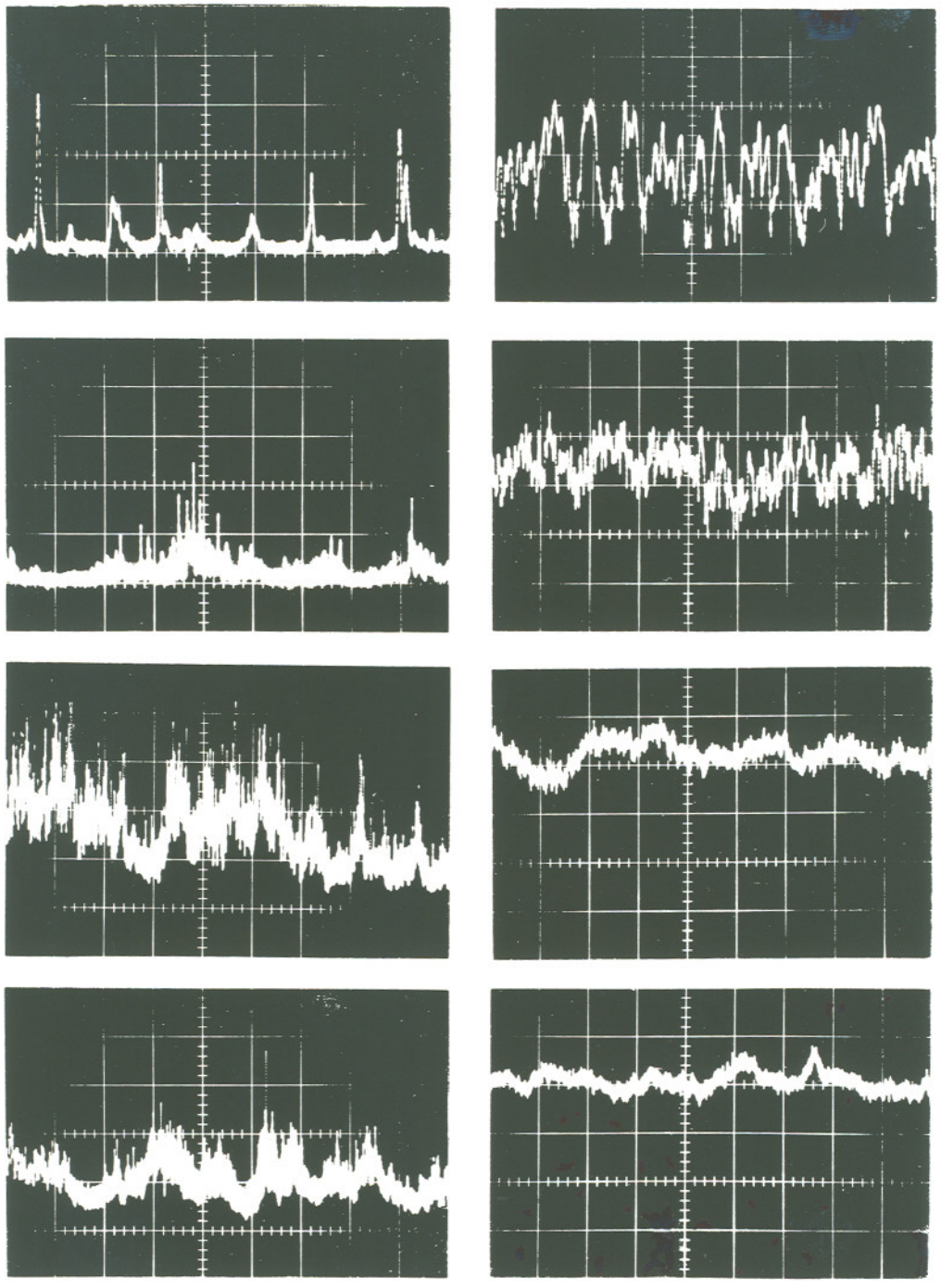

Figure 13. Linear (left) and log (right) irradiance scintillations at 4880Å. The pictures from top to bottom represent C_n^2 values A-D, respectively, of Fig.10. The abscissa is 0.2s/cm; the ordinate for the log signal is one decade of irradiance per cm. The linear baseline is 1 cm up from the bottom of each frame; the log baseline is indefinite and not pertinent.

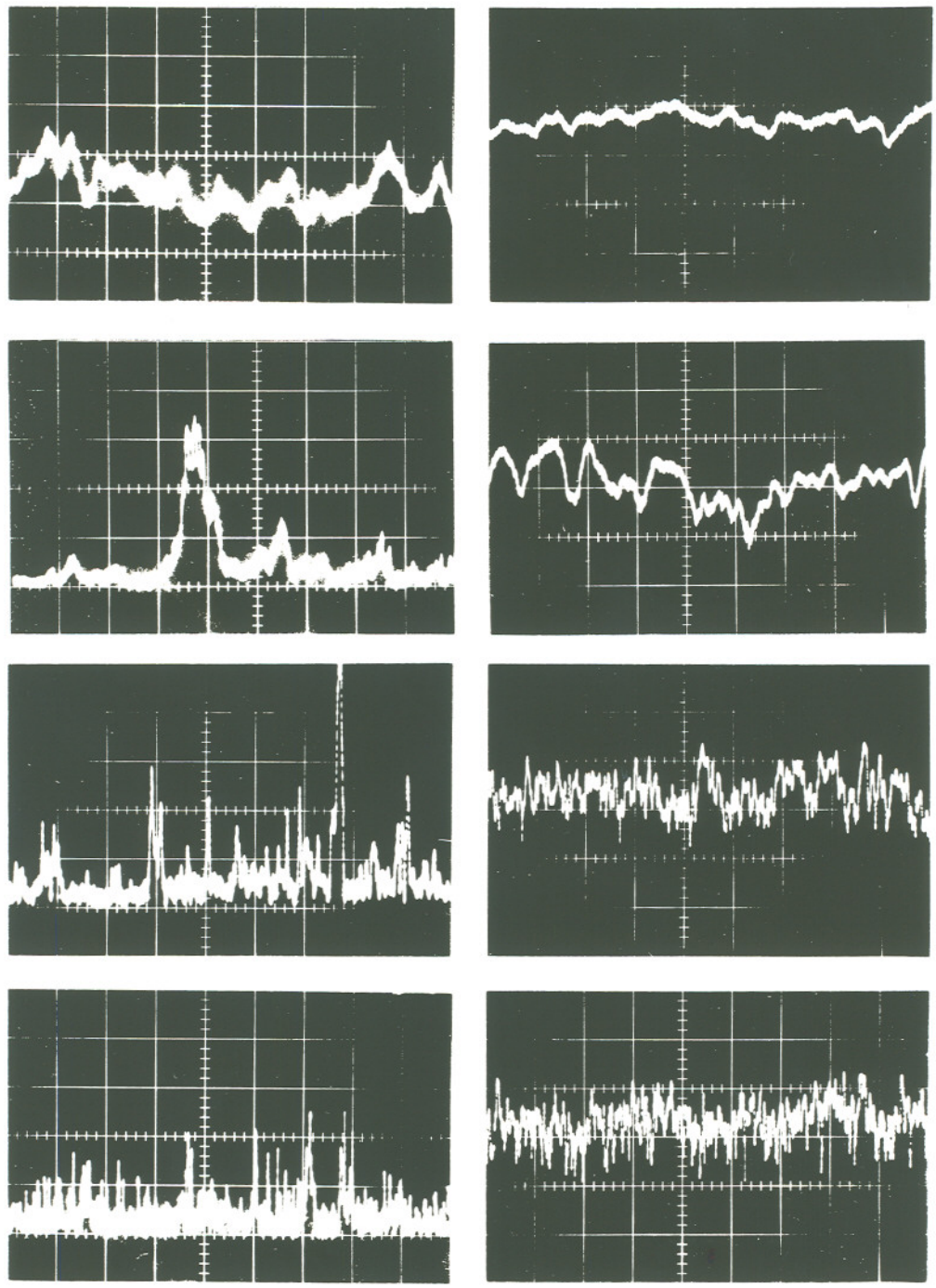

Figure 14. Same as Fig. 13, for 10.6 μm. The turbulence levels are those of Fig. 9.

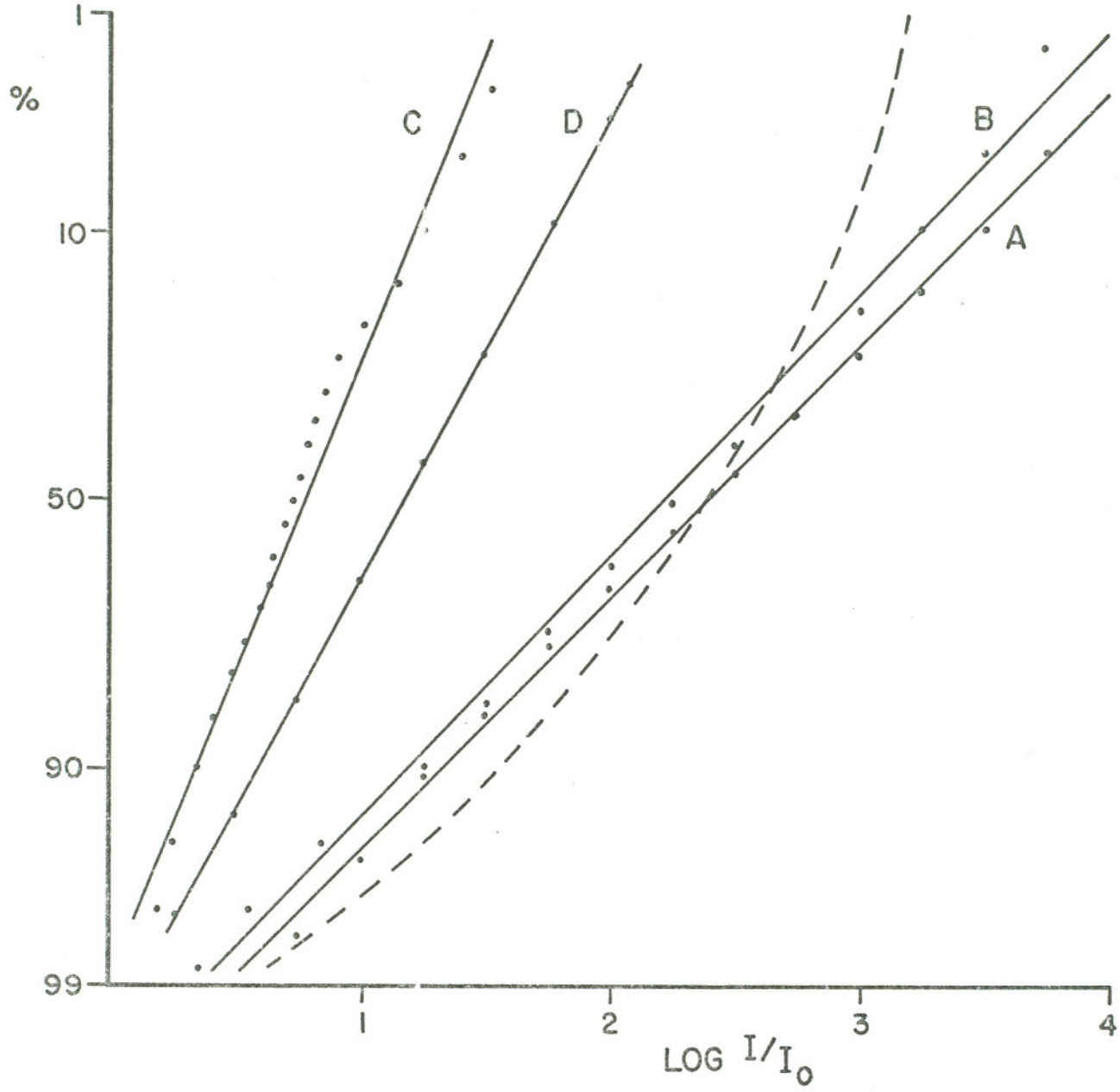

Figure 15. Cumulative probability distributions for log irradiance.

Curve	Wavelength	C_n^2	σ_T^2
A	4880 Å	4.5×10^{-15}	1.0×10^{-1}
B	4880 Å	3.4×10^{-12}	1.5×10^{2}
C	10.6 μm	4.2×10^{-15}	2.6×10^{-3}
D	10.6 μm	3.2×10^{-12}	3.9

For curve B, the abscissa should ge divided by 3.3. The broken curve represents a Rayleigh-amplitude distribution.

Rayleigh case, the dynamic range between two probability levels is invariant; the present data are sufficient to rule out a Rayleigh distribution.

I.B.5. Receiver Aperture Averaging

The covariance results of Figs. 8 and 9 suggest that receiver-aperture smoothing will be very poor for high integrated-path turbulence levels. This was directly confirmed at 4800 Å with large-receiver measurements as shown in Table IV.

Table IV. Typical Receiver-Aperture Smoothing Results at 4880 Å. The receiver-smoothing factor Ω is the log-amplitude variance for a 32-cm receiver, normalized by that for a small (6-mm) receiver.

C_n^2	Ω
3.1×10^{-12}	0.46
7.5×10^{-13}	0.35
5.4×10^{-13}	0.70

I.C. RECENT THEORETICAL AND EXPERIMENTAL EFFORTS

Following the theoretical and experimental work described above, there has recently been new and significant effort to complete the description of the saturation phenomenon. This section provides an updated review of these theoretical and experimental attempts.

I.C.1. Experiments

Recent high turbulence propagation work done in the USSR is important because small detectors 0.3 mm in diameter were used (some of the data was taken with 5 mm diameter receivers but how much is not clear). The implication is that an unbiased supersaturation slope should be obtainable. However, before making further comment, it is useful to clarify their notation. For instance, their parameter β_o is equivalent to the square root of the theoretical Rytov prediction for the log-irradiance variance of a plane wave, $\sigma^2_{\ln I}$. The parameter that they plot as experimental data is β which is the square root of the normalized variance of the linear irradiance, σ^2_I. With these parameters in mind, we find that their measurements begin to saturate at the same theoretical Rytov value of the log-amplitude variance ($\sigma^2_\chi = 0.56$) seen by others.[16] Their data exhibited a peak value of $\beta^2 = 1.69$ with only a slight supersaturation to to about 1.5. These measurements agree with the maxima predicted by the theoretical extensions of propagation theory reviewed in I.A. However, in terms of the log-amplitude variance, their saturation peak was only $\sigma^2_\chi = 0.25$ ($\beta^2 = 1.69$) which is about half of the value normally seen. In addition, when their supersaturation slope is translated into log-amplitude terminology by using the log-normal approximation for the distribution, it becomes almost negligible. Ref. 52 also measured the covariance function and found behavior similar to our measurements. Interestingly,

their spectra definitely showed the effects of two scale sizes. Their work also confirmed the fluctuations to be log-normally distributed. Lastly, they found that a beam wave did not behave differently from spherical or plane waves during saturated conditions.

Further high turbulence experiments have also been completed in the United States by Clifford, et al.[53] Their measurements corroborate those reported here and those of Gracheva, et al. The only point of discrepancy is that they observed saturation beginning at a measured σ_χ^2 of about 0.3, (in agreement with Ref. 52 and in agreement with the CO_2 data presented here) compared to our higher value for argon data. Our higher value for the visible wavelength can be explained to result from poorly developed turbulence. Due to the extreme length of our propagation path, only atmospheric conditions providing low C_n^2 values could give measurements prior to the onset of supersaturation. Unfortunately, these conditions existed only during the early morning hours when turbulence could not be expected to be well developed, thus causing possible discrepancies between experimental values presented here and those of Clifford, et al.

I.C.2. Theory

Ref. 53 also has significant theoretical comment to attend their experimental efforts. Clifford, et al. present a numerically solvable theory that applies Huygens-Fresnel techniques to determine a modification to the transmitter-path filter function utilized in the method of smooth

perturbations. It predicts the experimental saturation curve in detail. Of special interest is the fact that their predicted dependence in the super-saturation region is $(\sigma_\chi^2)^{-2/5}$ which agrees well with our measured dependence of $(\sigma_\chi^2)^{-.48}$. In addition, their theory supports our covariance and probability distribution measurements.

Yura[54,55] has also developed a modification of Tatarskii's method of smooth perturbations which allows the unmodified theory to include diffraction and loss of coherence in the optical field. The modified theory can describe the saturation of spherical and plane waves. The transverse coherence scale size, ρ_o, is fundamentally involved. A smooth saturation without a peak is predicted to a constant of order unity. In saturation the covariance function narrows until it becomes equal to ρ_o in width. This fact is very pleasing physically, for in strong turbulence it means that the correlation scale size for both the amplitude and the phase becomes ρ_o. For experimental investigations as presented in (I.B.) the implication of the covariance collapse is that significant spatial and temporal filtering will take place for finite receiver sizes and limited electronic bandwidths.[56]

A recent paper[57] presents proof of the equivalence of the above works of Yura and Clifford, et al. The addition of this new work to the file of theoretical extensions allows one to equate the modified versions of the method of smooth perturbations with those of renormalization and moment techniques. In addition it stresses that saturation is independent of wavelength,

propagation distance and turbulence parameters (as in Ref. 54). Subject to the assumptions of a particular value for their α parameter and a log-normal distribution, they found that σ_χ^2 saturates to a value of about 0.5 and then assymptotically approaches a value of 0.23 (for the theoretical Rytov value approaching infinity). Hence their theory supports a peak saturation value with a definite supersaturation effect. The detail of this hump at saturation agrees in general with all the theory reviewed in Section I.B., but the assymptote appears to be the peak value of the other theories.

Much interest surrounds the question of a saturation peak and super-saturation in contrast to smooth saturation. Reviewing Brown's work,[29] it can be suggested that for a larger α value that the saturation curve of Ref. 57 would not exhibit a hump. At this point the most reasonable discussion of the effect is due to Yura.[58] He specifically shows that for definite truncation of spatial or temporal frequencies, saturation measurements and/or theories produce a supersaturation effect. The decay of σ_χ^2 in saturation with temporal or spatial bandwidth limitations will depend on $(\sigma_\chi^2)^{-2/5}$, the result of Clifford, et al.

Further comment on the modifications to the method of smooth perturbation is given by deWolf.[59,60] In fact, he considers his approach to be more fundamental, even though his results don't agree as well with experimental evidence as do the results of Refs. 53 and 54.

Since the work of I.B., additional extensions of the renormalization technique have been contributed by deWolf.[61,62] The results are not greatly different from Ref. 25. However, in Ref. 61 deWolf produces additional information suggesting that his renormalization work gives high turbulence covariance narrowing as do the modifications to the method of smooth perturbation. Alternatively, Yura[55] refutes that deWolf's theory agrees with experimental observations.

Finally, the most recent additions in the moment equation group show that in saturation the intensity can neither be exactly log-normal[63] nor Rayleigh[64] in distribution and that for large propagation distances the correlation scale size of a finite transmitter becomes independent of the transmitter's size.[65]

I.D. CONCLUSION

In the experiments described here, the log-amplitude variance at 10.6 μm was observed to saturate for the first time. This occurred at a value of approximately 0.3 over the 6 km path. At 4880 Å the variance saturated at a slightly higher value and then exhibited strong supersaturation with apparently no assymptote. However, these results were biased by a new effect discovered during the experiments. The covariance scale size was found to depend strongly on turbulence levels. It was experimentally established that the initial correlation was reduced drastically

with the onset of saturation. Concurrently, a residual correlation appeared at large distances. This modification of the covariance function was sufficient to cause spatial and electronic filtering effects that could significantly bias the log-amplitude variance measurements. Furthermore, it is proposed that very poor receiver aperture averaging at 4880 Å was caused by the modified covariance function. Even though the strong turbulence levels induced these extreme effects on the overall distribution, the intensity (and amplitude) statistics remained approximately log-normal at both wavelengths.

Since these experiments, the observed effects have been successfully explained by theoreticians. The combined progress of this experiment and recent theoretical work has led to a nearly complete understanding of optical propagation subject to conditions of strong atmospheric turbulence. This understanding is fundamentally important to practical design problems utilizing lasers in the atmosphere.

CHAPTER II. PROPAGATION OF A PASSIVE, FOCUSED BEAM WAVE

INTRODUCTION

The previous chapter was aimed at testing the propagation theories for classical wavefronts. In this chapter advantage is taken of a unique capability afforded by the application of lasers in optical systems operating in the atmosphere: the wavefront is finite and can be shaped. The resulting effects are discussed by Lawrence and Strohbehn.[12] Of particular interest is the prediction that a finite, focused beam wave reduces atmospherically induced fluctuations on the optical carrier. Ishimaru[66,67] has developed propagation theory for the beam wave to a point that is manageable for fundamental testing. This chapter is specifically directed towards experimental examination of his results.

II.A. THEORETICAL PREDICTIONS

Ishimaru[66] provides the general expression for the log-amplitude variance in the target plane of a finite beam wave

$$\sigma_\chi^2 = 0.033\pi^2 k^{7/6} L^{11/6} \left[-\Gamma\left(-\frac{5}{6}\right)\right] \int_0^1 dx\, C_n^2(x)\, G_a(x) \qquad (8)$$

where k is 2π divided by the optical wavelength, and L is the pathlength through the turbulent medium. C_n^2 is the strength of turbulence, and G_a

is a spatial filter function that depends on the size of the transmitter and its wavefront shaping. In the same reference, an example (his Fig. 11) is given indicating that when the beam is focused on the target plane that the log-amplitude variance is reduced by an order of magnitude (compared to that of a plane wave) for even a modest size of beam.

The specialization of Eq. 8 to the case of a negligible inner scale is used by Kerr and Eiss[68] to detail the dependence of σ_χ^2 for the beam wave as the shape of the wavefront is adjusted. The size and shape of a beam wave are described by $\alpha_1 L$ and $\alpha_2 L$. $\alpha_1 L$ is defined as the inverse Fresnel number, $\lambda L/\pi\omega_o^2$, where λ is the wavelength of the radiation, L is the propagation distance, and ω_o is the e^{-1} amplitude radius of the beam. $\alpha_2 L = L/R$ describes the curvature (R) of the wavefront relative to the distance (L) of propagation. $\alpha_2 L$ has a value of 1.0 and 0 for focus and collimation, respectively. When the calculated beam wave variances are normalized by the log-amplitude of a point source, important facts are revealed. These can be summarized as follows:

1. If $\alpha_1 L > 100$, then the transmitter effect is equivalent to that of a point source.

2. If $\alpha_1 L \ll 100$ and the transmitter is collimated, then the irradiance distribution scintillates more than that of a point source.

3. If $\alpha_1 L \ll 1.0$ and the transmitter is grossly defocused, then the scintillation is equivalent to that of a point source.

4. If $a_1 L \ll 1.0$ and the transmitter is only slightly defocused, then the scintillation is enhanced to a level that can be an order of magnitude greater than that of a point source.

5. If $a_1 L \ll 1.0$ and the transmitter is precisely focused, then the scintillation will go to nearly zero.

The beam configuration of (5.) is of prime interest, and point (4.) suggests that the adjustment of the transmitter to meet the conditions of (5.) are extremely important in order that reduced scintillation, rather than enhanced scintillation, is observed. The fact that theoretical works by others produce similar effects[69-72] as mentioned here (but with less detail) lends weight to these arguments.

It is further desirable to understand physically why the finite sources, when precisely focused, should yield lower scintillation levels compared to point sources. Fried[73] suggests a spatial diversity effect. On the other hand Massey[74] furnishes a discussion based on ray optics and interference. It is observed for large transmitters that the geometrical conditions for π relative phase shifts are minimized. Consequently, scintillation is reduced.

With this introduction to the effect that is called finite transmitter averaging, the experimental efforts are reviewed. We note there that this experimental work was completed some time ago and reported by 21 August 1972.[75] Hence the point of view taken in this chapter is based on the literature available as of that time.

II.B. EXPERIMENTAL EFFECTS

The purpose of this experiment was to test Ishimaru's predictions as reviewed in the preceding section. The experimental measurements are listed in Table I and along with qualitative photographs were subject to the parameters of the system as detailed in Table V. The results are broken into two sections, each of which presents data for moderate and strong turbulent conditions of the atmosphere. "Moderate turbulence" refers to the following condition on the predicted point source log-amplitude variance

$$\sigma_\chi^2 \leq 0.3$$

while "high" or "strong turbulence" was set by the criterion that

$$\sigma_\chi^2 \geq 1.0$$

Table V. Experimental Parameters

Pathlength: 1.4 km	
Path description: homogeneous farm land	
Transmitter height: 2 m	
Wavelength: 4880 Å	
Transmitter-beam configuration: large and focused large and diverged point source	see data
Transmitter focal adjustment resolution: 2.5 μm	
Receiver aperture: 0.6 cm	
Receiver bandwidth: 1 kHz	
Receiver dynamic range: > 80 db	
Receiver averaging time: 60 s	
Aperture smoothing receiver: 0.3 to 30 cm	
Resolution of spectral measurements: 1 Hz	
Microthermal-probe separation for C_n^2: 10 cm, horizontal	
Microthermal-probe height: 1.8 m	
Microthermal averaging time: 300 s	

The first section concerns itself with a qualitative understanding of the irradiance distribution of the beam wave. The second section provides quantitative measurements on distributions similar to those examples of the first section.

II.B.1 Qualitative Results

Under moderate turbulence conditions nearly diffraction limited propagation was obtained for the precisely focused beam. Fig. 16 provides a time-sequence of photographs exhibiting that negligible scintillation appeared within the central maximum of the intensity distribution. Outside the central portion of the beam the pattern evolved continually with time. As will be seen in the next section the predicted transmitter aperture averaging effect could not be measured, even though there is apparently no fluctuation observable on the interior part of the beam. This problem was the result of atmospherically induced wandering of the beam, as an additional and important effect. The time scale for this type of fluctuation was on the order of one second compared to the faster time scale of scintillation (10^{-1} to 10^{-2}s).

Fig. 17 yields the results of slight, intentional defocusing of the transmitter. As the transmitter was misadjusted, the intensity distribution changed from a nearly diffraction-limited condition to an array of independently scintillating patches. It appears that the breakup of the beam

Figure 16. Characteristic received beam for a focused, near-field transmitter in moderate turbulence. The duration of each frame was 4 ms; the time between adjacent frames was 21 ms. The sequence is downward in each column, and the scale marks represent 2.5 cm. λ = 4880Å, L= 1.4 km, D_T= 15 cm, $a_1 L$ = 0.09.

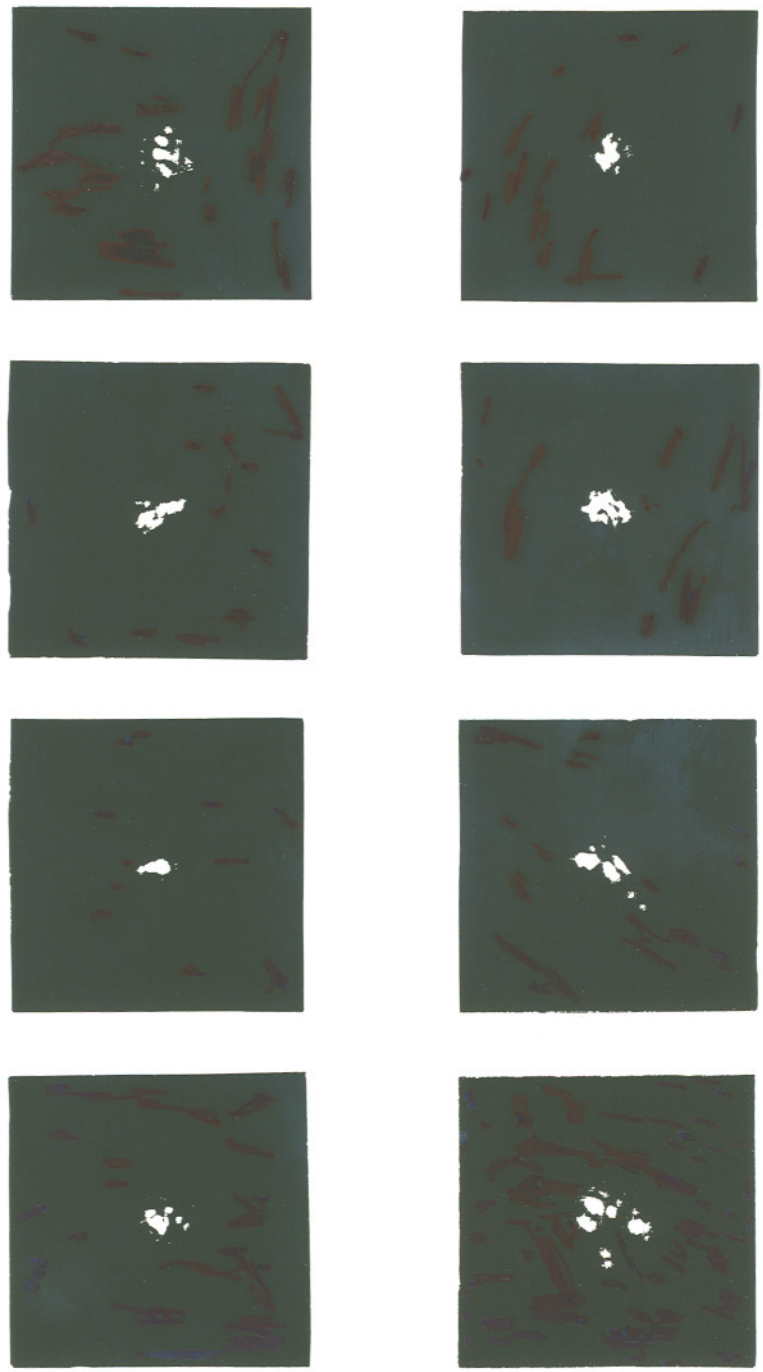

Figure 17. Received beam vs transmitter focal adjustment for the near-field transmitter of Fig.16 in moderate turbulence. Successive frames downward represent axial focal adjustments of 50μm compared to an effective focal length of 120 cm. Precise focus is illustrated in the third frame. Individual patches have the same nominal size as the central spot in Fig. 16.

is the mechanism that forces scintillation to increase beyond that of a point source under the same atmospheric conditions.

For conditions of sufficiently strong turbulence that would saturate point source fluctuations, the transmitter beam width in the target plane was many times the diffraction limited width. The intensity distribution consisted of an array of many independently scintillating patches whose diameters approximated the theoretical diffraction scale size of the transmitter aperture (Fig. 18). Obviously, there can be no transmitter averaging capabilities under such severe deterioration of the beam wavefront. These qualitative observations are corroborated by quantitative measurements discussed next.

II.B.2. Quantitative Results

II.B.2.a. Log-amplitude variance

Fig. 19 presents a type of bar graph for visualizing the effects of finite transmitter (and receiver) apertures on scintillation measurements. The actual values used in making the bar graph are listed in Table VI. Notice that the range of values given in the tables are illustrated by bars in the graph. Data include the measured log-amplitude variances for focused and diverged wavefronts in addition to virtual point source conditions. Each case is normalized by the nearly simultaneous measurement of the variance for the point source configuration, all of which were

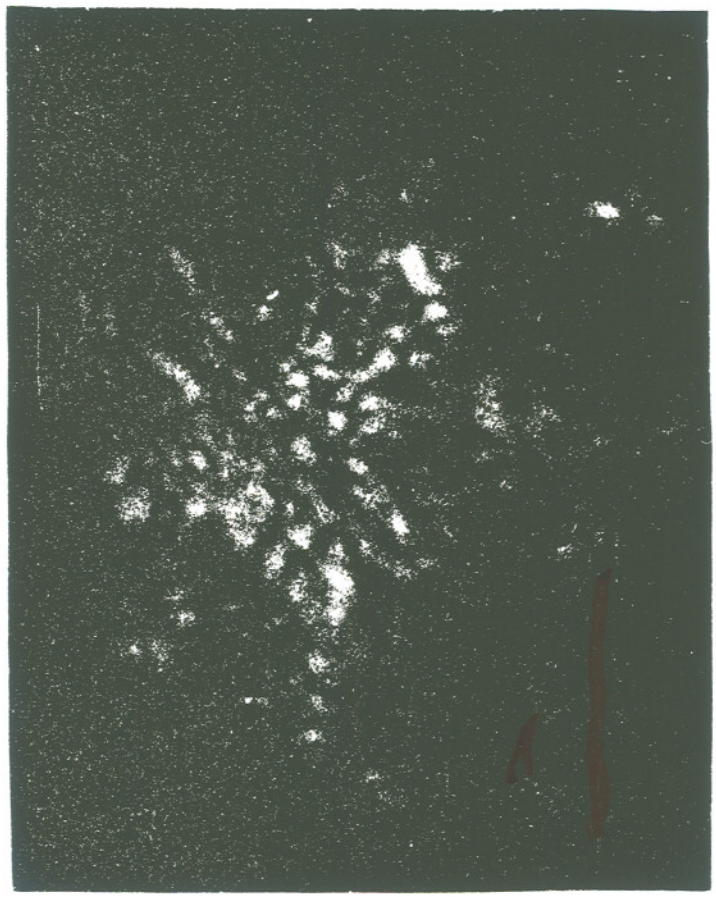

Figure 18. Received beam for the focused, near-field transmitter of Fig.16 in strong turbulence. Individual patches have the same nominal size as the central spot in Fig.16.

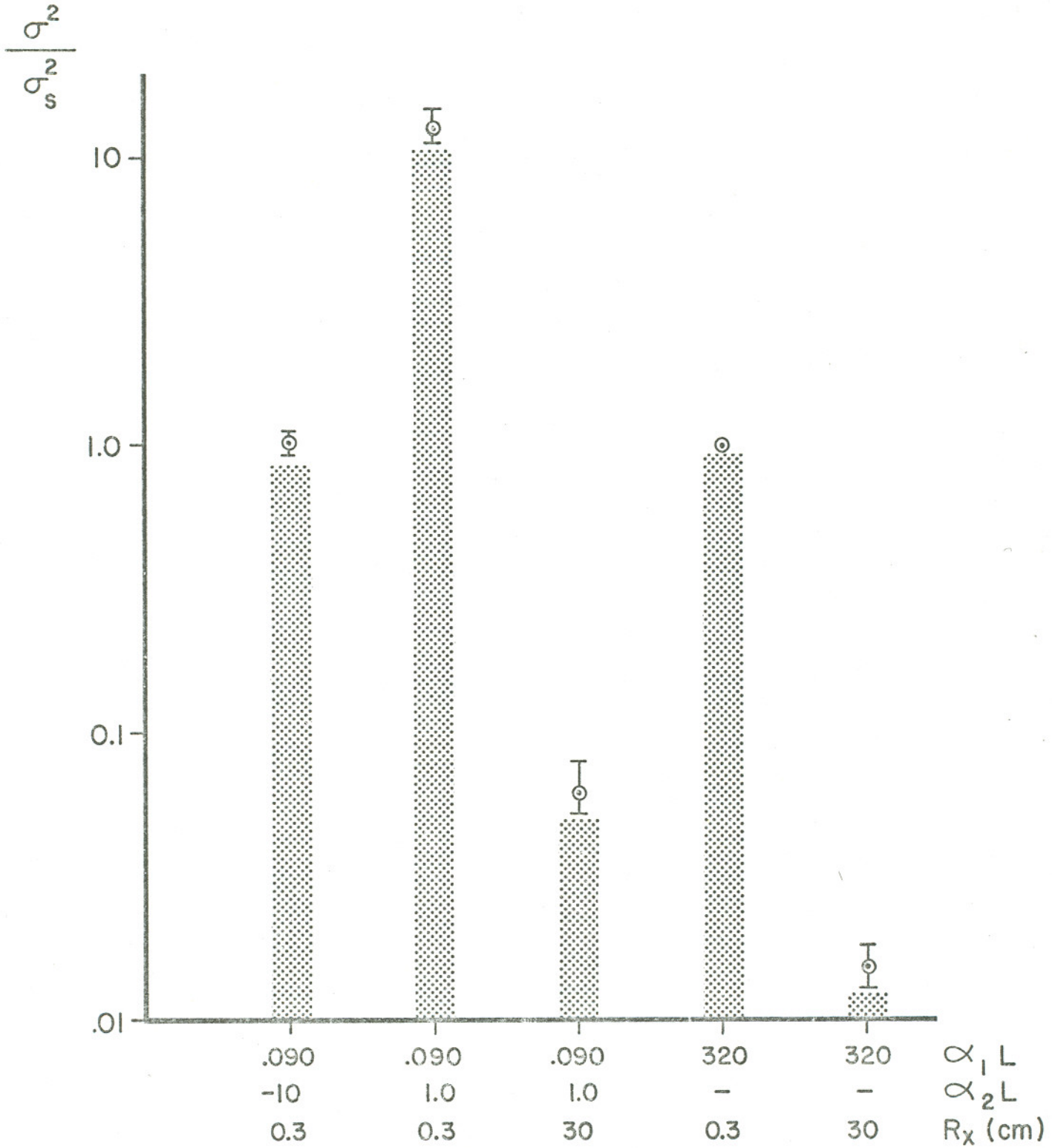

Figure 19. Normalized log-amplitude variance for moderate turbulence vs transmitter and receiver diameter and transmitter divergence. The range and average of a number of measurements made on different days are indicated. Each measurement is normalized by the variance obtained nearly simultaneously with a virtual point source and receiver. The large (15 cm) and small transmitter apertures correspond to ($\alpha_1 L$= 0.09, 320), respectively, whereas a diverging and focused beam correspond to ($\alpha_2 L$= -10, 1.0). The receiver diameter is denoted by R_x.

Table VI. Normalized Log-Amplitude Variance Measurements of Fig. 19

$a_1 L$	$a_2 L$	R_x (cm)	σ^2/σ_s^2 Range	Average
0.090	-10	0.3	0.91-1.12	1.00
0.090	1.0	0.3	11.2-14.6	12.2
0.090	1.0	30	0.052-0.079	0.061
320	...	0.3	...	1.00
320	...	30	0.013-0.018	0.015

unsaturated. Immediately evident is the fact that a large, diverged beam wave exhibited the characteristics of a point source. This was expected from the evaluations provided by Kerr and Eiss.[68] Surprisingly, for the second case, that of a large, focused beam, we observed fading an order of magnitude greater than measured for the point source. This effect is understood as the confined, nearly diffraction limited beam wandering about the target point detector. The sharp contrast between this result and the predicted reduction in fading indicates a deficiency in the theory introduced in the previous section. The remainder of the results included in Fig. 19 relate to the point source measurement and receiver aperture averaging, which will be discussed later.

Representative measurements for the strong turbulence case (saturated point source log-amplitude variance) are displayed in Fig. 20.

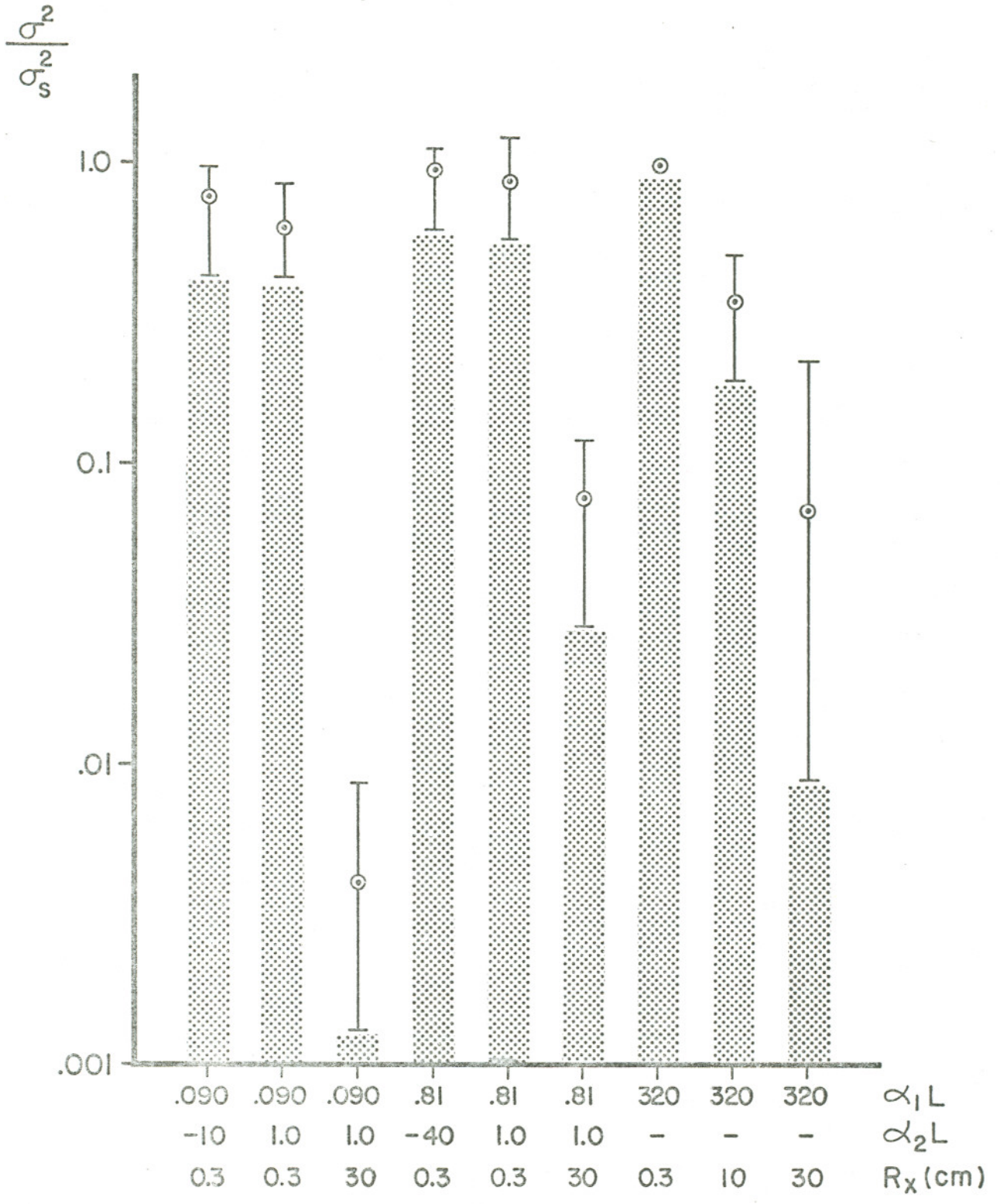

Figure 20. Measurements similar to those of Fig. 19, for strong turbulence.

The large, diverged transmitter produced a scintillation level just below that of the point source. Russian data[52] agrees with this result. The precisely focused beam provided scintillation similar to the case of the diverged transmitter. This was anticipated from observation of Fig. 18 which suggests that the atmospheric wavefront distortion was so drastic during strong turbulence that the shape of the transmitter wavefront was of little importance. The data suggests that wander was negligible because beam spreading by the atmosphere became emphasized. Fig. 20 also furnishes results from measurements on an intermediate size transmitter and the point source configuration. Actual values are summarized in Table VII.

Table VII. Normalized Log-Amplitude Variance Measurements of Fig. 20

$a_1 L$	$a_2 L$	R_x (cm)	σ^2/σ_s^2 Range	Average
0.090	-10	0.3	0.42-0.96	0.77
0.090	1.0	0.3	0.42-0.85	0.60
0.090	1.0	30	0.0013-0.0087	0.0040
0.81	-40	0.3	0.60-1.09	0.94
0.81	1.0	0.3	0.56-1.19	0.88
0.81	1.0	30	0.029-0.12	0.077
320	...	0.3	...	1.0
320	...	10	0.19-0.49	0.35
320	...	30	0.0089-0.22	0.070

II.B.2.b. Log-Amplitude Covariance

Under conditions of strong turbulence, the diffraction scale size of the large transmitter was observed to define the correlation scale size in the target plane. A typical measurement is given in Fig. 21. Of particular interest is the residual correlation tail of the point source covariance function which was observed in earlier experiments.[41] A summary of the correlation sizes, r_a, measured for different saturated conditions is furnished by the bar graph of Fig. 22. These illustrate substantial spread except in the case where the diffraction size of the transmitter defined the correlation size at the target plane. Table VIII lists the resulting numerical values.

Table VIII. Covariance Scale Sizes for Fig. 22

a_1L	a_2L	r_a (cm) Range	Average
0.090	-10	2.0-4.5	3.1
0.090	1.0	0.85-1.04	0.93
320	...	2.5-4.9	3.6

Fig. 23 indicates that during moderate turbulence wander had smeared the target plane distribution sufficiently to impair the measurement of the diffraction scale. Attendant with these moderate turbulence conditions was the lack of residual correlation for large separations in the point source covariance function.

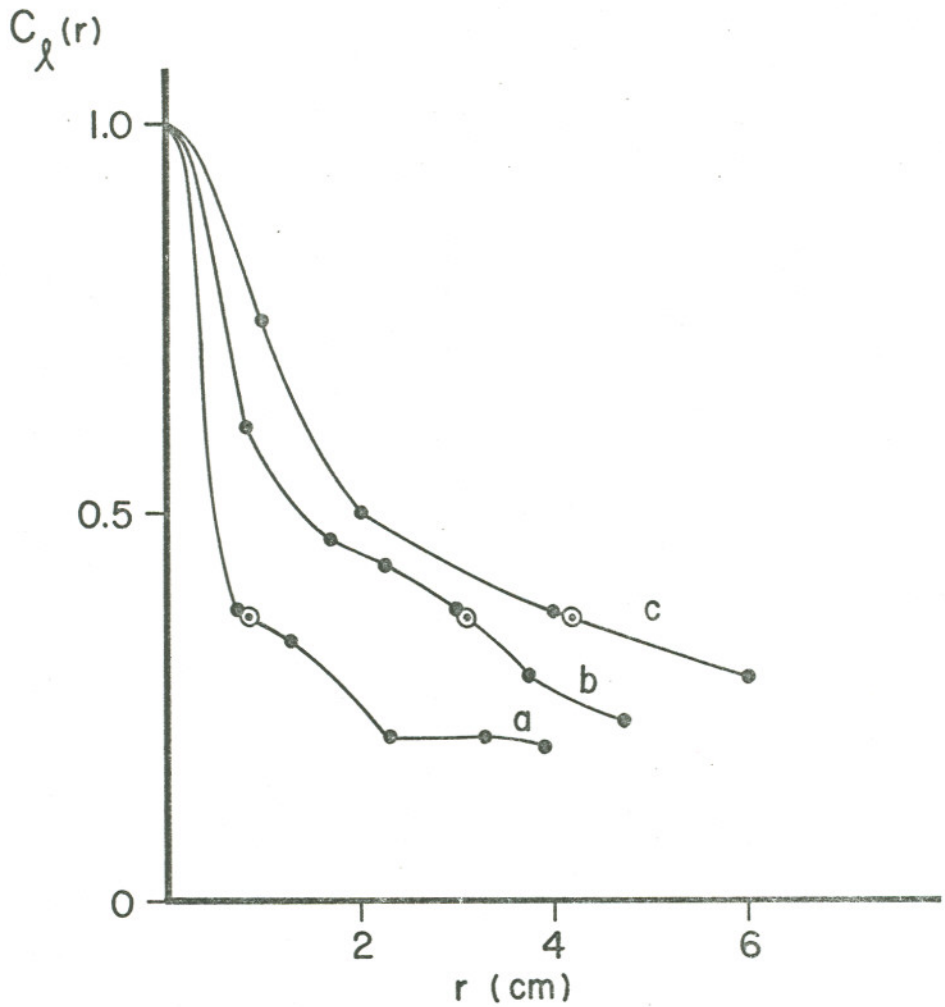

Figure 21. Typical log-amplitude-covariance curves for strong turbulence. The circles indicate the 1/e ordinate points. (a) Large, focused beam ($\alpha_1 L = 0.09$, $\alpha_2 L = 1.0$); (b) large divergent beam ($\alpha_1 L = 0.90$, $\alpha_2 L = -10$); (c) virtual point source ($\alpha_1 L = 320$).

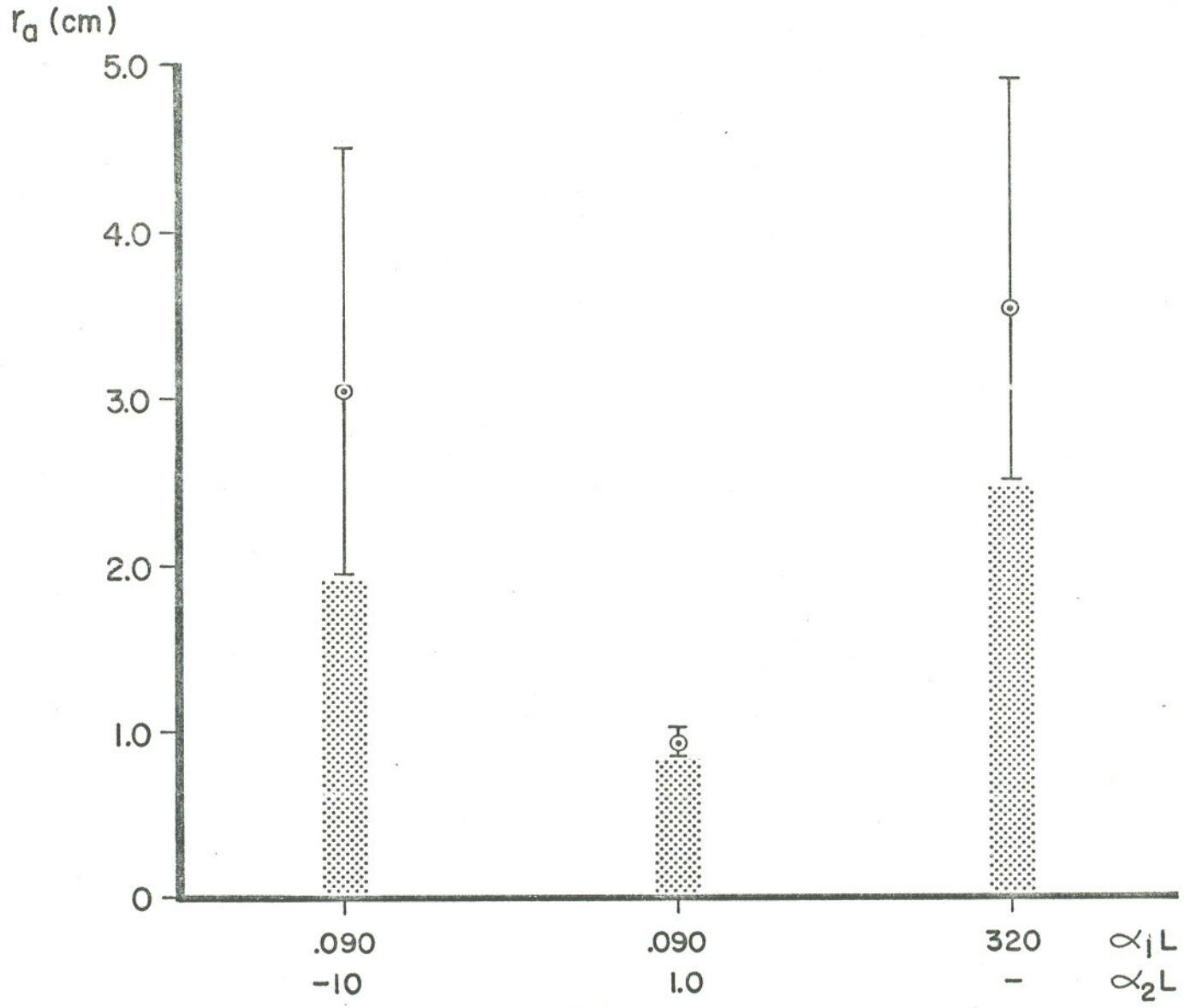

Figure 22. Covariance separations or e^{-1} points (r_a) vs transmitter conditions for strong turbulence. The range and average of a number of measurements of the type illustrated in Fig. 21 are indicated.

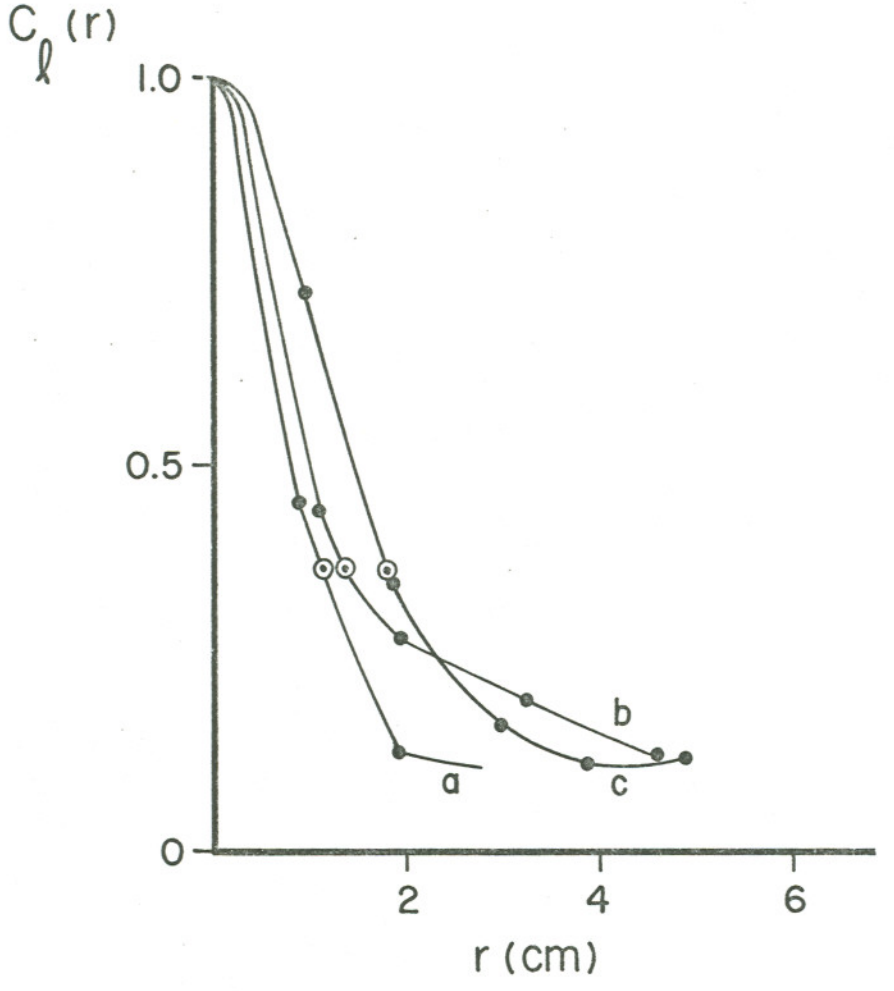

Figure 23. Measurements similar to those of Fig. 21 for moderate turbulence

II.B.2.c. Scintillation Spectra

Temporal spectra for the large focused transmitter case, Fig. 24, support the apparent lack of scintillation and the domination of slow wander effects by indicating that the spectral width was significantly less than that of the point source. These measurements are for the moderate turbulence regime, and we have defined the spectral width as the 1/e point of the normalized spectra. Representative numbers are furnished in Table IX.

Furthermore, the measurements during high turbulence substantiate the meaninglessness of a focused beam, as seen in Fig. 25. In fact, the spectral width for point receiver measurements of the large focused beam can be greater than that of the point source because of the finer correlation scale sizes defined by the transmitter diffraction effect. Fig. 25 is derived from the values listed in Table X.

II.B.2.d. Probability Distribution

When wander was important the scintillation probability distribution was apparently distorted from log-normal (Fig. 26). This situation occurred during moderate turbulence conditions. The obvious conclusion is that the predictions of Mitchell[76] do not pertain to confined beams subject to wander. The result must be the convolution of the log-normal distribution of scintillation and a different distribution for the wander phenomenon. This new distribution will be dominant whenever wander

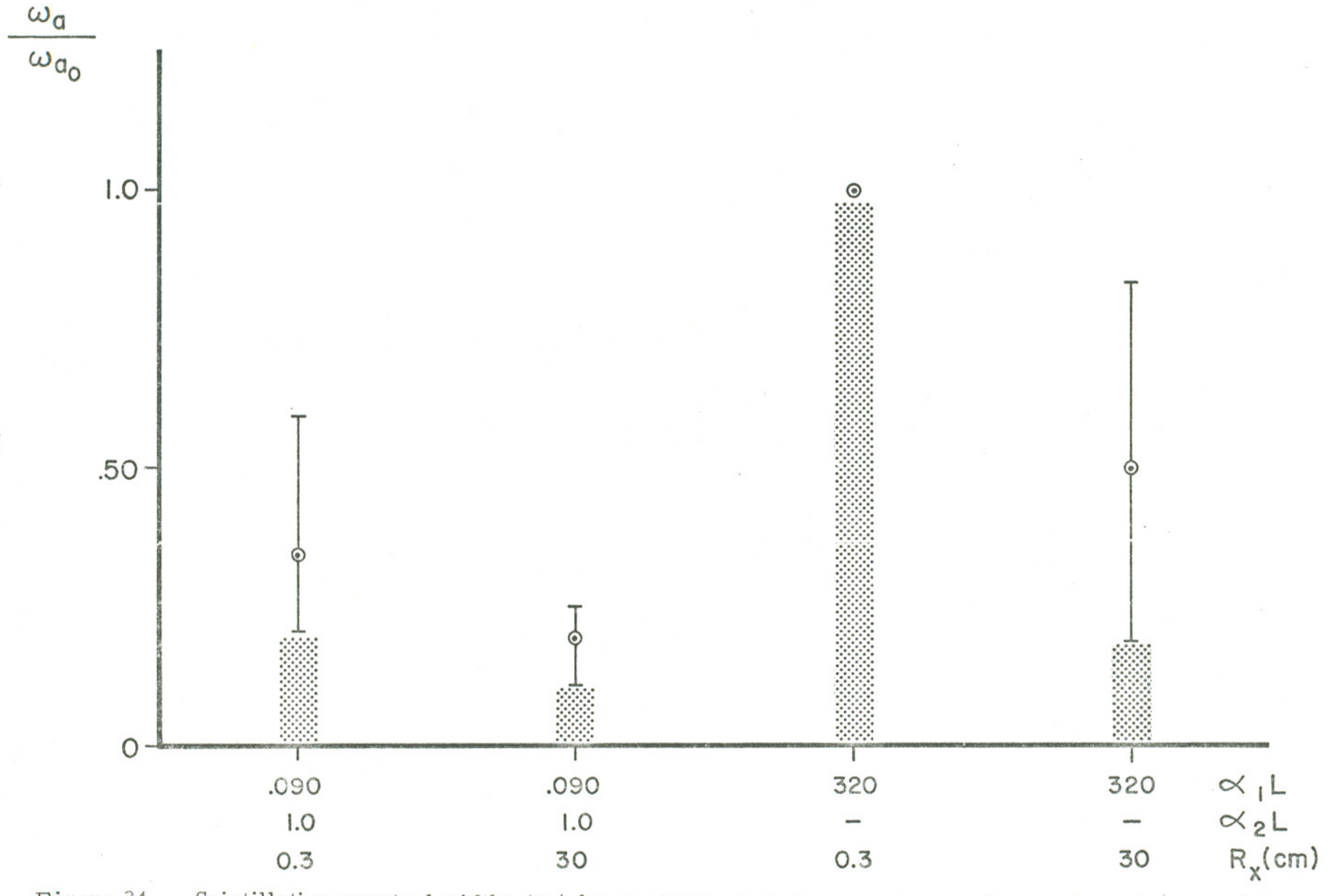

Figure 24. Scintillation spectral widths (ω_a) for moderate turbulence vs transmitter and receiver conditions. The range and average of a number of measurements made on different days are indicated. Each measurement is normalized by that obtained nearly simultaneously with a virtual point source and receiver.

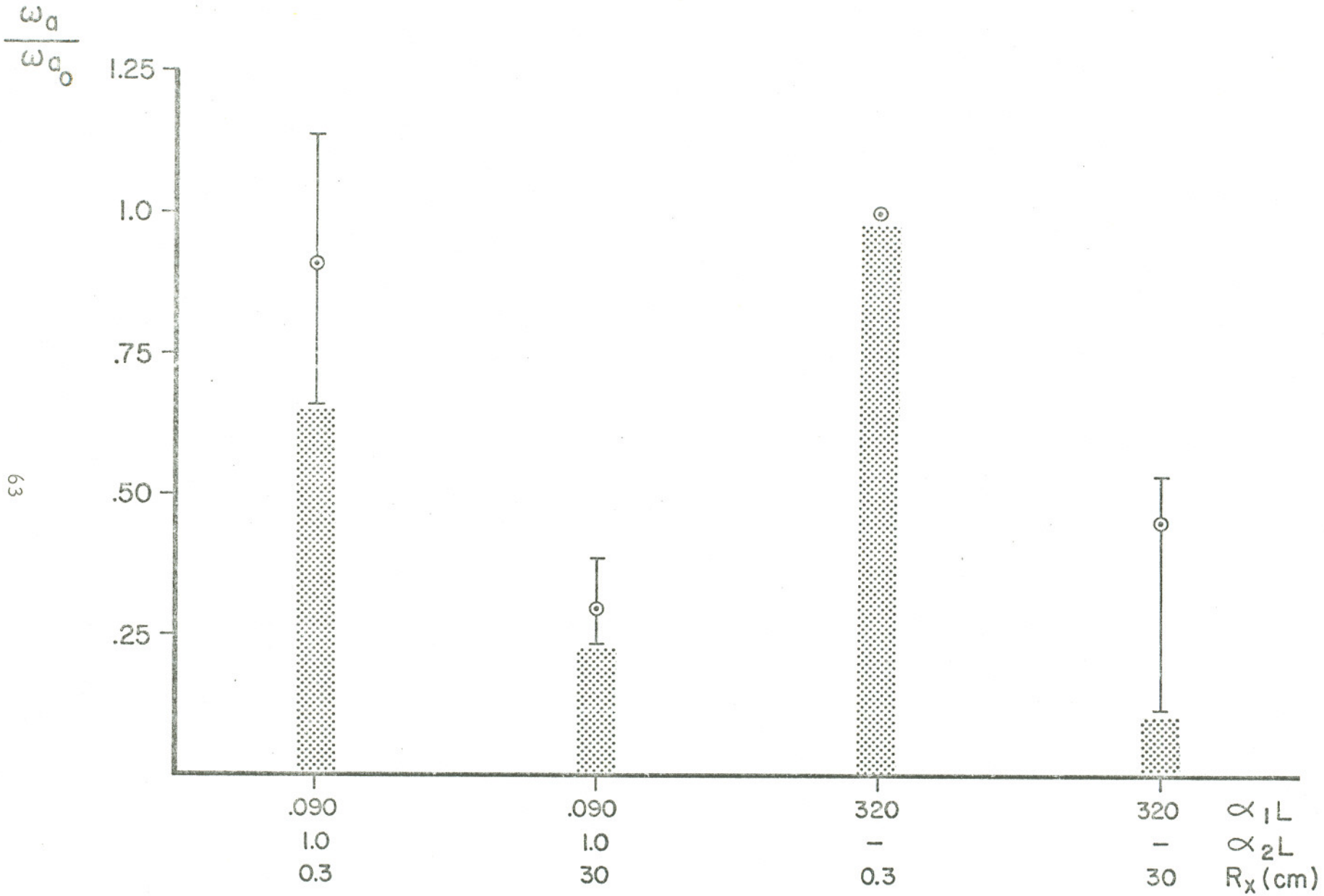

Figure 25. Measurements similar to those of Fig. 24, for strong turbulence.

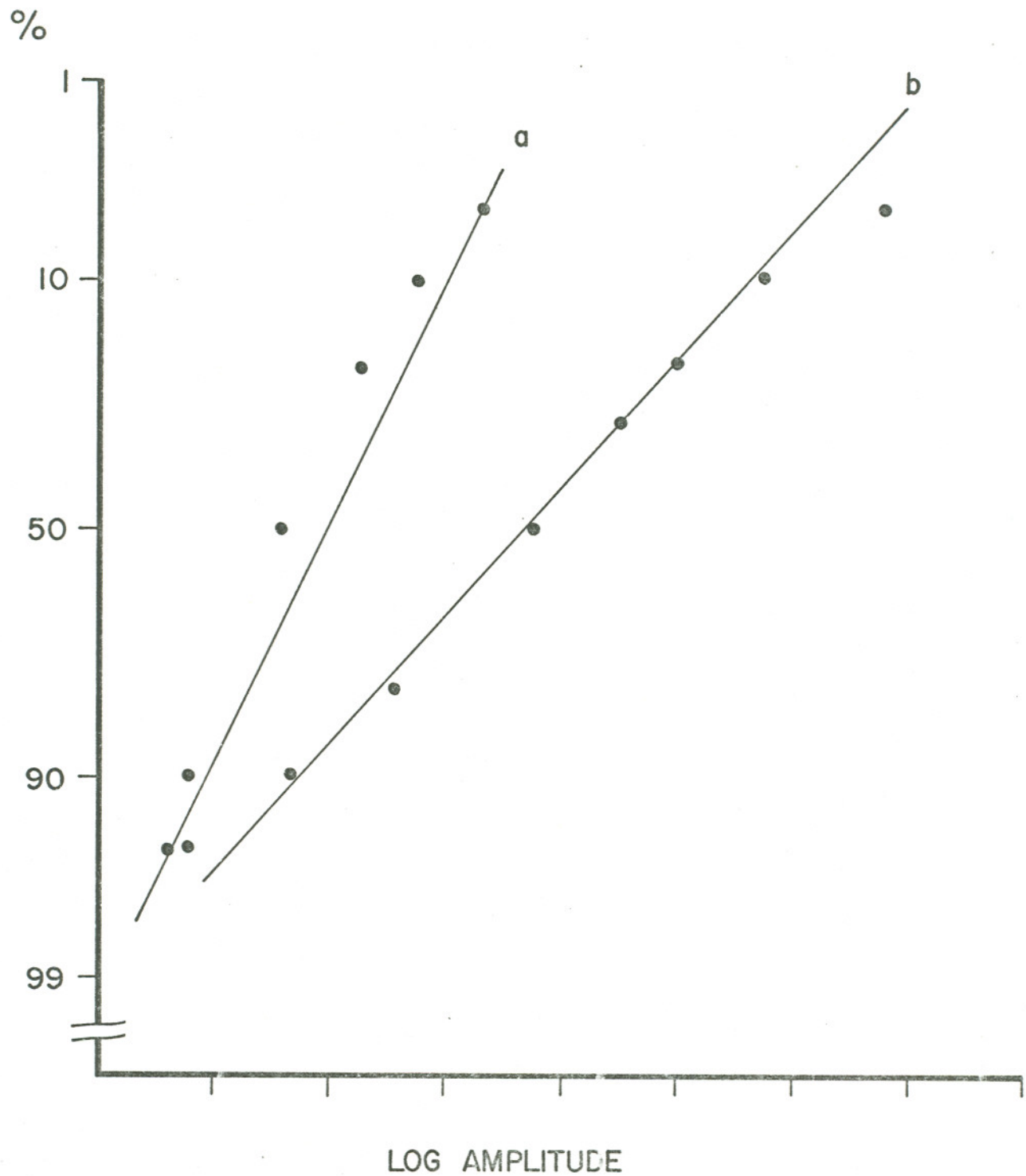

Figure 26. Cumulative probability distributions for a large, focused beam (a_1L= 0.09, a_2L=1.0) under conditions of predominant beam wander. The wander causes significant departures from log normality. (a) Small receiver (R_x=0.3 cm); abscissa:0.5 increment of log irradiance per division. (b) large receiver (R_x=30 cm); abscissa: 0.005 increment of log irradiance per division.

Table IX. Scintillation Spectral Widths of Fig. 24

a_1L	a_2L	R_x (cm)	ω_a/ω_{ao} Range	ω_a/ω_{ao} Average
0.090	1.0	0.3	0.20-0.59	0.34
0.090	1.0	30	0.11-0.25	0.19
320	...	0.3	...	1.0
320	...	30	0.18-0.83	0.50

Table X. Scintillation Spectral Widths of Fig. 25

a_1L	a_2L	R_x (cm)	ω_a/ω_{ao} Range	ω_a/ω_{ao} Average
0.090	1.0	0.3	0.66-1.14	0.91
0.090	1.0	30	0.23-0.39	0.30
320	...	0.3	...	1.0
320	...	30	0.12-0.53	0.45

is the dominant fade mechanism. However, as the beam breaks up (broadens) wander becomes less important, and the fluctuations once again become log-normal as are those of the point source (Fig. 27).

II.B.2.e. Receiver Aperture Averaging

From Fig. 19 we observe that during weak turbulence wander also had a detrimental effect on receiver aperture averaging, causing the averaging advantage to be less than that for a point source. This is further supported by the fact that the scintillation spectra for the finite beam and the large receiver contained lower frequency components than did the spectra for the point source (Fig. 24).

On the other hand, during strong turbulence, Fig. 20 shows that receiver aperture averaging was much more effective on the beam wave source than on the point source. This enhanced advantage originates from the fact that the correlation size of the finite beam was smaller than the correlation size of the point source (Fig. 22), thus giving rise to more efficient spatial averaging. Furthermore, the spectra of Fig. 25 for the finite beam wave and the large receiver show that wander became negligible during strong turbulence and the spectral width was indicative of point source fading as supported by previously discussed qualitative and quantitative data.

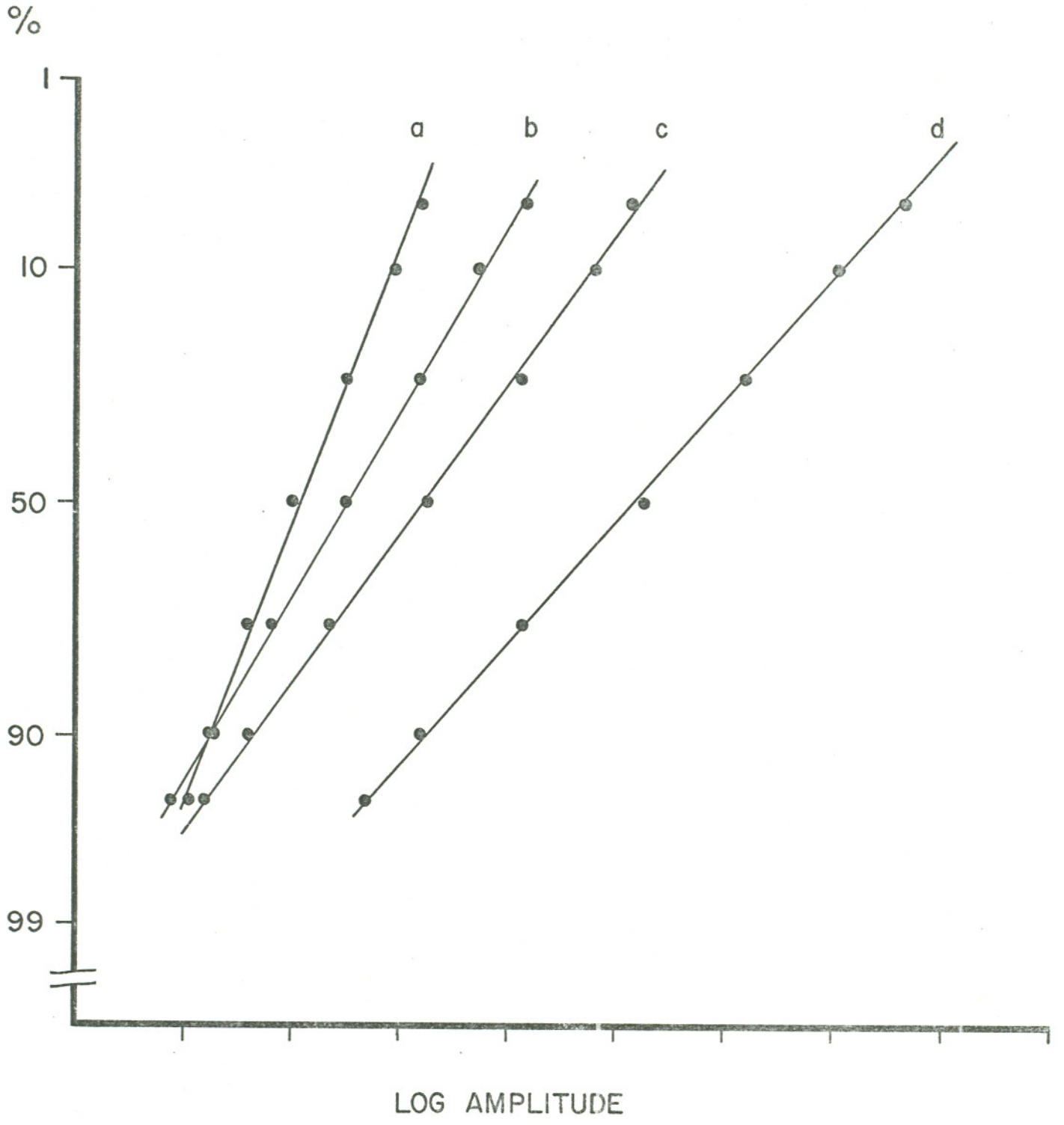

Figure 27. Cumulative probability distributions vs transmitter and receiver conditions. These examples indicate good log normality. (a) Large, focused beam (a_1L=0.09, a_2L=1.0); large receiver (diameter R_x=30 cm); abscissa:0.005 increment of log irradiance per division. (b) Large, focused beam (a_1L=0.09, a_2L=1.0); small receiver (R_x=0.3 cm); abscissa:0.5 increment of log irradiance per division. (c) virtual point source (a_1L=320); small receiver (R_x=0.3 cm); abscissa:0.5 increment of log irradiance per division. (d) virtual point source (a_1L=320); large receiver (R_x=30 cm); abscissa: 0.005 increment of log irradiance per division.

II.C. CONCLUSION

With respect to the log-amplitude variance, the previous section found that under moderate turbulence conditions beam wave effects were more detrimental than those of a point source. The primary reason for not observing transmitter aperture averaging was that atmospherically induced wander steered the beam (nearly diffraction-limited) randomly about the receiver in the target plane. On the other hand, during strong turbulence the wavefront of the large transmitter became so distorted that the measured variance was nearly indistinguishable from that of a point source. Corresponding effects were seen in the temporal spectra. The fluctuations were predominantly slower (wander) for weak turbulence and faster (beam break-up) for strong turbulence than those of a point source.

Moreover, measurements of the log-amplitude covariance function indicated that the transmitter diffraction width was the important scale size in the spatial distribution, regardless of the strength of turbulence. This covariance scale size (finer than that of the point source) provided better large receiver aperture smoothing — but only during strong turbulence when atmospherically induced beamspread was sufficient to make wander insignificant. During moderate turbulence, wander destroyed the large receiver's ability to smooth beam wave fluctuations as efficiently as it could for a point source.

Hence the initial hypothesis that beam waves could aid the reduction of optical carrier fluctuations appears false. The inescapable conclusion is that a more general and comprehensive view of beam wave propagation must be utilized. Such a theory and its experimental verification are discussed in the next chapter.

CHAPTER III. PROPAGATION OF A FOCUSED BEAM WAVE WITH WANDER CANCELLATION

INTRODUCTION

The last experiment that was discussed indicated that a passive beam wave optical carrier offerred no advantage over a point source when atmospherically induced fluctuations were evaluated. In fact, it was pointed out that for weak turbulence, the fading of a point source was less than that of the beam wave. This indicates a serious deficiency in the Rytov approach (smooth perturbation method) to the propagation theory for laser radiation. The wander phenomenon was completely left out. However, if the wandering of the beam could be cancelled, then it appeared that the Rytov approach might possibly be valid. Hence, it is the goal of the experiment discussed in this chapter to (1) test the Rytov predictions under conditions during which wander is cancelled and to (2) test a new, unified approach to beam wave propagation that is sufficiently comprehensive to include the wander phenomenon – the extended Huygens-Fresnel method.[77]

A key factor in accomplishing these experimental goals was the development of a fast-tracking laser transmitter.[78] This system, whose design is detailed in Appendix I, is capable of cancelling beam wander in the target plane, thus allowing a fundamental test of the predictions of Ishimaru. In addition, utilization of the "reciprocity" tracker permits

collection of all the basic data necessary to test the new, comprehensive beam wave propagation theory. When the system is not tracking, the measurements correspond to long-term averages for the on-axis mean irradiance and variance. On the other hand, if the system is tracking out wander, then the measurements relate to what is called short-term averaging. In the following sections of this chapter a condensed review of the new theoretical approach is discussed. First, the semiquantitative method is presented. The long- and short-term averages of the resulting quantities agree assymptotically with the exact Huygens-Fresnel equations that are given in the second section. Then in a final section, experimental tests of this new approach are provided.

III.A. THEORY, A UNIFIED SEMIQUANTITATIVE APPROACH

In contrast to application of the method of smooth perturbations to the beam wave propagation problem, there is a linear systems type of analysis that, fortunately, does include the wander phenomenon. The method applies a modified Huygens-Fresnel principle[35] in which a reciprocity theorem[79,80] is utilized. Then if the mutual coherence function (MCF)[81] or the modulation transfer function (MTF)[82] is known for a point source through the perturbing medium, the medium's effect on any input can, in principle, be calculated.[83,84] Moment generating techniques are used to find the higher moment effects.

Authors using this systems approach or other methods seem to agree in concept or under certain limits, but otherwise detailed comparison is difficult.[8,85-91] Approximations and definitions become vague and misused.[92,93] Previous approaches to the finite beam problem did add physical insight but have also caused confusion because the works were published without care in stating two basic facts:

(1) Definition of beamspread, i.e., does it include wander and instantaneous spread (long-term spread) or just instantaneous spread (short-term spread).

(2) Conditions of validity as specified by the relative sizes of the independent variables.

And to further complicate matters related to problem (1), there have been four basic definitions used to study spread:[93]

(a) 1/2 power radius, r'_L at L on axis by

$$\langle I(r'_L, L)\rangle = (0.5)\langle I(0, L)\rangle \tag{9}$$

(b) 0th moment radius, r''_L

$$r''^2_L = \int d\vec{\rho}\ \langle I(\vec{\rho}, L)\rangle \Big/ \langle I(0, L)\rangle \tag{10}$$

(c) 2nd moment radius, r'''_L

$$r'''^2_L = \int d\vec{\rho}\ \rho^2 \langle I(\vec{\rho}, L)\rangle \Big/ \int d\vec{\rho}\ I(\vec{\rho}, L)\rangle \tag{11}$$

(d) I^2 definitions, r_L^{iv}

$$r_L^{iv\,2} = \left(\int d\vec{\rho} \, \langle I(\vec{\rho}, L) \rangle \right)^2 \Big/ \int d\vec{\rho} \, \langle I^2 (\vec{\rho}, L) \rangle \tag{12}$$

The question of whether or not the proposed definition includes wander depends on the effective averaging time or the form of the wave structure function, $D_s(\rho)$, that is applied.[10,12]

In answer to this confusion, Kerr proposed a unified, semiquantitative approach that began with the most general expression of the modified Huygens-Fresnel principle. The fundamental effect of beamspread is coded into an on-axis mean-irradiance measure. Secondly, he set up an organized listing of the physical conditions on the variables that were useful for evaluation purposes. His report, Ref. 74, provides the set of physical conditions for recognizing and/or defining the finite beam wave effects of wander, instantaneous spread and long-term spread. In addition, many of these limits had not yet been qualified to their proper region of validity. In fact, some of the conditions had not been previously recognized in full and hence resulted in some of the earlier confusion in the field.

Kerr collects the evaluations of image resolution, optical heterodyne receiver analysis and Rytov work to develop (via reciprocity arguments) the assymptotic behavior of the exact expressions for beam wave effects. Further, it can be shown that this semiquantitative approach is consistent with other authors' systems-developments by evaluating the exact

Huygens-Fresnel equations. Moment techniques applied to these basic expressions (with related approximations) then allow analysis of all important statistics related to the beam wave problem. This new, unified approach to finite beam propagation is presented by discussing its basic equations and basic quantities and conditions in the next two sections.

III.A.1. Basic Quantities and Conditions

The fundamental experiment may be envisioned as a laser transmitter with an e^{-1} amplitude diameter of D_g transmitting an optical carrier at a wavenumber k over a pathlength L. With this arrangement, there are two physical conditions immediately recognized: we will be concerned with approximations dealing with near field conditions ($D_g > \sqrt{L/k}$) and far field conditions ($D_g < \sqrt{L/k}$). These regions are of fundamental interest because they change the weighting of the wave structure function,[10] which is of ultimate importance.

The wave structure function is of fundamental significance due to the fact that it is utilized to define the MCF and the MTF of the random medium. For instance, the long term MTF[94] is given by

$$M_{LT}(\rho) = e^{-1/2\, D_s(\rho)} \tag{13}$$

Usually, the approximation is made that the wave structure function is just the phase structure function,[95] and by the above NF/FF conditions, we realize that the most error that results is a factor of 2. In an effort to parametize MTF considerations, it is typical to write the MTF in the form[12]

$$M_{LT}(\rho) = e^{-(\rho/\rho_o)^{5/3}} \tag{14}$$

where ρ_o is the transverse coherence scale size owing to atmospheric turbulence. ρ_o is defined by the condition such that[35]

$$D_s(\rho_o) = 2 \tag{15}$$

Since the theoretical considerations in deriving the MTF via the wave structure function involve approximations concerning the spatial spectrum of the turbulent field, one is forced to bring the inner and outer scales of the turbulence spectrum into the list of important parameters. Automatically, one must then deal with conditions related to the relative sizes of the outer scale (L_o), the inner scale (ℓ_o) and the transverse coherence scale (and in some cases the relative size of k.[77] In conclusion there are two fundamental sets (NF or FF) of nine inequalities related to L_o, ℓ_o and ρ_o[74] that affect the basic equations.

III.A.2. Basic Equations, 1st Moment and 2nd Moment

The spreading effects of turbulence on a propagating beam wave can be broken into two problems due to the disparate time scale of the effects: wander-related spreading (a slow phenomenon) and beam breakup spreading (a fast phenomenon). Using an assumption that the spread angles can be separated into discrete components, one defines the long-term mean square beamspread to be

$$\theta_{LT}^2 = \theta_o^2 + \theta_{INST}^2 + \Phi^2 \tag{16}$$

where θ_o^2 is the fundamental spread of the beam as defined by diffraction. Φ^2 is the mean square beamspread due to the wander phenomenon, and θ_{INST}^2 is the mean square instantaneous spread due to a beam breakup process.

It has been suggested that the wander problem is a slow phenomenon and nearly uncoupled from instantaneous beamspread.[96] Hence, there is the possibility of cancelling this particular spreading component. If wander is cancelled, then the residual beamspread is called the short-term beamspread and is given by

$$\theta_{ST}^2 = \theta_o^2 + \theta_{INST}^2 \tag{17}$$

These beamspread expressions can be tested with the fast-tracking laser transmitter by measuring the on-axis mean irradiance for the non-tracked (long-term spread) and the tracked (short-term spread) states of the system. We have operated the equipment with the receiver in the NF of the transmitter and under a wide range of turbulence levels to unveil any special parametric dependencies on ρ_o. Hence the detailed approximations of spread as a function of D_g/ρ_o are certainly of interest. Ref. 77 derives the reduced on-axis mean irradiance that results from atmospheric beamspreading

$$\bar{I}_{LT}/\bar{I}_o = \frac{1}{1+\left[C_2\left(\frac{D_g}{2\rho_o}\right)^{1/3} + 3.63\right]\frac{D_g^2}{4\rho_o^2}} \tag{18}$$

We have specialized to the NF, focused case, and normalization is chosen for applying ρ_o as the variable parameter with D being fixed. When C_2 is zero this expression describes the on-axis mean irradiance for the non-tracked case (long-term average) normalized by the on-axis mean irradiance for diffraction-limited operation ($\bar{I}_o$). However, during the tracked case (short-term average) the total spread is reduced by taking $C_2 = (-3.44)$. The coefficients of the terms were chosen to cause this mean irradiance argument to agree with the detailed Huygens-Fresnel equations for image resolution, heterodyne receiver analysis and coherent transmitters under appropriate limiting conditions. Immediately obvious from this expression is that the mean irradiance will be proportional to ρ_o^{+2} when $D_g > \rho_o$. In addition, for $D_g < \rho_o$ the diffraction effect will dominate.

The consequences of fluctuations about the mean irradiance levels suggested by the unified approach are best described by the normalized variance of the linear irradiance. The general approach is to identify three mechanisms

$$\sigma_I^2 = A_1\sigma_w^2 + A_2\sigma_R^2 + A_3\sigma_c^2 \tag{19}$$

where σ_w^2 is the wander induced component; σ_R^2 comes from first-order theory (Rytov approach); and σ_c^2 is due to coherent fading (beam break-up). The detailed expression can be found in Ref. 77. In addition, the important break point definitions related to the component weighting through

coefficients A_i are given. Fig. 28 shows a semiquantitative graph of Eq. 19 for normalization to the case where ρ_o is varied and D_g is constant.

The probability distribution of the above fluctuations can be very complicated.[97] Reciprocal arguments indicate that the wander angle will exhibit a gaussian distribution[12], consequently causing a modified beta distribution in the received power or intensity fluctuations.[98] Fried[99] translates these linear intensity fluctuations to log intensity fluctuations to find an exponential distribution. Fried further indicates that when both wander and scintillation are important the resulting log-intensity fading distribution is a convolution of the exponential and the normal distributions. For the coherent fading case the distribution and its effects are not analytically described, but it is apparent from Chapter II that once the beam is entirely broken up the statistics are log-normal.

The salient features of the temporal spectra of these fluctuations are best described by recognizing two spectral regions. As indicated earlier, wander is a slow phenomenon, and as such will produce peaks below a few Hz.[100] On the other hand, scintillation spectral components can extent to several hundred Hz.[41]

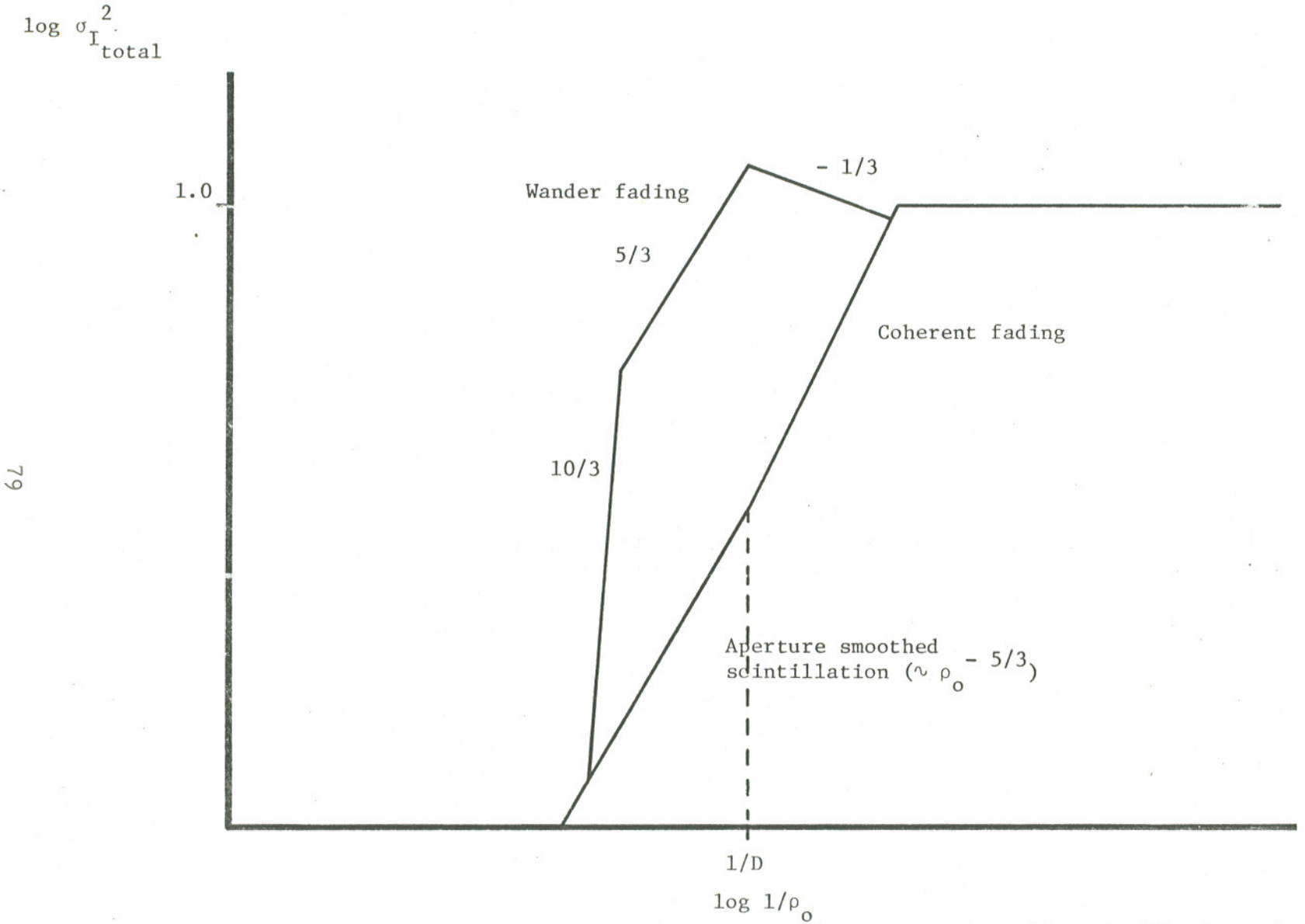

Figure 28. Normalized variance of the linear irradiance vs. coherence scale, with and without wander cancellation, (Ref. 77).

Ishimaru[66,67] has attempted to describe the spectra of scintillation for finite apertures, and found the roll-off to be $f^{-8/3}$ for the assumptions of zero inner scale and large f. Others[12,52,56,101,102] have considered the form for classical waves, and these descriptions may apply for certain conditions such as high turbulence.

Reciprocal arguments can be applied to the wander spectral analysis to indicate that it is essentially identical to the spectral analysis of the angle of arrival problem (phase difference fluctuations) for a two point interferometer whose separation is equivalent to our telescope diameter.[103] Huber[104] summarizes the conditions as listed here:

$$\begin{aligned} &f^{-2/3} \quad \text{if} \quad f, < f < f_2 \\ &f^{-8/3} \quad \text{if} \quad f > f_2 \\ &f_1 \equiv \frac{\nu}{2\pi L_o} \quad ; \quad f_2 \equiv \frac{\sqrt{6}\,\nu}{2\pi D} \end{aligned} \tag{20}$$

where D is indicative of the aperture diameter, ν is the wind speed perpendicular to the propagation path and L_o is the outer scale.

In addition, Clifford[102] gives the form of the frequency weighted spectrum for the angle of arrival as $f^{-5/3}$.

It is suggested that these expressions apply only in an approximate sense due to the finite receiver averaging effect on the phase difference fluctuations over the entire aperture.[105] A more rigorous approach would

use the results of Rheinhardt and Collins[106] by applying the proper filter function modifications.

All or a portion of each of the effects described above can be tested by the data received during the use of the fast-tracking transmitter. However, before discussing the resulting data, it is interesting to compare the semiquantitative results given above with what can be found from exact Huygens-Fresnel expressions.

III. B. EXACT HUYGENS-FRESNEL EXPRESSIONS

III.B.1. The First Moment

The fundamental expression for the on-axis, long-term mean irradiance via the extended Huygens-Fresnel method is provided by Lutomirski and Yura[35]

$$\bar{I}_{LT} = \left(\frac{k}{2\pi z}\right)^2 \int d\vec{\rho}\, M_{LT}(\vec{\rho}, z) e^{-\frac{ik}{z}\vec{p}\cdot\vec{\rho}} \int d\vec{r}\; U(\vec{r}+\vec{\rho}/2)\, U^*(\vec{r}-\vec{\rho}/2) e^{\frac{ik}{z}\vec{\rho}\cdot\vec{r}} \tag{21}$$

where they have defined the following quantities:

k = the optical carrier wavenumber

z = the propagation distance

$M_{LT}(\rho, z)$ = the long term MTF for a spherical wave through the perturbing medium

$U(\vec{r})$ = the amplitude illumination function of the transmitter

A detailed analysis of the gaussian weighted laser transmitter problem is given by Yura,[107] while Kerr[77] specializes the considerations directly to the NF and focused case. They apply equations for the untruncated beam. A numerical evaluation of the appropriate normalized expression for the on-axis, long-term mean irradiance

$$\frac{\bar{I}_{LT}}{\bar{I}_o} = 2\int_0^\infty dx\ xe^{-x^2}\ e^{-(D_g x/\rho_o)^{5/3}} \tag{22}$$

is given in Fig. 29, in addition to results from the earlier semiquantitative analysis. D_g is defined as the e^{-1} amplitude diameter of the untruncated gaussian beam. We would like to plot Fried's reciprocal results[94,108] on this same figure, but two problems arise. (1) In the transmitter case the expressions are parameterized by ρ_o while in the imaging case the parametric effects are referred to r_o. (2) In addition, the aperture weighting is different for the two situations: uniform for the image case; gaussian for the transmitter case. Once these two differences are resolved, the reciprocal results of image analysis can be compared with the evaluation of Eq. 22. Additional problems will occur when we attempt to compare Eq. 22 with our experimental data which is inherently a hybrid of the uniform and the untruncated gaussian weighting cases, i.e., a truncated gaussian beam.

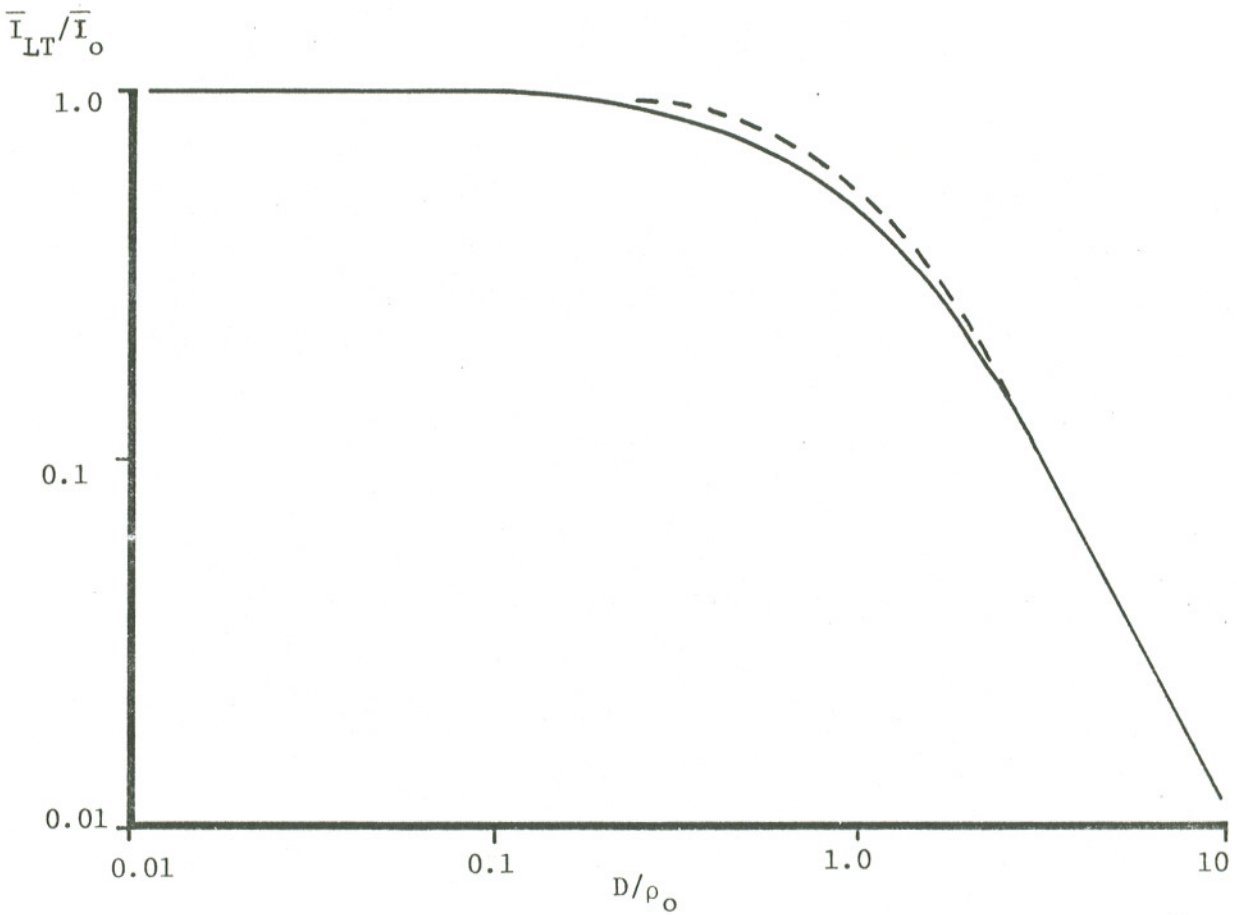

Figure 29. Theoretical $\bar{I}_{LT}/\bar{I}_o$ from Eq. (22) (———) and points from Eq. (18) with $C_2 = 0$ (-----).

To detail how the resolution of these difficulties was obtained we first note $r_o = (2.0986)\rho_o$. Secondly, Fried[94] provides sufficient information to derive

$$\frac{R_\infty}{R_{max}} = \frac{r_o^2}{D^2} \tag{23}$$

for the uniformly weighted aperture of diameter D. The parameters R_∞ and R_{max} relate to the image resolution of an optical system as described in Ref. 94. However, after comparison of Fried's equations with Eq. 22 for the untruncated gaussian case, we find

$$\frac{R_\infty}{R_{max}} = \frac{\bar{I}_{LT(\xi \to \infty)}}{\bar{I}_{LT(\xi \to 0)}} \tag{24}$$

where ξ is the diameter of an aperture truncating the gaussian beam. So

$$\frac{r_o^2}{D^2} = \frac{\bar{I}_{LT(\xi \to \infty)}}{\bar{I}_{LT(\xi \to o)}} \tag{25}$$

If we evaluate the RHS of Eq. 25 when truncation is important, then we will obtain the connection between the purely uniform, the truncated gaussian and the untruncated gaussian cases.

Consider the denominator of Eq. 25. The formal expression is

$$\bar{I}_{LT(\xi \to o)} = \lim_{\xi \to o} 2I_o \int_o^{\xi/D_g} dx\, x e^{-x^2} e^{-\left(\frac{D_g x}{\rho_o}\right)^{5/3}} \tag{26}$$

But if we recognize that the condition $\xi \to o$ is equivalent to $\rho_o \to \infty$, diffraction-limited operation is indicated. The evaluation of this when truncation effects are important is provided by Olaofe[109]

$$\overline{I}_{LT(\xi \to o)} = \frac{A}{4} D_g^4 \left(1 - e^{-\eta/2}\right)^2 \tag{27}$$

where $\eta = (\xi/D_g)^2$. To evaluate the exact form of the constant (A) we can consult Yura. From the appendix of Ref. 107 we calculate that for no truncation

$$I_o = \frac{k^2 D_g^4}{16z^2} \left|U_o\right|^2 \tag{28}$$

Comparing Eqs. 27 and 28, we obtain the following equation

$$\overline{I}_{LT(\xi \to o)} = \frac{k^2 \left|U_o\right|^2}{16z^2} D_g^4 \left(1-e^{-\eta/2}\right)^2 \tag{29}$$

The formal expression for the numerator of Eq. 25 is given by

$$\overline{I}_{LT(\xi \to \infty)} = \lim_{D \to \infty} 2I_o \int_o^{\xi/D_g} dx\, x e^{-x^2} e^{-\left(\frac{D_g x}{\rho_o}\right)^{5/3}} \tag{30}$$

We can show that this becomes

$$\overline{I}_{LT(\xi \to \infty)} = 2I_o \left[3/5 \left(\rho_o^2/D_g^2\right) \Gamma(6/5)\right] \tag{31}$$

or applying Eq. 28

$$\overline{I}_{LT(\xi \to \infty)} = (1.102) \frac{k^2 D_g^4 \left|U_o\right|^2}{16z^2} \left(\rho_o^2/D_g^2\right) \tag{32}$$

It is fundamental to recognize that Eq. 32 pertains to the untruncated gaussian case. If we are to allow truncation, Eq. 32 must be normalized for power loss to a truncating aperture about the gaussian beam. This normalizing factor is provided by Titterton, et al.,[110] and Eq. 32 becomes

$$\overline{I}_{LT(\xi \to \infty)} = (1.102) \frac{U_o^2 k^2 D_g^2 \rho_o^2}{16 z^2} (1-e^{-\eta}) \tag{33}$$

Combining Eqs. 33, 29, and 25 we find

$$\frac{r_o^2}{D^2} = \frac{(1.102)(1-e^{-\eta})}{D_g^2 [1-e^{-\eta/2}]^2} \tag{34}$$

For clarity call $D = D_e$ where D_e is the effective uniformly illuminated diameter of a truncated gaussian beam, then

$$D_e = 2D_g \frac{[1-e^{-\eta/2}]}{\sqrt{1-e^{-\eta}}} \tag{35}$$

It is interesting to note from Eq. 35 that for no truncation

$$D_e = 2D_g \tag{36}$$

This observation provides the final key to our conversion problem of Fried's image resolution results to those of the on-axis transmitter irradiance (Eq. 22). Fried's data is normalized to a condition where r_o is held constant and D is varied. To normalize his evaluations to the opposite condition, that of holding D fixed and allowing r_o to vary, we multiply his R_∞/R_{max} by $a = (1/(D/r_o)^2)$. But from the above considerations we find that

$$\alpha = \frac{1.1}{D_g^2/\rho_o^2} \tag{36}$$

This conversion of Fried's data makes it indistinguishable from the evaluation of Eq. 22 as illustrated in Fig. 29.

Furthermore, Eq. 35 provides the proper expression necessary to bring the data of our truncated transmitter into agreement with the theoretical evaluations that were done specifically for the untrucated gaussian case.

To analyze the parametric advantage of tracking vs not tracking the short-term irradiance must be calculated for comparison against the long-term mean irradiance. Yura[107] attempts to apply the Fried recipe to the gaussian weighted aperture situation. It can be shown that Yura's result

$$\bar{I}_{ST} = \frac{k}{2\pi z}^2 \int d\vec{\rho}\; M_{ST}(\rho,z) e^{-\frac{ik}{z}\vec{p}\cdot\vec{\rho}} \int d\vec{r}\; U(\vec{r}+\vec{\rho}/2)\, U^*(\vec{r}-\vec{\rho}/2) e^{-\frac{ik}{z}\vec{\rho}\cdot\vec{r}} \tag{37}$$

where

$$M_{ST}(\rho,z) = e^{-(\rho/\rho_o)^{5/3}\left[1 - 0.62\delta(\rho/D)^{1/3}\right]}$$

will diverge for physically realizable conditions. This indicates a mistake in applying Fried's work. Fried's approximations for the short-term resolution appear to behave properly for uniform illumination[111], but cause trouble for the gaussian weighted case an exemplified by the preceding comments. A clue to the answer of this dilemna is given by Lutomirski[112] who suggests that the use of a short-term "MTF" is improper. After the

best-fit tilt portion of the aberration has been cancelled, the higher order distortions have modified characteristics. He then indicates that the proper method of solution is to retain these residual, higher order aberrations within the aperture integral of Eq. 37. The consequences have not yet been fully developed due to the increased mathematical complications.

Since there is remaining controversy over the short-term "MTF" we shall lean on the calculations of Heidbreder[113] and say that the gaussian weighted case cannot be too far from the uniformly weighted case. Hence the advantage of tracking vs not tracking for the mean irradiance is given by comparison of Eq.22 for the long-term average with Fried's approach to image resolution for the short-term average. The numerical details are illustrated by Fig. 30. Also, a numerical evaluation of Yura's expression, Eq. 31, is included for the short-term case when there is sufficient truncation of the integral to alleviate the divergence problem.

III.B.2. The Second Moment

Moving on to the exact equation for the second moment of the irradiance, we recall that Eq. 21 can be used to find the proper form. Among others,[28,86,114,115], Yura [34] provides the complete expression

$$\langle I \rangle^2 = \int d\vec{r}_1 \int d\vec{r}_2 \int d\vec{r}_3 \int d\vec{r}_4 \; U_A(\vec{r}_1)\, U_A^*(\vec{r}_2)\, U_A(\vec{r}_3)\, U_A^*(\vec{r}_4) \times \left\{ \frac{\exp\left[S(\vec{r}_1,\vec{p}_1) - S(\vec{r}_2,\vec{p}_2)\right]}{S(r_1,p_1)S(r_2,p_2)} \right\} \times \left\{ \frac{\exp\left[S(\vec{r}_3,\vec{p}_3) - S(\vec{r}_4,\vec{p}_4)\right]}{S(r_3,p_3)S(r_4,p_4)} \right\} \times H(\vec{r}_1,\vec{r}_2,\vec{r}_3,\vec{r}_4;\; \vec{p}_1,\vec{p}_2,\vec{p}_3,\vec{p}_4) \tag{38}$$

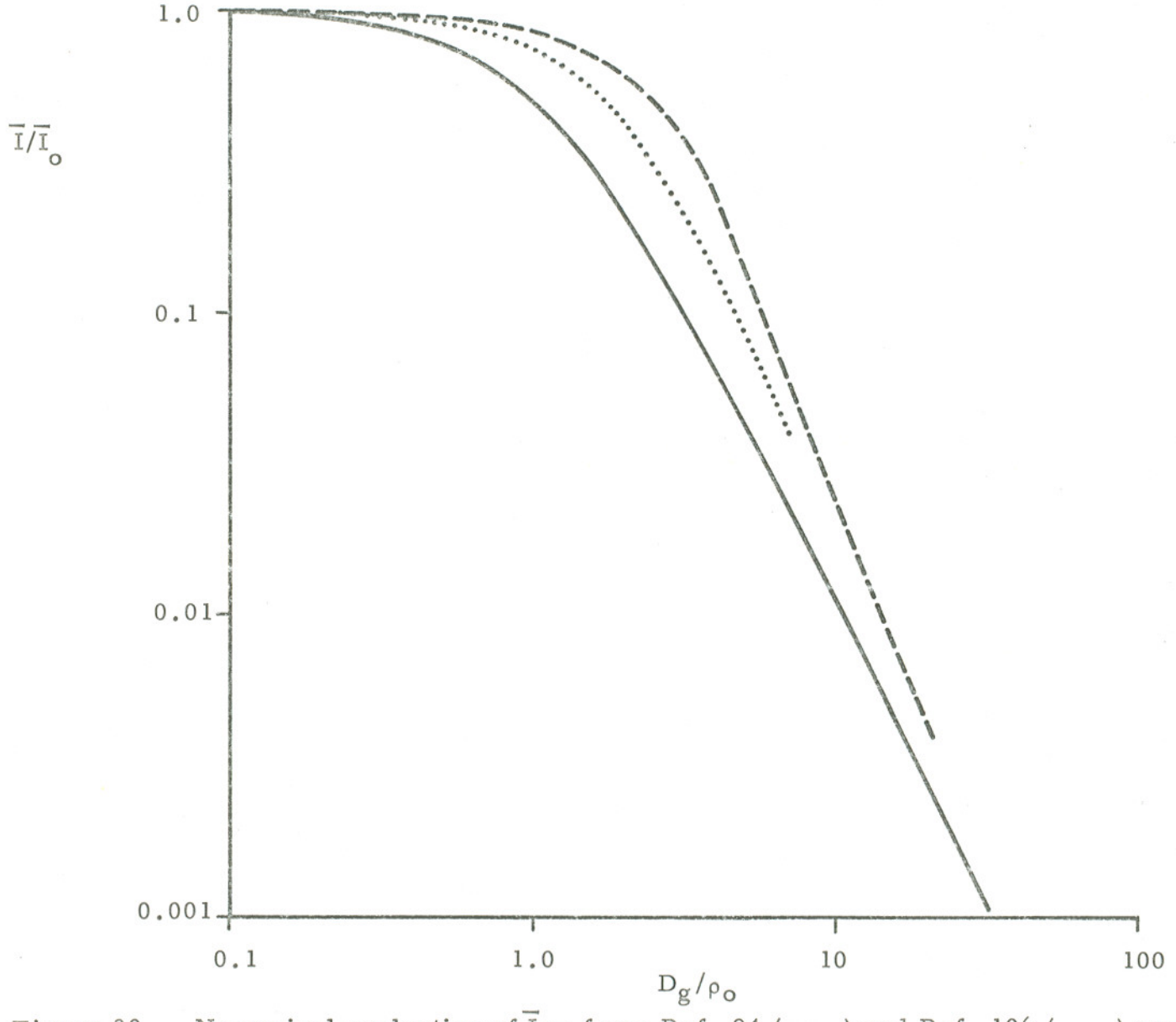

Figure 30. Numerical evaluation of $\bar{I}_{ST}$ from Ref. 94 (----) and Ref. 106 (....) compared to numerical results of Eq. 22 (———) for $\bar{I}_{LT}$.

where he defines

U_A = aperture illumination function

$$H(\vec{r}_1 \ldots \vec{r}_4; \vec{p}_1 \ldots \vec{p}_4) = \langle \exp[\psi(\vec{r}_1, \vec{p}_1) + \psi^*(\vec{r}_2, \vec{p}_2) + \psi(\vec{r}_3, \vec{p}_3) + \psi^*(\vec{r}_4, \vec{p}_4)] \rangle$$

$\psi(\vec{r}_i, \vec{p}_i)$ = complex perturbation of the spherical wavefront by the atmosphere

The difficulty of solving this problem is apparent in realizing that Eq. 38 represents an eight-fold integral. Some initial progress was made by Fried[116], however it was not until the paper by Banakh, et al.[117] that really useful, detailed results were available. Their numerical work agrees well with the predictions of the semiquantitative method (Fig. 28), even though Banakh and his co-workers generated faulty results. The error arises when they apply the normalizer for the tracked case to the equivalent of our non-tracked situation.

In conclusion, the advantages of cancelling wander have been presented in detail. Assymptotic predictions of the new unified, semiquantitative theory were compared with the exact, extended Huygens-Fresnel expressions. Good agreement was found. The fundamental applicability of these two approaches to beam wave propagation through turbulence can be proved only under rigorous experimental test. The following section provides a summary of this investigation.

III.C. EXPERIMENTAL RESULTS

INTRODUCTION

Atmospherically induced beam wander was cancelled through the use of a fast-tracking laser transmitter. The design philosophy, in addition to optical and electronic details, of the adaptive, fast-tracking transmitter is described in Appendix I. Fig. 31 provides a schematic diagram of the experimental arrangement. In that figure a beacon (point source) illuminates the adaptive transmitter with a constantly changing angle of arrival as perturbed by the atmosphere. The tracking transmitter detects the angle of arrival of the beacon wavefronts and launches a transmitted wavefront at that same angle. By reciprocity the focused spot of this transmitted beam should illuminate the target plane with its centroid locked onto the beacon. Note that signals from the tracker give fundamental data about beam wander while the point detector that is optically conjugate to the beacon provides fundamental data about short-term and long-term spread and the reduction in fluctuations due to tracking-out wander.

To test the theoretical advantages suggested by the last section, we collected the data listed in Table XI on magnetic tape via an FM tape-recorder. These signals were later analyzed by a PDP-11 computer and were subject to the parameters listed in Table XII. Special care was taken to insure a very homogeneous propagation range. This is important to the calculation of ρ_o from a single point measurement of C_n^2.

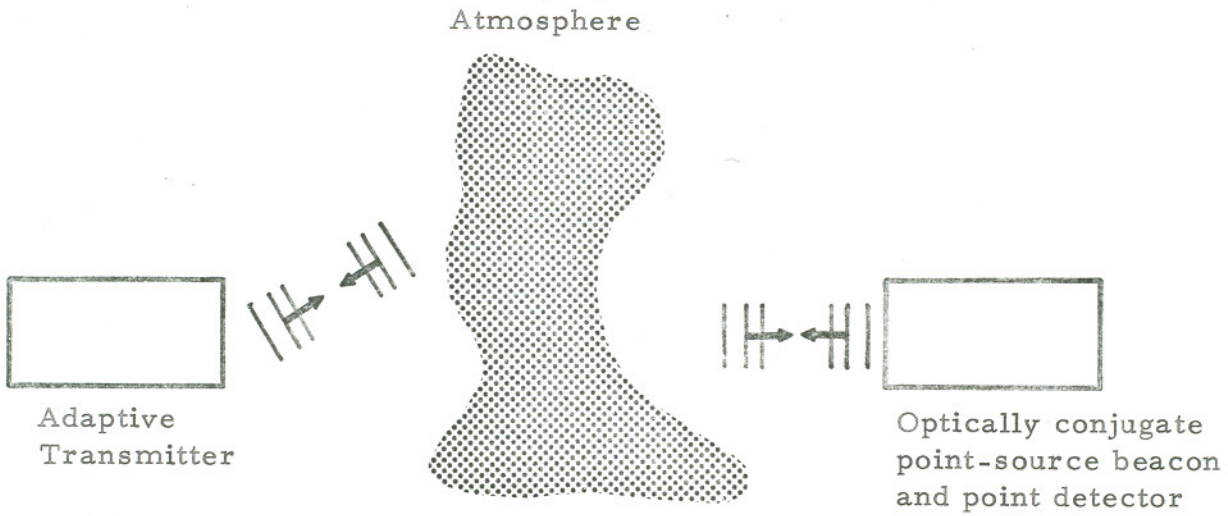

Figure 31. Basic experimental configuration

Table XI. Experimental Data

Tracker:	Wander signals
Target:	Linear irradiance
	Mean linear irradiance
	Log irradiance
	C_n^2
	Temperature fluctuations
	Wind speed and direction
	Mean temperature
	Barometric pressure

Table XII. Experimental Parameters

Wavelength: 6328Å
Path: 1.6 km, very homogeneous farm land
Beam height: 1.8 m
Mean irradiance: 120 s averaging
Variance { linear irradiance: 120 s averaging; log amplitude; wander angle
Spectra: Digital; 0.1 Hz resolution; 100 s averaging
Analogue; 1.0 Hz resolution; 100 s averaging
Probability distributions: Digital
Digital sampling rate: 1 kHz
Target receiver aperture: 0.6 cm
Target receiver bandwidth: 1 kHz
Target receiver dynamic range: ~ 80 db
Adaptive transmitter aperture: 15.2 cm
Adaptive transmitter focus resolution: 2.5 μm
Steering servo resonant frequency: 300 Hz, no load
Steering servo linearity: 1% of peak to peak deflection or better
Steering servo repeatability: 0.050% of peak to peak deflection or better
Open loop transfer function: Single integration
Closed loop bandwidth: ~ 20 Hz
Noise limited tracking angle: < 2% of transmitter diffraction-limited width
Microthermal probe response: 1 kHz
Microthermal probe separation: 10 cm, horizontal
Microthermal probe height: 1.8 m
Microthermal probe averaging time: 300 s

The entire set of data can be categorized into two cases: (1) target plane analysis, which allows a comprehensive study of the transmitter's irradiance distribution, and (2) transmitter plane analysis, which provides information regarding the fundamental nature of the wander phenomenon, per se.

III.C.1. Target Plane Analysis

III.C.1.a. Mean Irradiance

Wander cancellation increases the mean irradiance delivered to the target detector. Fig. 32 provides an example of the relative (smoothed) on-axis irradiance vs. time during weak turbulence conditions for the tracked and the non-tracked cases, indicating this very significant increase in the delivered mean irradiance. On the other hand, higher turbulence conditions allowed a decreased, but still substantial, advantage as seen in Fig. 33. Evident in the tracked case of both Figs. 32 and 33 is some residual fluctuation in the mean irradiance. This may be due to statistical fluctuations in ρ_o. The problem is not fully characterized yet, and the only related theoretical work considers night-to-night statistics over a horizontal path.[118,119]

Signals similar to those discussed in the previous paragraph were averaged for 120 seconds to obtain their relative values as a function of C_n^2 and ρ_o (Table XIII). Fig. 34 summarizes the results as a function of D_g/ρ_o. The abscissa of the theoretical curves and the data points have been brought into agreement by utilizing Eq. 29. The ordinate has been adjusted for fit due to the fact that low enough turbulence levels (small D_g/ρ_o) for a reliable

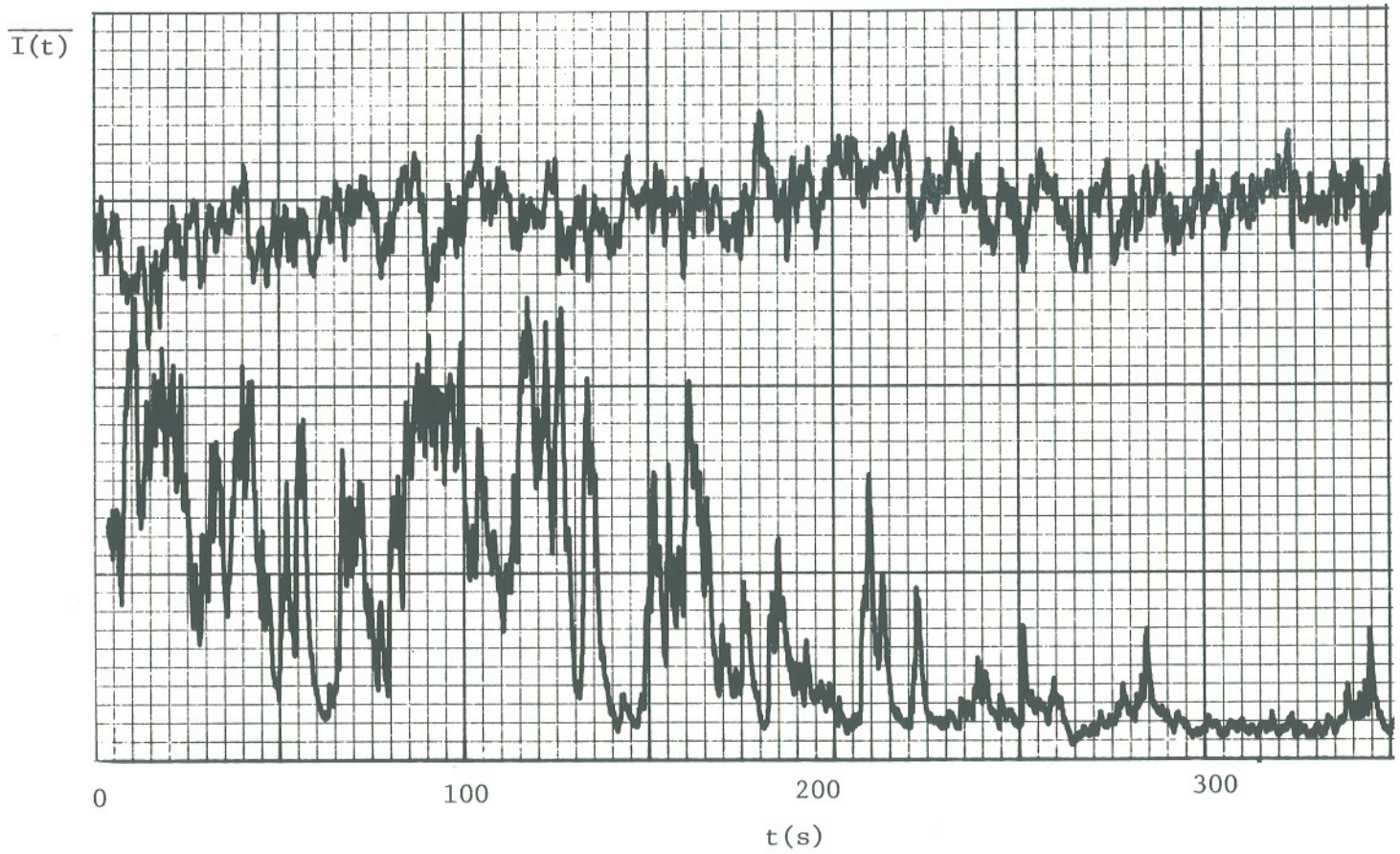

Figure 32. On-axis irradiance vs. time, with (upper trace) and without wander tracking (lower trace), for weak turbulence. The irradiance is smoothed with a 1-sec time constant.

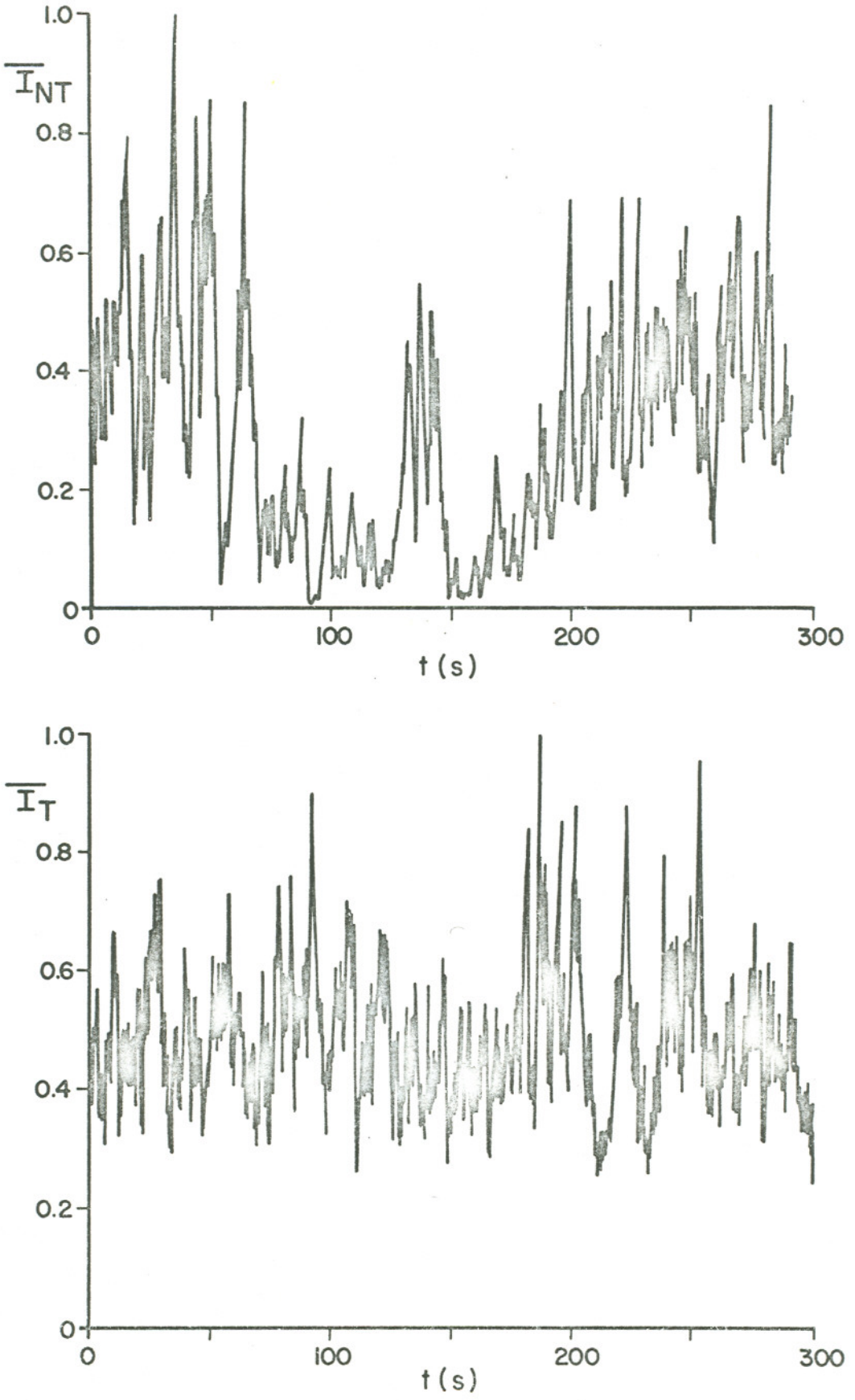

Figure 33. Smoothed (1-sec) irradiance vs. time, with (lower trace) and without (upper trace) wander tracking, for strong turbulence.

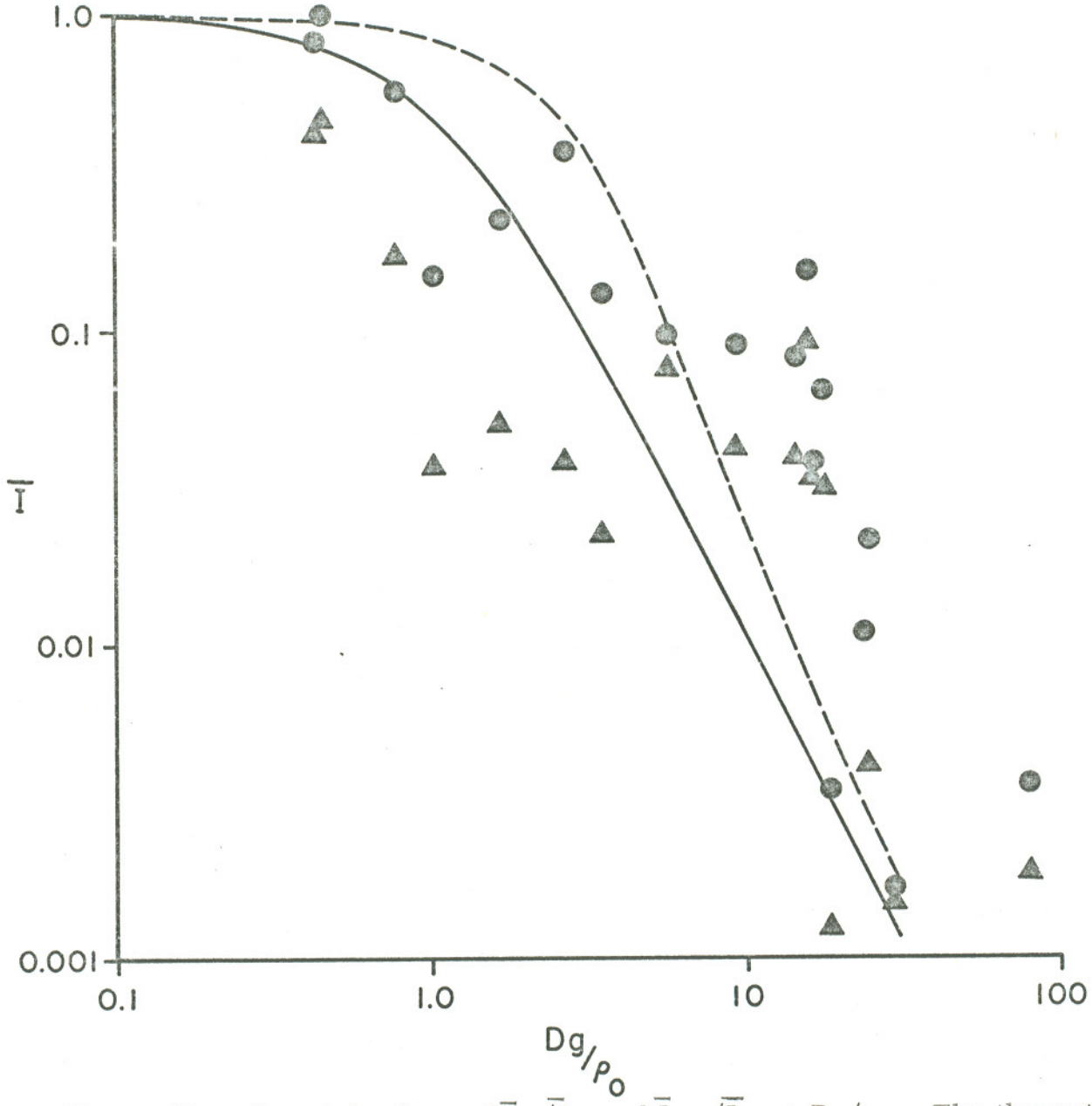

Figure 34. Experimental values of $\bar{I}_T/\bar{I}_o$ and $\bar{I}_{NT}/\bar{I}_o$ vs D_g/ρ_o. The theoretical curves are from Fig. 31.

Table XIII. Relative Mean Irradiance

Equation $\rho_o = [0.309\ L\ k^2 C_n^2\ \ell_o^{-1/3}]^{-1/2}$ was used to calculate ρ_o for data marked (*) because $\ell_o > \rho_o$. Equation $\rho_o = [1.44(k^2 L C_n^2)^{-3/5}]$ was used to calculate ρ_o for the unmarked data because $\rho_o > \ell_o$.

ρ_o(m)	Relative $\bar{I}_T$	Relative $\bar{I}_{NT}$	$\bar{I}_T/\bar{I}_{NT}$
8.81×10^{-4}(*)	0.00365	0.00187	1.95
2.40×10^{-3}(*)	0.00170	0.00151	1.13
2.90×10^{-3}(*)	0.0217	0.0110	1.97
3.00×10^{-3}(*)	0.0110	0.00416	2.64
3.8×10^{-3}(*)	0.00354	0.00126	2.81
4.0×10^{-3}	0.0646	0.0316	2.04
4.3×10^{-3}(*)	0.0485	0.0343	1.41
4.5×10^{-3}	0.154	0.0922	1.67
4.9×10^{-3}(*)	0.0830	0.0391	2.12
7.8×10^{-3}	0.0918	0.0428	2.14
1.3×10^{-2}(*)	0.0981	0.0750	1.31
2.0×10^{-2}	0.133	0.0225	5.91
4.2×10^{-2}	0.224	0.0507	4.42
6.9×10^{-2}	0.151	0.0372	4.06
9.2×10^{-2}	0.583	0.174	3.35
1.6×10^{-1}	1.00	0.464	2.16
1.7×10^{-1}	0.832	0.419	1.99

measurement of the on-axis mean irradiance for the diffraction limited case could not be obtained for the 1.6 km path. Notably, the data of the tracked case nearly met this criterion.

At high turbulence (large D_g/ρ_o) both the track and the nontracked on-axis mean irradiances fall off as ρ_o^{-2}. In the non-tracked case for D_g/ρ_o greater than 9.6 this occurred with a correlation coefficient of 0.59, while the tracked case occurred with a correlation coefficient of 0.68 (D_g/ρ_o greater than 9.6). Presumably data for higher turbulence will indicate a closer approach to the ρ_o^{-2} fall off and somewhat better correlation coefficients. The importance of this result is the realization that for strong turbulence conditions, beamspread is indicative of a transmitter diameter ρ_o rather than the true telescope diameter. The size of the beam is totally determined by the atmosphere. This fact explains the early beamspread results of Buck[120] and those of Khmelevtsov.[121]

The empirical expression for beamspread developed by Dowling and Livingston[100]

$$X = C_n^{0.85} Z^{0.62} k^{0.65} \tag{39}$$

was also tested in this high turbulence regime. For X greater than 10 there was virtually no correlation between X and the data. Livingston[122] indicates that this is reasonable since their expression was obtained for conditions of moderate turbulence, only.

Hence, we tested Eq. 39 for the transition region between the diffraction limited case and the ρ_o^{-2} fall off. For X less than 10 we corroborate the empirical relation (correlation coefficient of 0.89).

The parametric advantage of the tracked cases vs. the non-tracked case is better observed in Fig. 35 where the ratio $\bar{I}_T/\bar{I}_{NT}$ is plotted as a function of D_g/ρ_o. The theoretical curve is from the reciprocal case of Fried's work on the LT and ST average image resolution for a uniformly illuminated aperture.[94] Both data and theory indicate that a maximum advantage occurs at D_g/ρ_o of order unity. This is a very important result because the consequences of not adjusting the transmitter aperture to fit the turbulence conditions (as indicated by ρ_o) can defeat the entire advantage of tracking out the tilt variations.

In general more advantage was observed than predicted. This effect was also observed by Gilmartin and Holtz[123]. However, data spread and eventual completion of the theoretical expressions for the gaussian weighted case may prove this apparent extra advantage to be negligible. In conclusion it suffices to suggest that there is good parametric agreement between the theoretical predictions and data collected for the mean irradiance utilizing the fast-tracking transmitter. The next step is to investigate the effects of tracking on the fluctuations about these mean levels.

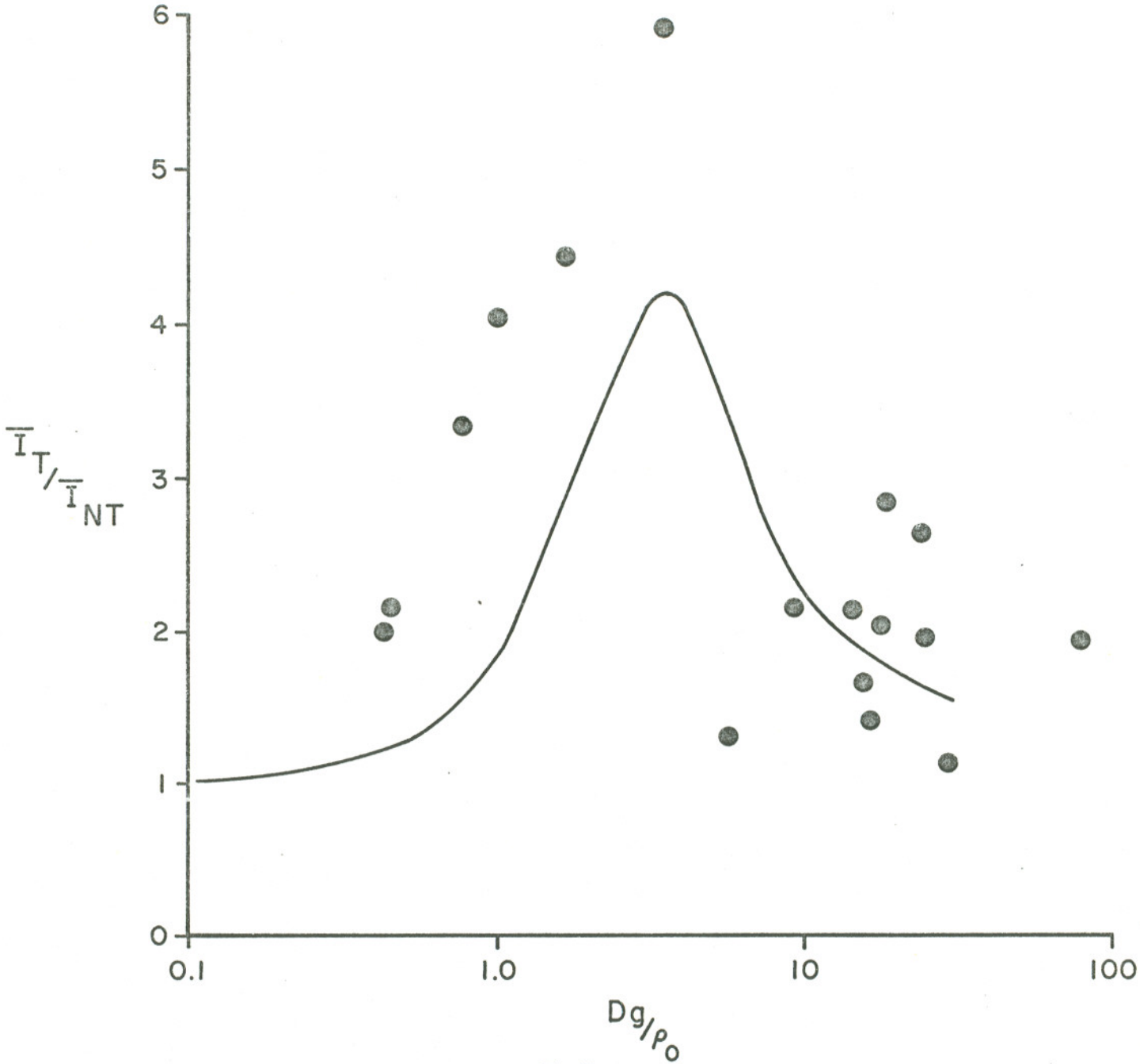

Figure 35. Experimental values of $\overline{I}_T/\overline{I}_{NT}$ vs. D_g/ρ_o. The theoretical curve is from Ref. 94.

III.C.1.b. Fading

The advantages of tracking in reducing fluctuations about the mean irradiance are appraised by measurements of the linear irradiance and log-amplitude variances, σ_I^2 and σ_χ^2, respectively. Both of these parameters were measured from probability distributions taken directly from the target point-detector signals with approximately 120 seconds of averaging. No statistical assumptions were made in order to derive one or the other.

Normalized Variance of the Linear Irradiance

Examples of the unsmoothed, relative-irradiance fluctuations vs. time are provided in Fig. 36 for weak turbulence. Initiation of tracking cancelled all of the very deep, slow fading due to wander, leaving residual scintillation on the interior part of the nearly diffraction limited spot. This effect could be visually observed and indicates that preliminary conclusions of Chapter II regarding Fig. 16 to be incomplete. Fig. 37 is a similar example except for stronger turbulence. Much higher frequency components existed due to the fact that the beam had broken up into an array of independently scintillating patches as shown in Fig. 18. Wander was still important, as was its cancellation.

A summary of the data on linear irradiance fading, Fig. 38, indicates that for the non-track case, σ_I^2 peaked at nearly the same D_g/ρ_o value as that for which tracking caused the maximum increase in mean irradiance.

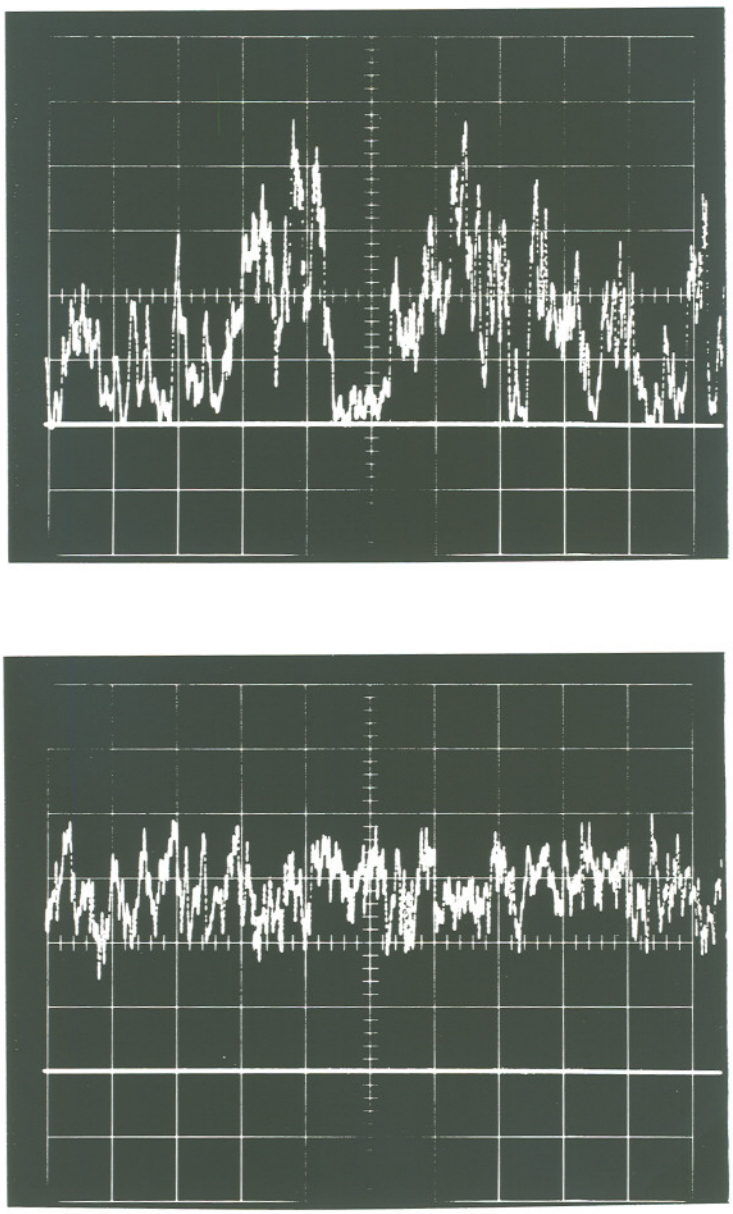

Figure 36. Unsmoothed irradiance vs. time, for the case of Fig. 32 (lower trace is tracked). The abscissa is 0.5 sec/div.

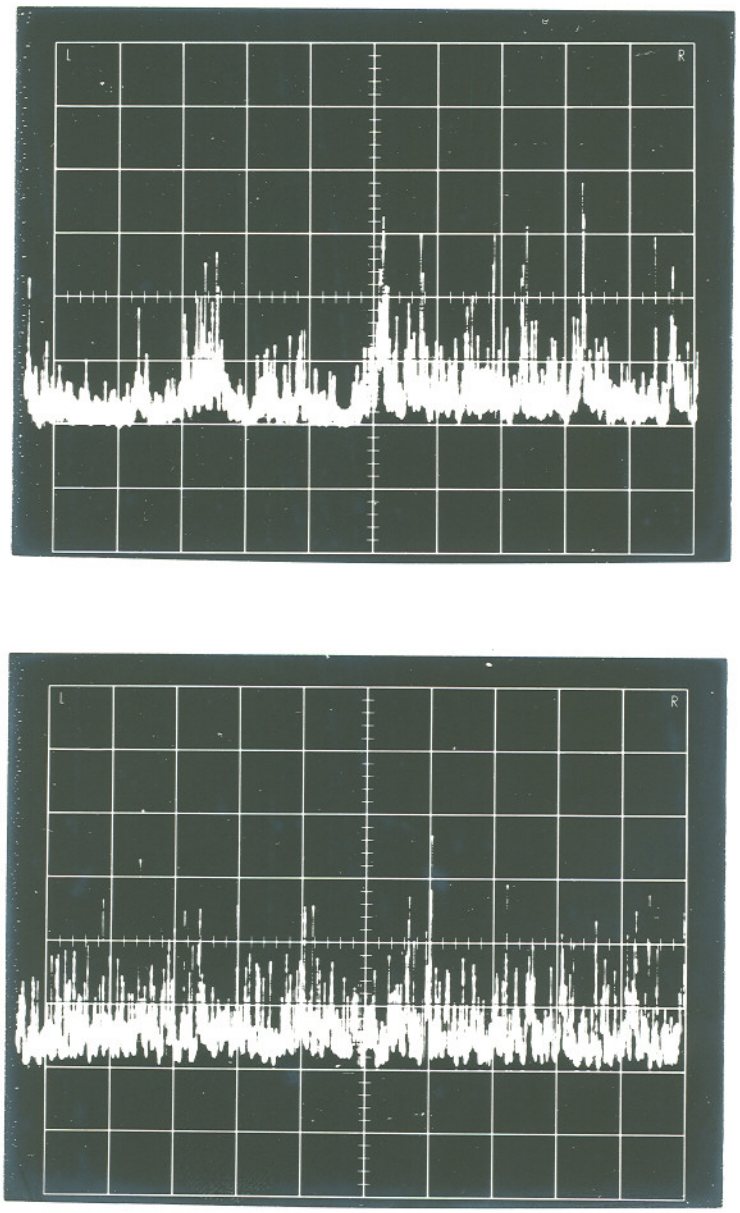

Figure 37. Unsmoothed irradiance vs. time, for the case of Fig. 33 (lower trace is tracked). The abscissa is 0.5 sec/div.

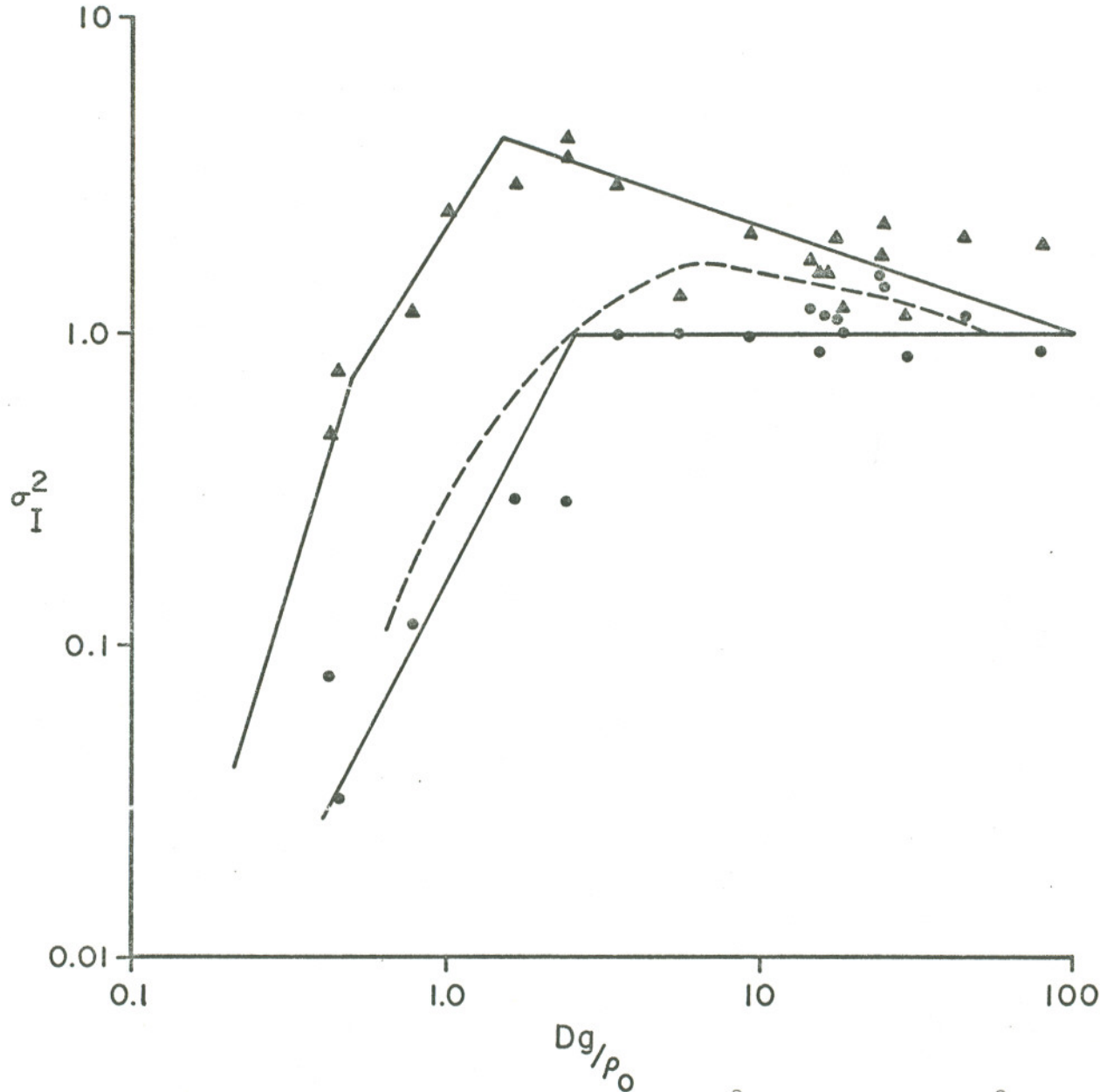

Figure 38. Normalized irradiance variance with $\sigma^2_{I_T}$ (●) and without $\sigma^2_{I_{NT}}$ (▲) tracking vs D_g/ρ_o. The theoretical curves are from Ref. 116 (-----) and Ref. 77 (———)

It is now recognized theoretically and experimentally that a D_g/ρ_o value of order unity signals the special combination of beam geometry-turbulence conditions generating maximum wander. As displayed by Fig. 39, the value of σ_I^2 for the tracked case indicates an order of magnitude reduction in fading compared with the non-tracked case in the critical D_g/ρ_o region.

For stronger turbulence, $\sigma_{I_{NT}}^2$ supersaturated from a value of about 1.3 to unity. At this point we have the indication that beam spread had increased sufficiently to fully dominate wander. The tracking advantage became unimportant. This is true because $\sigma_{I_T}^2$ saturated smoothly to unity at the critical D_g/ρ_o value, and remained saturated for higher turbulence levels. In contrast to this, tracking continued to provide order-of-magnitude reductions in the measured variance at small D_g/ρ_o values. In fact, if the two branches of the tracked and non-tracked variances do not meet at very small D_g/ρ_o, then there is possible indication that more energy exists in the low wavenumber region of the turbulent spectrum than is acknowledged by theory. This problem emphasizes the importance of work such as that of Greenwood and Tarazano.[124]

The saturation effects observed in Fig. 38 support optical heterodyne receiver analysis by Fried,[114] as well as fourth moment calculations by Brown.[29] This last fact can be substantiated by realizing that tracking cancels the effect of turbulence wavenumbers lower than the inverse of

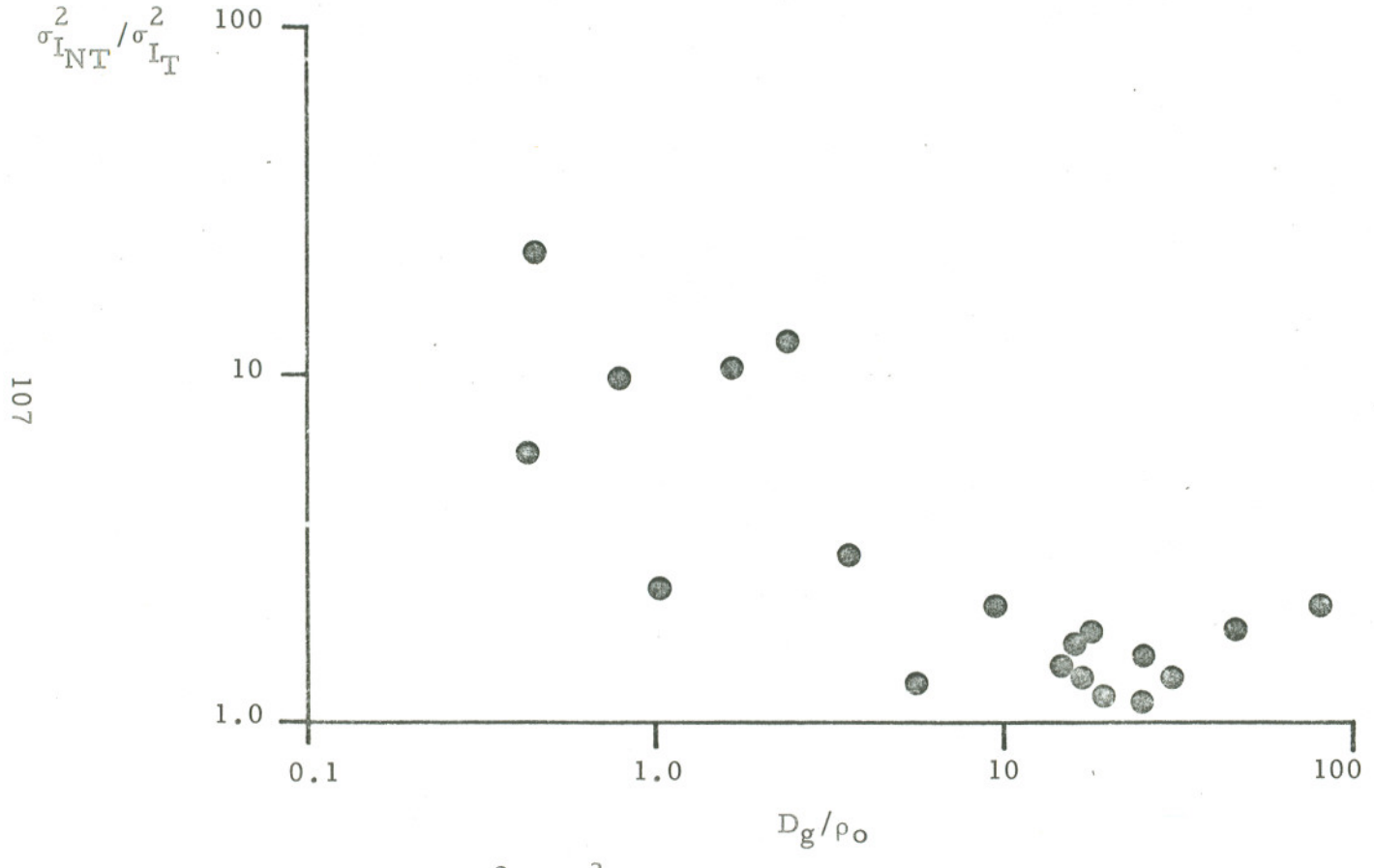

Figure 39. Values of $\sigma^2_{I_{NT}}/\sigma^2_{I_T}$ vs. D_g/ρ_o corresponding to Fig. 38.

the telescope diameter. The net result is to produce an enhanced outer scale effect. The consequence of the enhanced outer scale is to force a smooth saturation to unity, rather than a humped curve exhibiting super-saturation. This type of detail is given by Brown's calculations for considerations at 10.6 μm where natural outer scale effects can become important.

Furthermore, the slopes indicated on Fig. 38 were derived from the unified phenomenological approach to beam wave propagation, thus supporting its conclusions. Also plotted is an evaluation of the second moment via Huygens-Fresnel techniques that shows good parametric agreement. The fit is a little low, however, due to the improper normalization to the equivalent of our tracking condition by Banakh, et al.[117]

Log-Amplitude Variance

When the fluctuations were processed directly in terms of the log-amplitude, signals similar to those of Figs. 40 (weak turbulence) and 41 (strong turbulence) are observed. Again, it is seen that tracking cancels the low frequency fluctuations only, leaving residual higher frequency components. Data for a wide range of turbulence levels are presented in Fig. 42. Two important points become apparent: (1) for the non-track case, σ_{χ}^2 remained saturated at the same approximate value for both strong turbulence (beam breakup dominated conditions) and weak turbulence (wander dominated conditions) and (2) for the tracking case, finite-transmitter smoothing effects were not significantly observed.

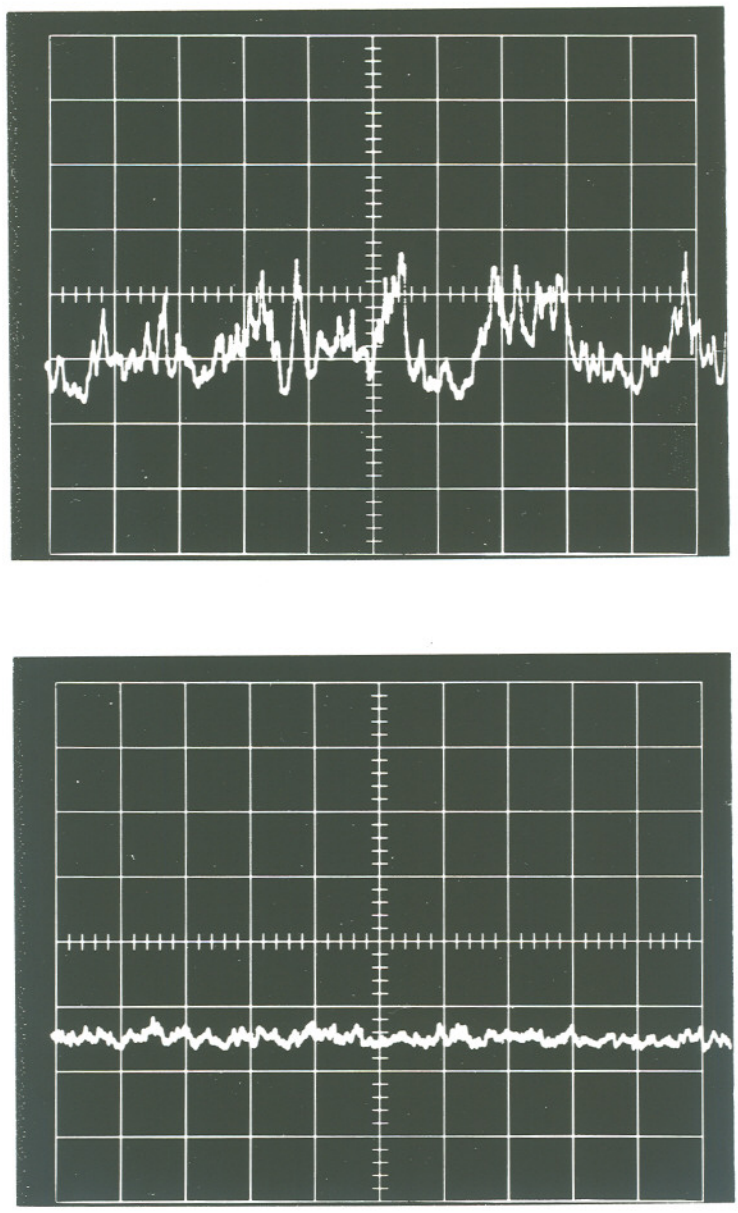

Fig. 40. Log-irradiance vs. time, for the case of Fig. 32 (lower trace is tracked).

Ordinate:	One decade/div.
Abscissa:	0.5 sec/div.

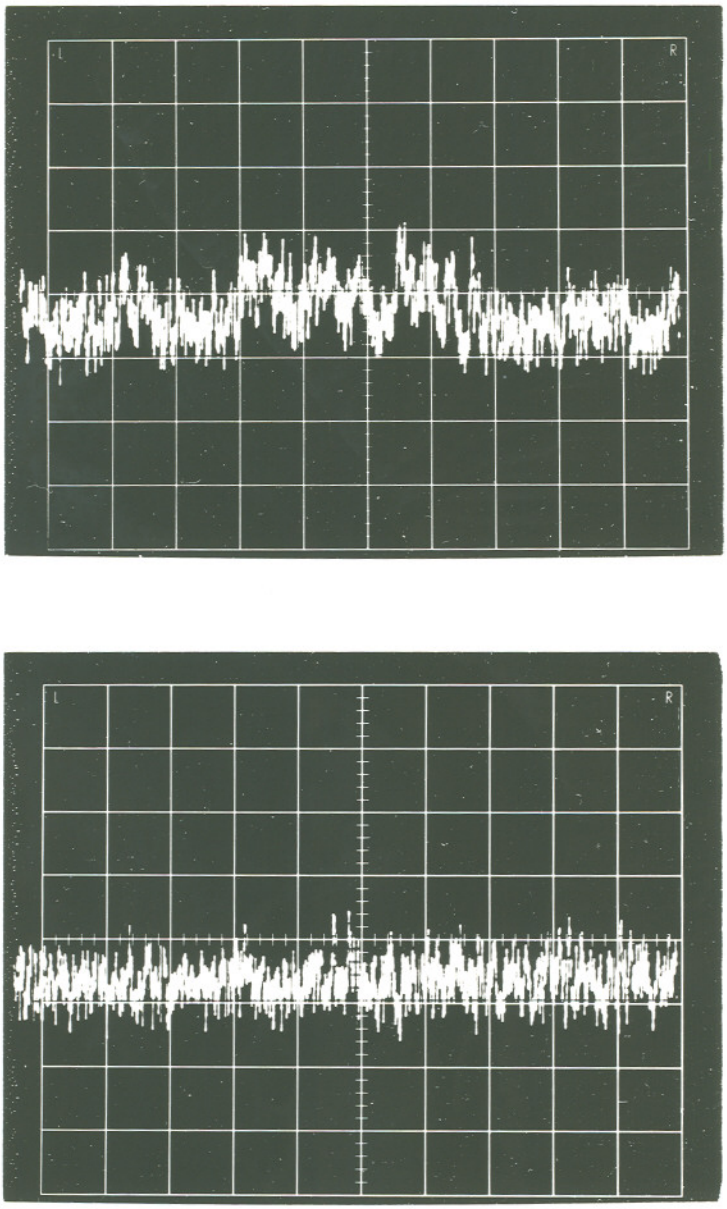

Figure 41. Log-irradiance vs. time, for the case of Fig. 33 (lower trace is tracked).

Ordinate:	one decade/div.
Abscissa:	0.5 sec/div.

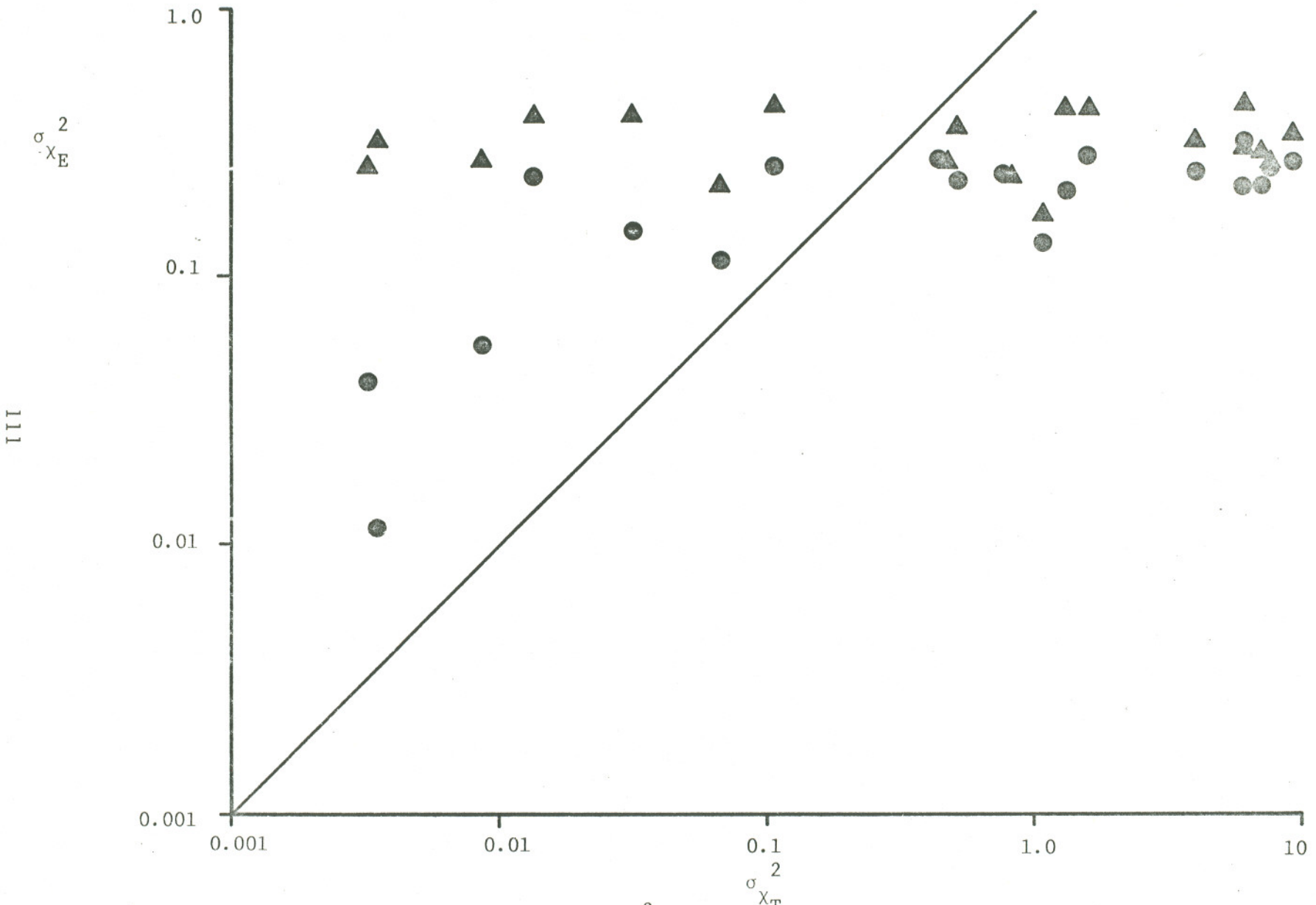

Figure 42. Experimental log-amplitude variance ($\sigma^2_{\chi_E}$) vs. theoretical Rytov value for a point source ($\sigma^2_{\chi_T}$), with (●) and without (▲) wander-tracking. (———) indicates $\sigma^2_{\chi_E} = \sigma^2_{\chi_T}$ condition.

To further test the conclusion of point number two, above, the 1.6 km path was shortened to 91 m. This was done to obtain more consistently small D_g/ρ_o values. With a transmitter Fresnel number identical to that of the 1.6 km path arrangement, we utilized the tracking system to probe the resonance-like effects of focussing as seen in Fig. 2 of Ref. 68. Fig. 43 furnishes the result. Notably, the enhanced scintillation due to slight defocussing was exhibited, as was the approach to point source statistics for gross defocussing. However, contrary to the theoretical predictions, the finite source scintillations did not go to near zero at precise focus. With regard to these data, the implicit conclusion is that for homogeneous turbulence over reasonable paths and with reasonable apertures the applications of first-order scintillation theory to the beam wave propagation problem are not valid. Ref. 121 also supports this result, and the implications on practical design considerations are obvious.[125]

Probability Distributions

Analysis of the log-amplitude signals was continued by consideration of their cumulative probability distributions. Fig. 44 suggests that during strong turbulence, tracking not only reduced the slope of the distribution (decreased the variance) but also tended to increase its log-normality. For weak turbulence data, however, the distribution remained somewhat distorted even during the tracking state (Fig. 45). In this state the dynamic range of the photocurrent was significantly less than one decade. It is

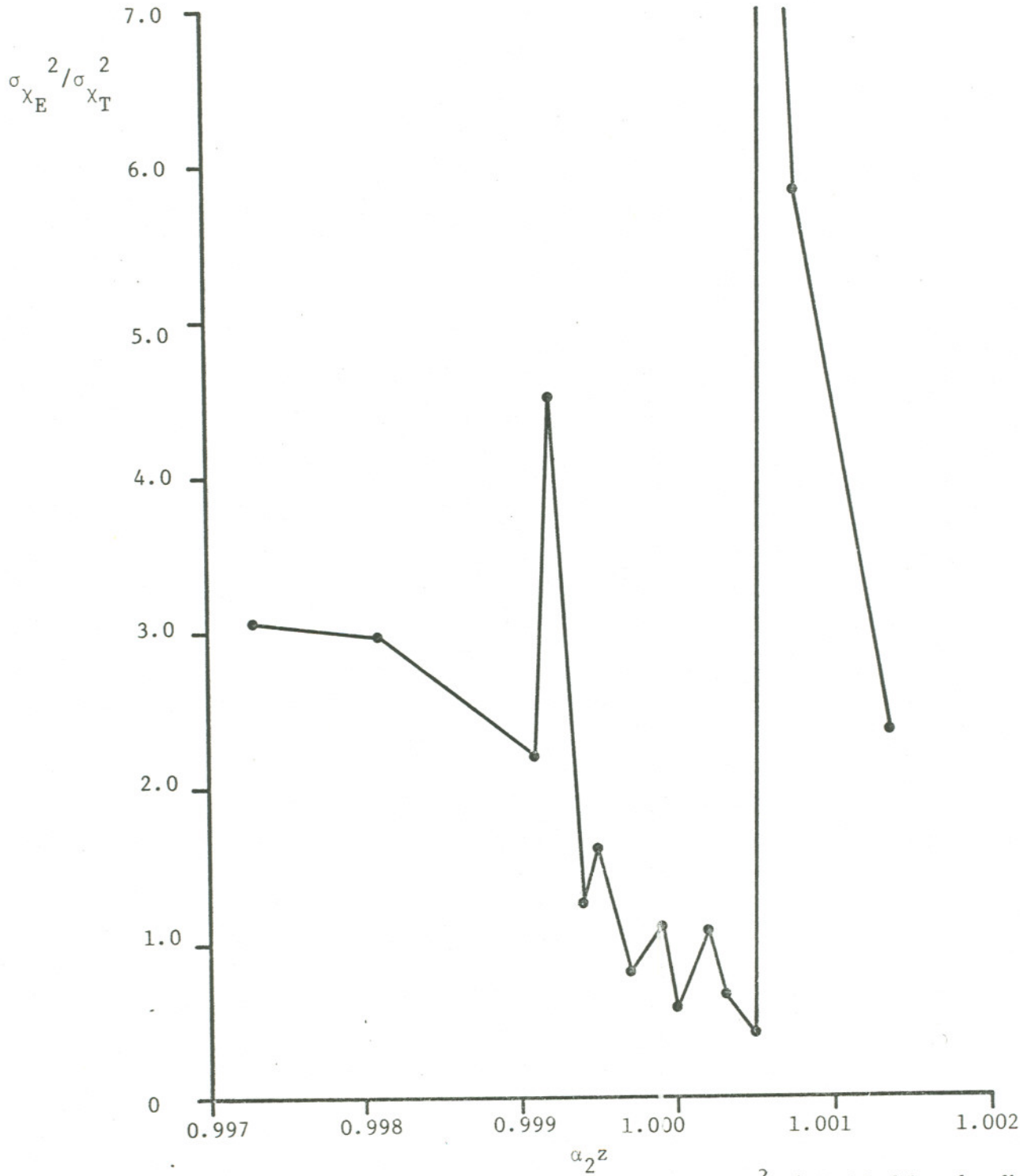

Figure 43. Experimental log-amplitude variances ($\sigma_{\chi_E}^2$) divided by the first-order theoretical values for a point source ($\sigma_{\chi_T}^2$) vs focus condition $\alpha_2 z$. The value of D/ρ_o is 0.80.

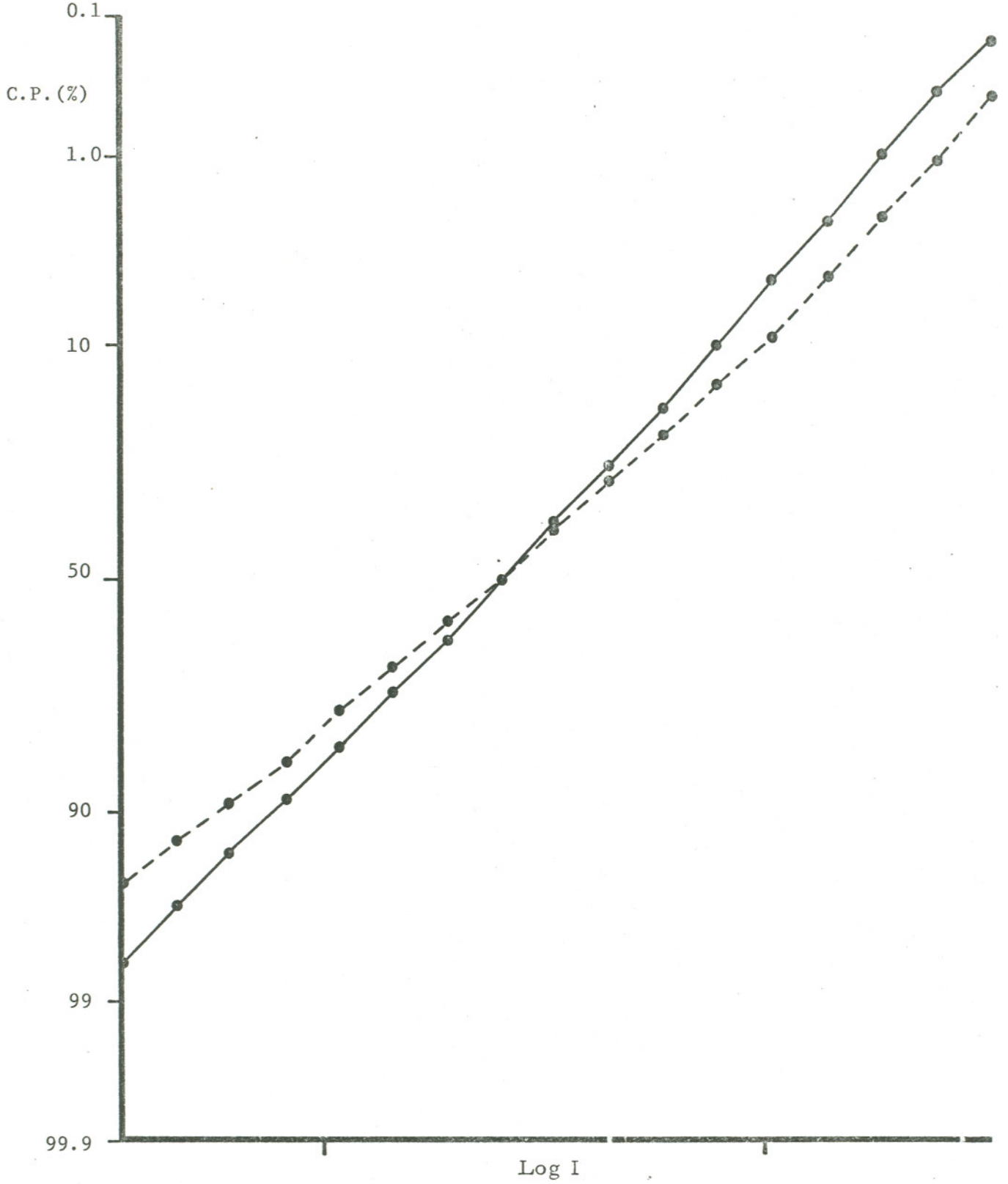

Figure 44 Cumulative probability (C.P.) for the log irradiance in strong turbulence, for the wander-tracked (———) and non-tracked (-----) cases. Scale marks on the abscissa indicate one decade of photocurrent.

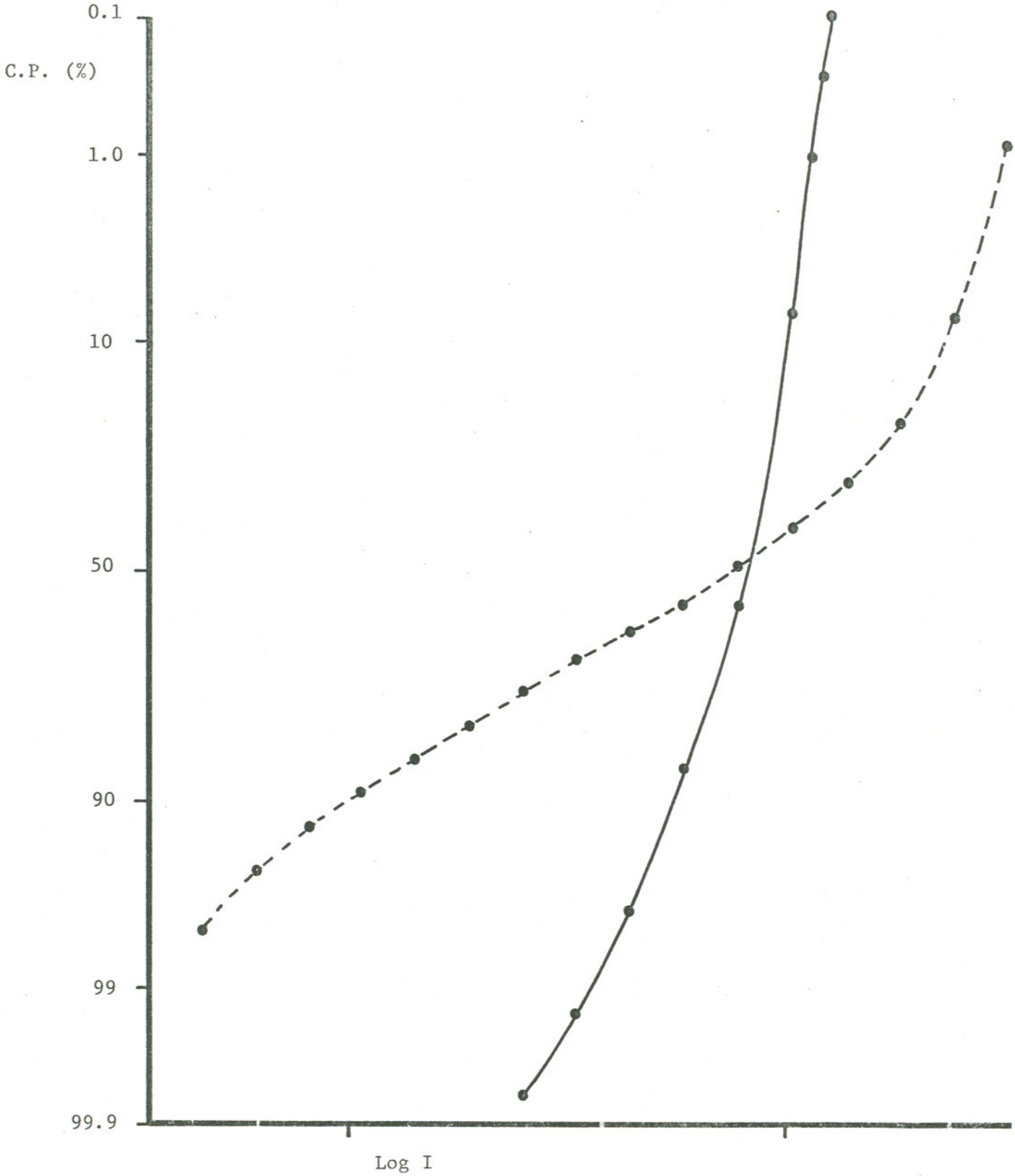

Figure 45. Cumulative probability (C.P.) for the log irradiance in weak turbulence, for the wander-tracked (———) and non-tracked (-----) cases. Scale marks on the abscissa indicate one decade of photocurrent.

interesting to note that the non-tracked data of Fig. 45 provided a distribution similar to that of a normally distributed variable modulated by a square wave.[126] The dynamic range of the signal fluctuations induced by wander was observed to be nearly that of the high turbulence distributions.

Spectra

In addition, low (Fig. 46) and high (Fig. 47) turbulence examples of the temporal frequency content of the log-amplitude signals were investigated. These first two spectral illustrations are presented on a relative scale. It is apparent that during high turbulence, tracking primarily affected the components below 20 Hz (wander components) while significant scintillation (beam breakup components) remained uneffected above 20 Hz. In contrast, the low turbulence spectrum for the non-tracked case shows nearly all frequency components existing below 20 Hz. This indicates a wander predominant condition, and as such, all components were reduced quite dramatically by tracking. The spectra normalized by the log-amplitude variance and corresponding to Figs. 46 and 47 are shown in Figs. 48 and 49.

One of the more striking effects observed was the broadening of the spectra as the beam breaks up into the independently scintillating patches. This effect is emphasized when the spectra are weighted by the frequency. Figs. 50 and 51 illustrate this effect for frequency weighted counterparts of Figs. 46 and 47.

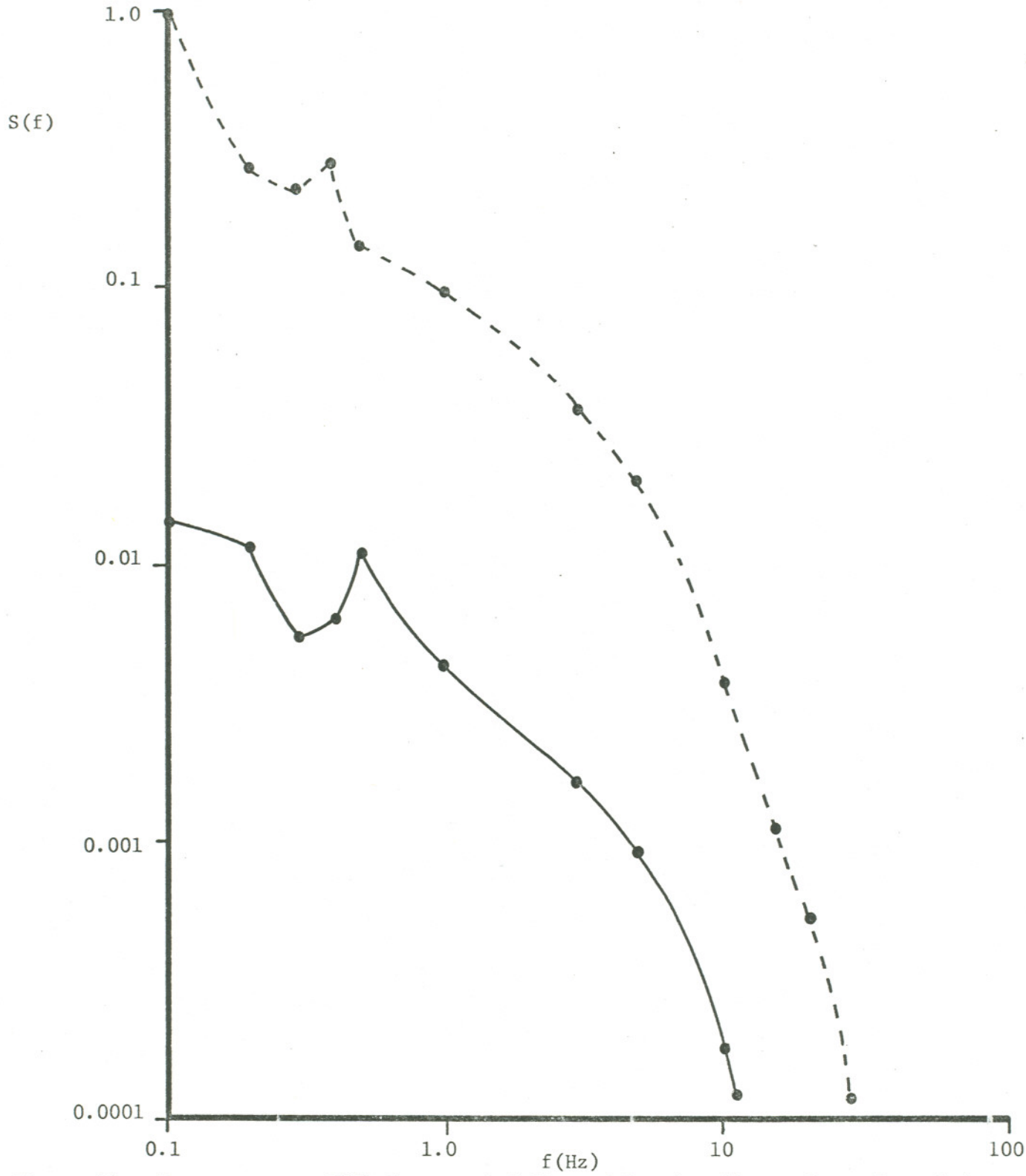

Figure 46. Power spectra S(f) for total fading of log irradiance in weak turbulence ($D/\rho_o = 0.97$), for the wander-tracked (———) and non-tracked (-----) cases.

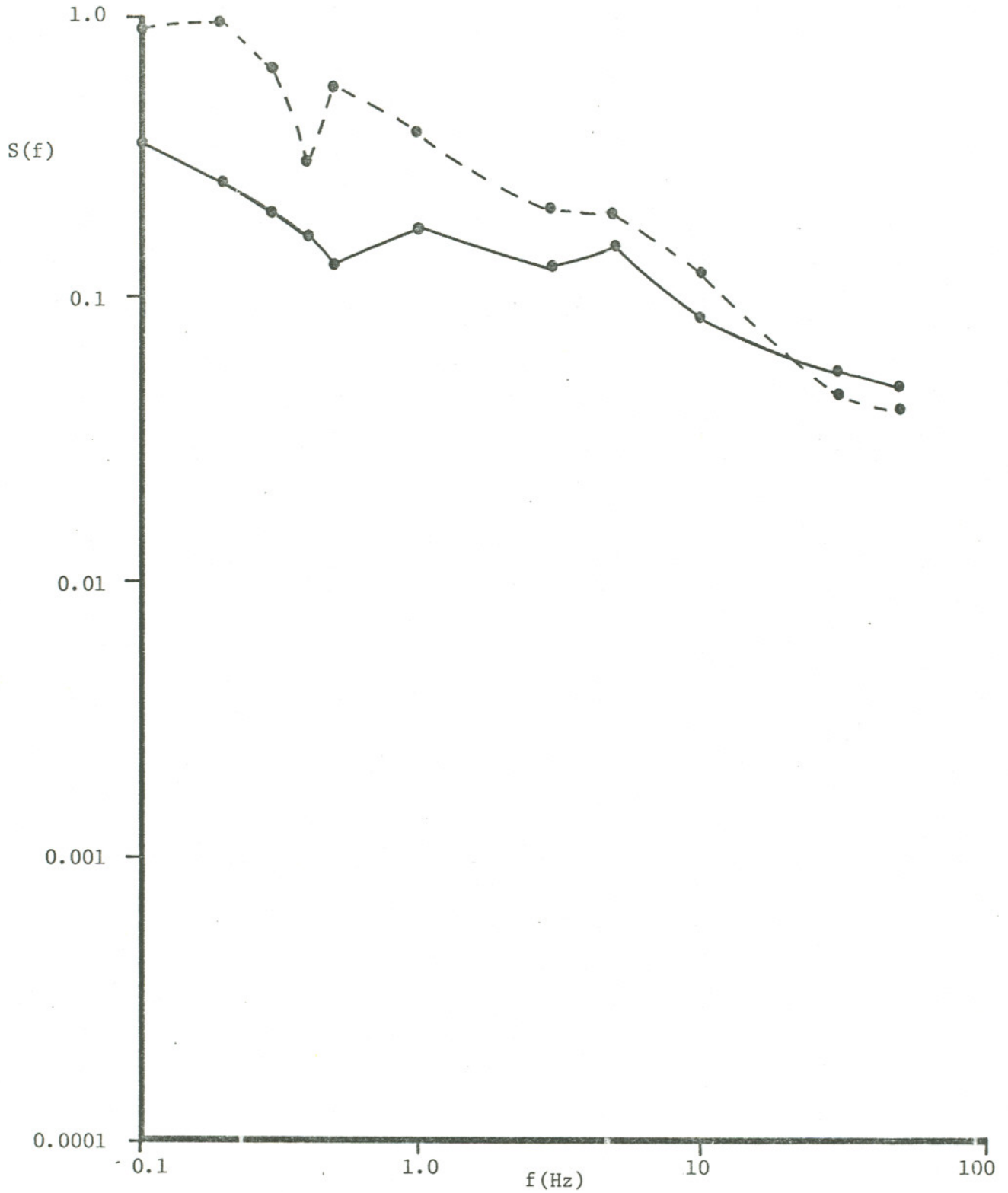

Figure 47. Power spectra as in Fig. 46, for $D/\rho_o = 63$.

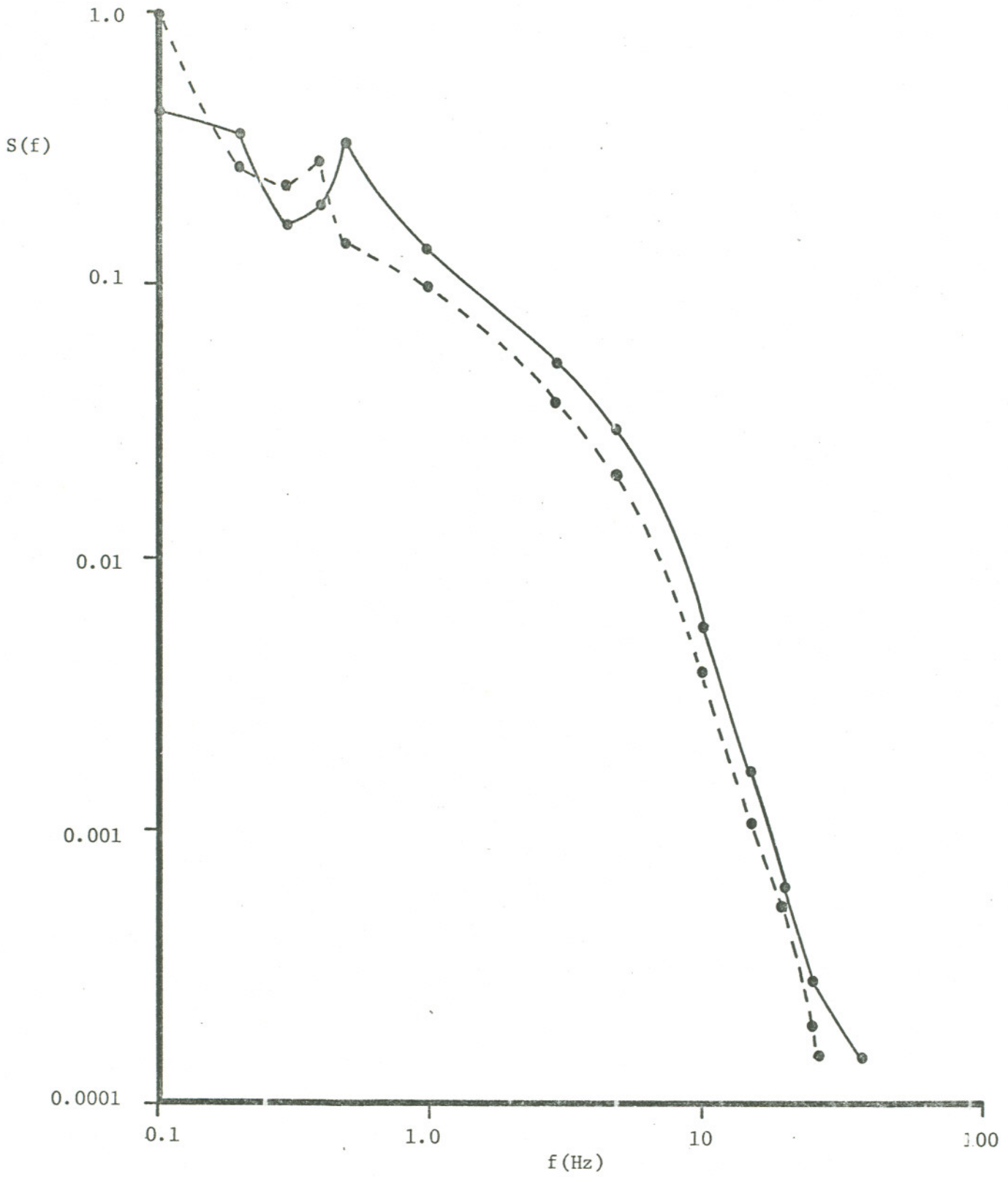

Figure 48 . Curves of Fig. 46 , normalized by total log amplitude variance for each case.

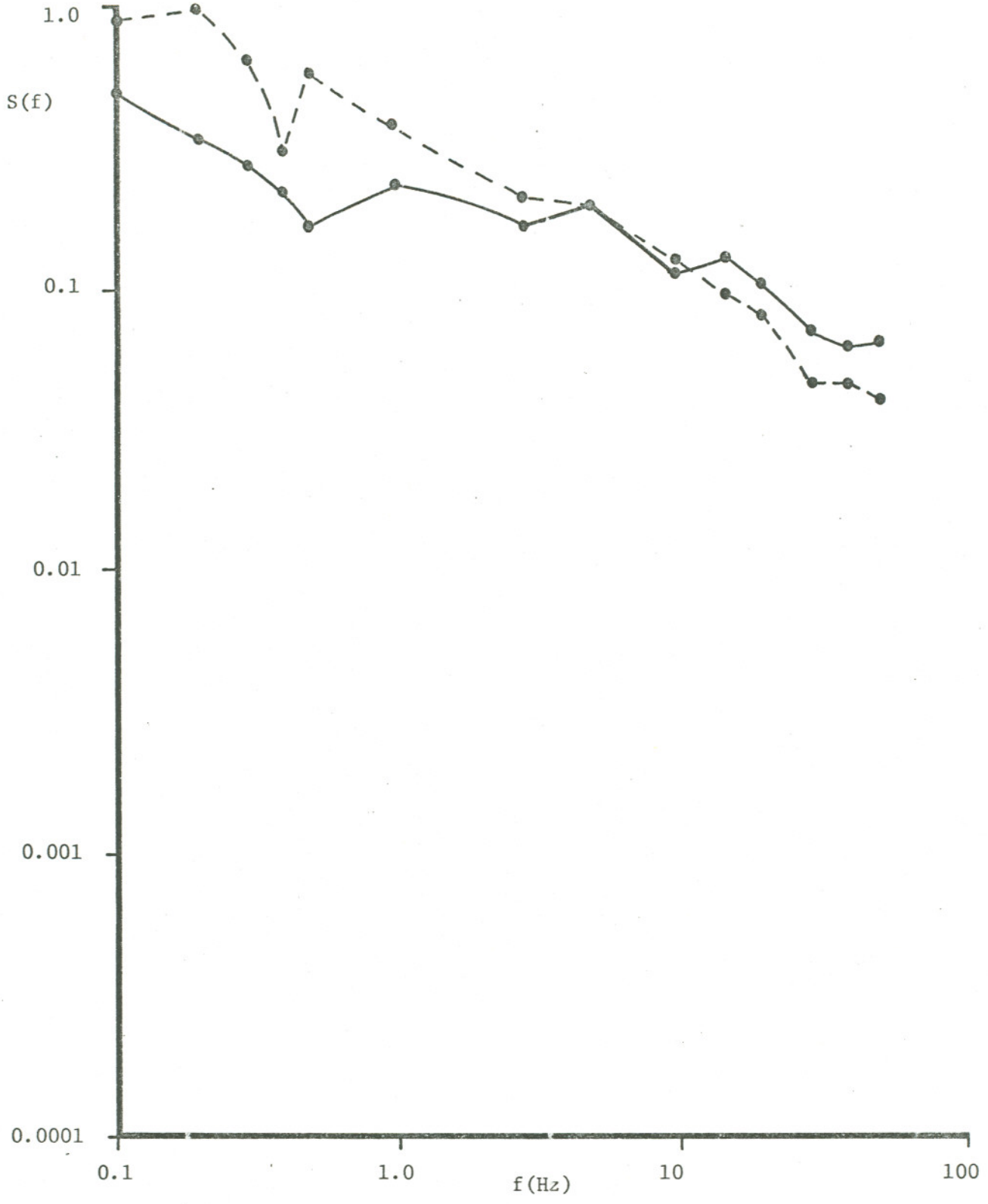

Figure 49 . Curves of Fig. 47, normalized by total log amplitude variance for each case.

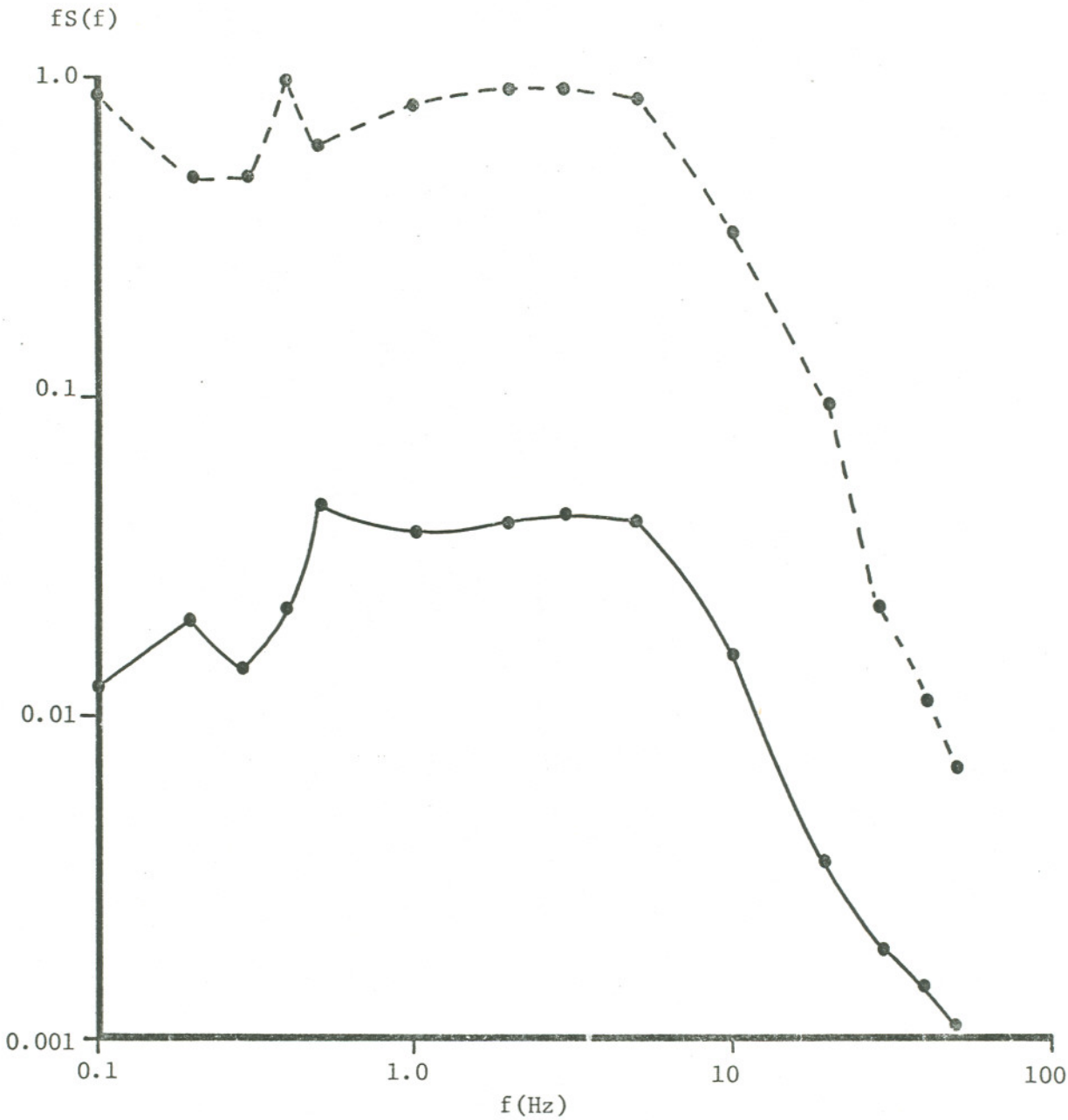

Figure 50. Curves of Fig. 46, weighted by frequency.

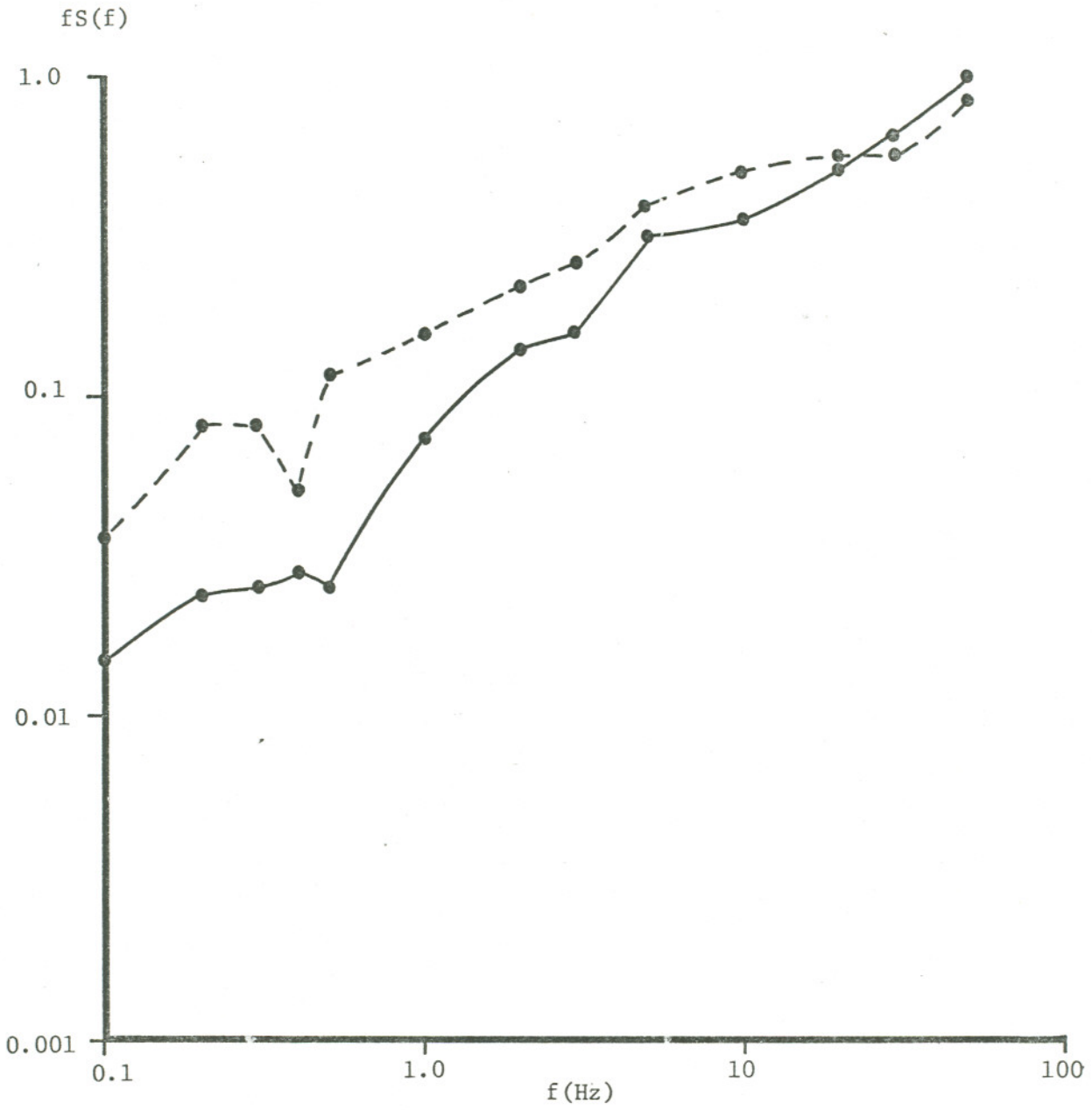

Figure 51. Curves of Fig. 47, weighted by frequency.

Also evidenced in the previous examples is the cancellation of definite peaks in the spectra below one Hz after tracking has been initiated. This corresponds to cancellation of specific peaks in the wander spectrum. An exaggerated example of this effect is furnished by the frequency weighted spectrum of Fig. 52. In this particular situation there were two well defined spectral regions – a wander portion and a scintillation portion. The wander related components were very effectively cancelled by tracking.

III.C.2. Transmitter Plane Analysis

III.C.2.a. Wander Angle

In addition to target signals, the error voltages driving the tracking transmitter steering mirrors were recorded. These transmitter signals provided quantitative data on beam wander to augment the comprehensive study of beam wave propagation. Specifically, the error voltage is a measure of the effective angle of arrival fluctuations of the point-source beacon wavefronts. But by reciprocity they also relate directly to the transmitter beam displacements that would be experienced in the target plane during the non-tracked condition. For instance, the theoretically predicted rms wander of the untracked transmitter beam is approximately given by[10]

$$\Phi_T \simeq \left(\frac{D_s(b)}{b^2} \right)^{1/2} \tag{40}$$

where $D_s(b)$ is the wave-structure function and b is the telescope diameter. For a specific condition observed (measured $\ell_o \simeq 0$ and $C_n^2 = 5.14 \times 10^{-14} m^{-2/3}$)

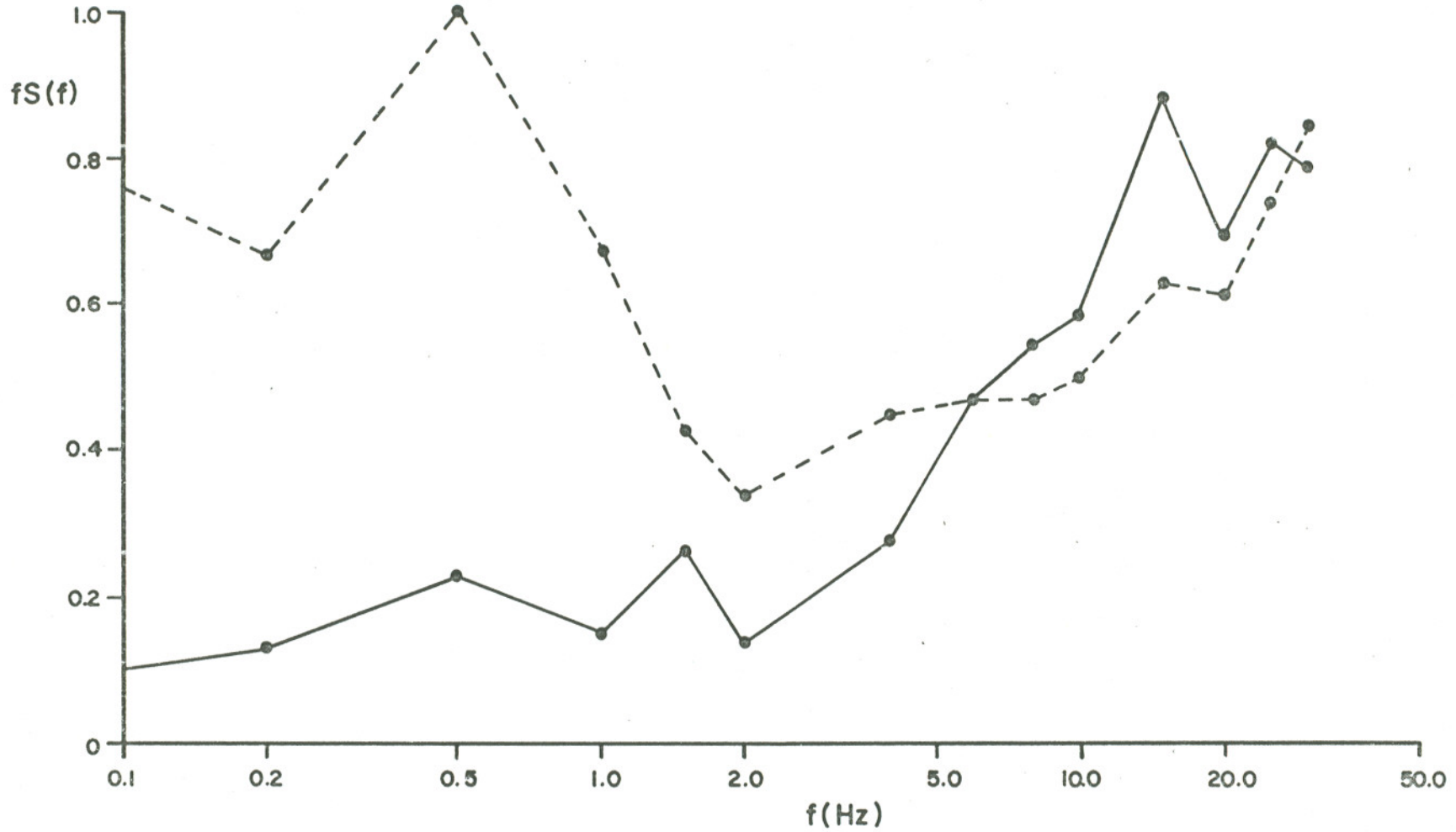

Figure 52. Frequency-weighted spectrum of the log-irradiance fluctuations sensed by the target detector for conditions of non-tracking (-----) and tracking (———) ($\rho_o/D = 3.2 \times 10^{-2}$).

the predicted rms wander angle is 13 μrad . The experimentally measured wander angle was found by using the computer to calculate the average error signal voltage variance for approximately 300 seconds of averaging time (and an effective high pass cutoff of 1/10 Hz). This result is then calibrated by the system response. We observed

$$\Phi_E = \sqrt{(2.77 \times 10^{-3} \text{ volts}^2)(2.13 \times 10^{-4} \text{ rad})^2}$$

$$\Phi_E = \quad 11 \quad \mu \text{ rad}$$

Naturally, not all of the measurements gave such close agreement as can be seen in Table XIV.

The measurements indicated that rms displacements as much as 35μrad were induced (about four times the diffraction limited beam width for these experiments). Table XIV further illustrates an important characteristic of the measured wander signals: wander is not an isotropic phenomenon. The rms deviation angles in the vertical and the horizontal directions were different. A striking example of this effect is provided by Figs. 53 and 54. The primary difference between these two is the shifting mean of the vertical data compared to the relatively invariant mean of the horizontal data. This pair of figures provides an excellent illustration of the differences between the mean angle of arrival which is affected by very slow shifts in the atmosphere's thermal gradient and the variance in the angle of arrival which is predicted by arguments like Eq. 40.

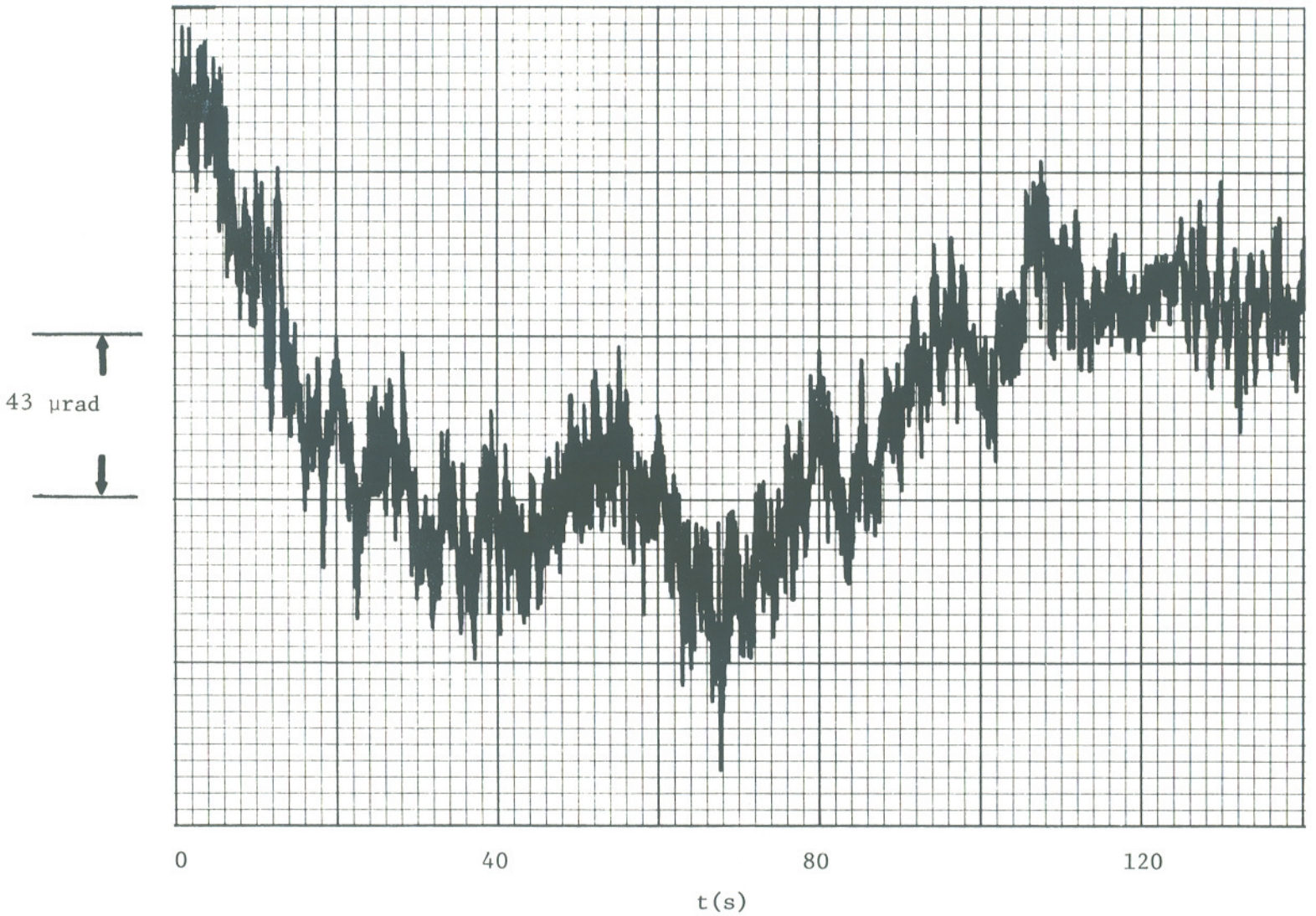

Figure 53. Vertical wander signal vs. time for a night-time run in low wind.

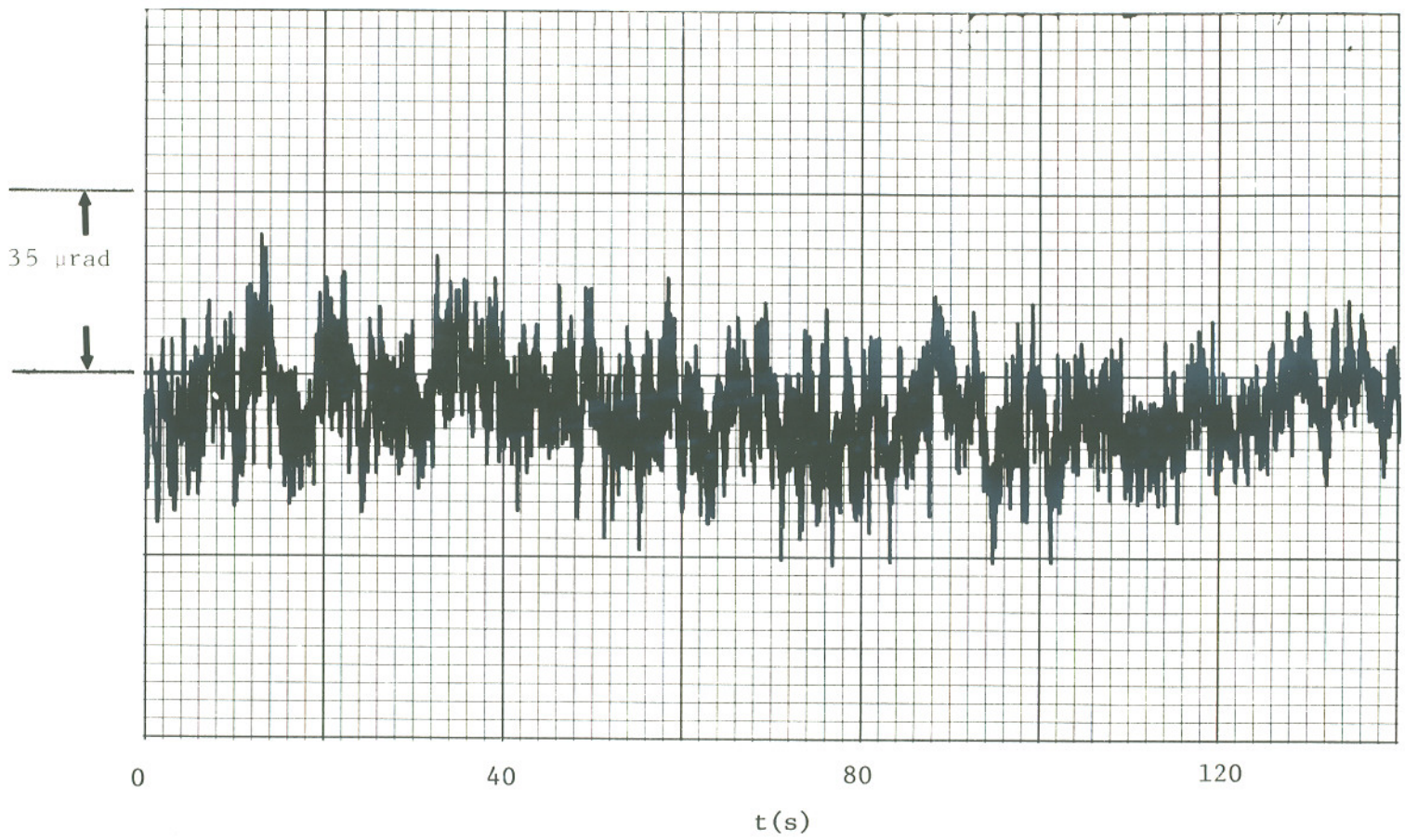

Figure 54 . Horizontal wander signal vs. time for a night-time run in low wind.

Table XIV. RMS Wander Angle

The rms wander angles are given for the experimentally measured vertical (Φ_{E_V}) and horizontal (Φ_{E_H}) components along with the predicted value (Φ_T). The averages for the listed numbers is indicated by an overbar.

C_n^2	$\Phi_{E_V}(\mu rad)$	$\Phi_{E_H}(\mu rad)$	$\sqrt{\Phi_{E_V}^2+\Phi_{E_H}^2}$	$\Phi_T(\mu rad)$
7.8×10^{-13}	29.9			29.7
5.6×10^{-13}	14.9	21.1	25.8	25.8
1.2×10^{-13}	6.90	9.39	11.7	19.5
3.3×10^{-14}	5.89	9.51	11.2	7.47
7.8×10^{-15}	5.88	7.60	9.61	5.04
4.9×10^{-15}	2.63	2.57	3.68	4.01
2.3×10^{-15}	6.24	11.0	12.6	2.73
9.9×10^{-16}	3.79	5.22	6.45	1.80
2.6×10^{-16}	2.34	4.41	4.99	0.907

Summary:

$$\frac{\bar{\Phi}_{E_V}}{\bar{\Phi}_T} = 0.809$$

$$\frac{\bar{\Phi}_{E_H}}{\bar{\Phi}_T} = 1.05$$

$$\frac{\bar{\Phi}_E\sqrt{V^2+H^2}}{\bar{\Phi}_T} = 1.28$$

III.C.2.b. Probability Distribution

Figs. 55 and 56 also provide useful examples of the probability distribution of wander. By reciprocity arguments, wander should be normally distributed. The distribution of the horizontal data was gaussian as seen in Fig. 55, regardless of the cutoff frequency of the high pass filter function. For 100 seconds total averaging time the horizontal beam displacements exhibited coefficients of skewness and kurtosis of 3.6×10^{-4} and 3.1, respectively. The values for an ideal gaussian distribution are 0 and 3.0. In contradistinction to these coefficients the vertical data gave skewness and kurtosis of 1.2 and 3.3, respectively, for 100 seconds averaging. Fig. 56 suggests that the vertical fluctuations in beam position could be considered gaussian only for a high enough high pass cutoff frequency to eliminate the slowest fluctuations, e.g., 0.05 to 0.1 Hz.

Table XV summarizes the values of these important beam wander parameters for a range of turbulence conditions. In general the fluctuations were nearly gaussian in nature and varied linearly with C_n^2, but wind effects in the horizontal plane generated significant deviations from this behavior.

III.C.2.c. Spectra

The spectral characteristics of the angular variations were discussed in Section (III.A.2.) and were shown to depend on two breakpoints. No measurements were made for frequencies below f_1. However, Fig. 57

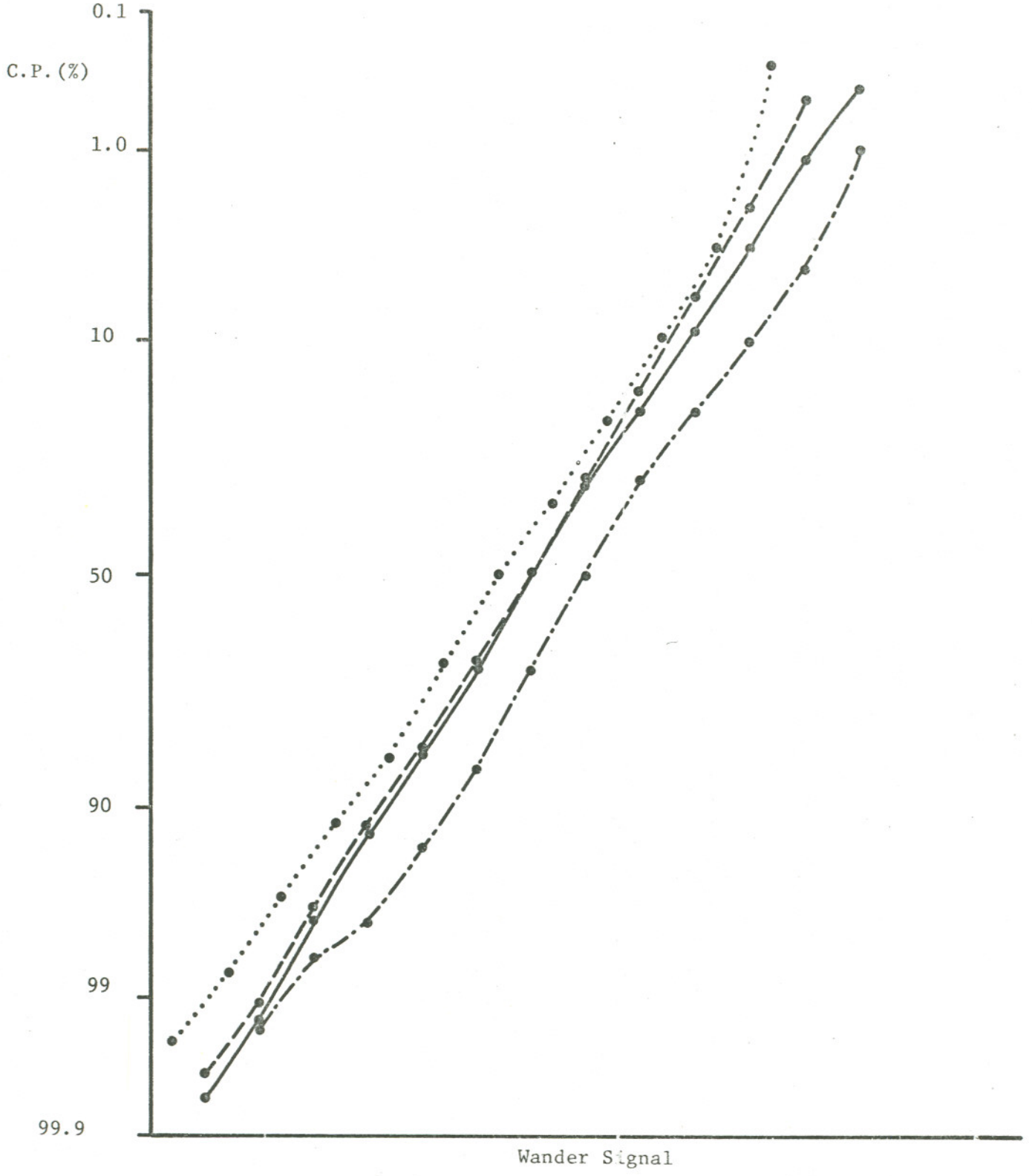

Figure 55. Cumulative probability (C.P.) for wander signal of Fig. 54, for various high-pass cutoff frequencies. The inverse cutoff frequency for (———) is 0.01; (-----), 0.017; (.....), 0.05, (-.-.-.-.-.), 0.1 sec.

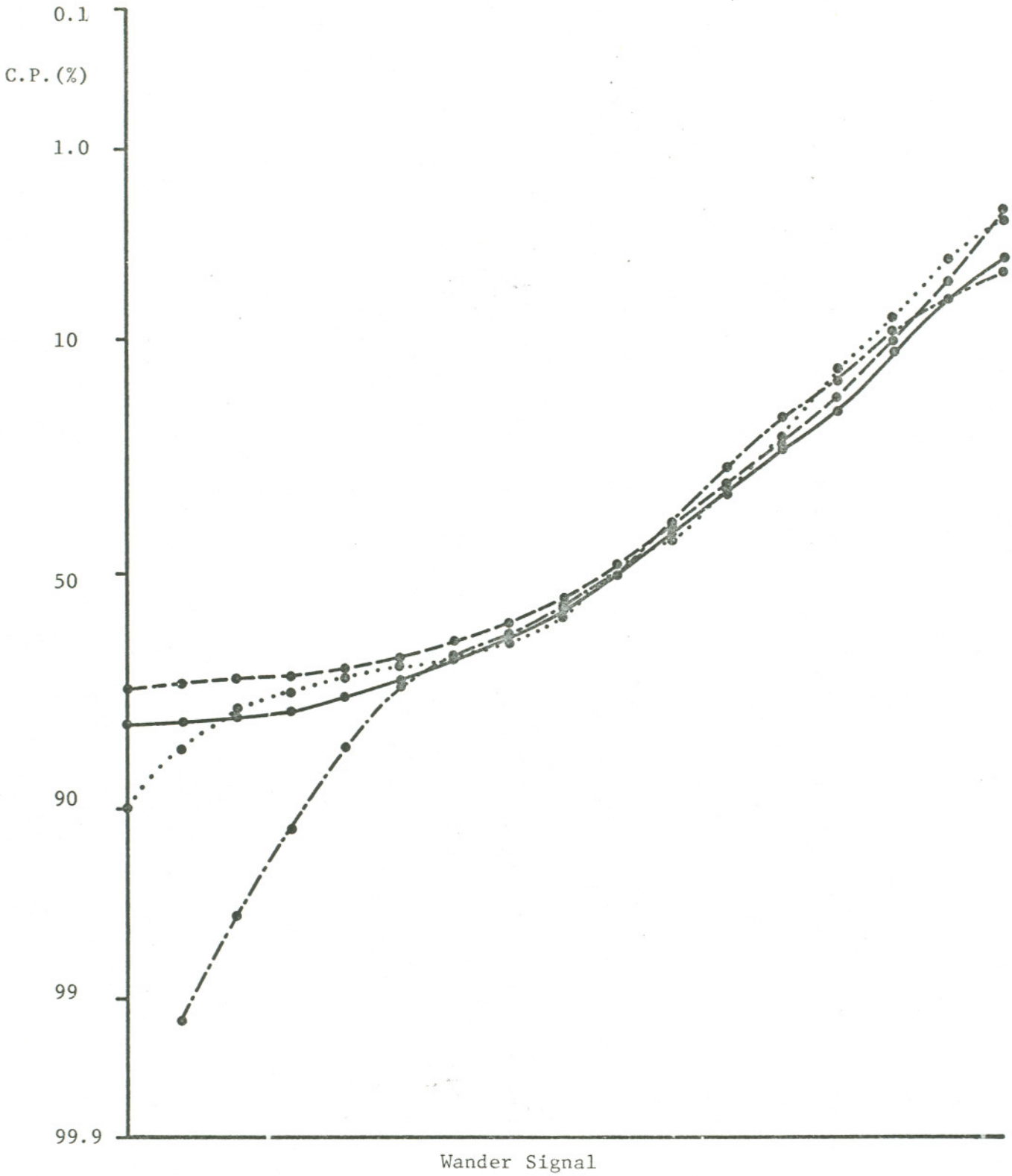

Figure 56. Cumulative probability (C.P.) for wander signal of Fig. 53, for various high-pass cutoff frequencies. The inverse cutoff frequency for (———) is 0.01; (-----), 0.017; (.....), 0.05; (-.-.-.-.-.-.), 0.1 sec.

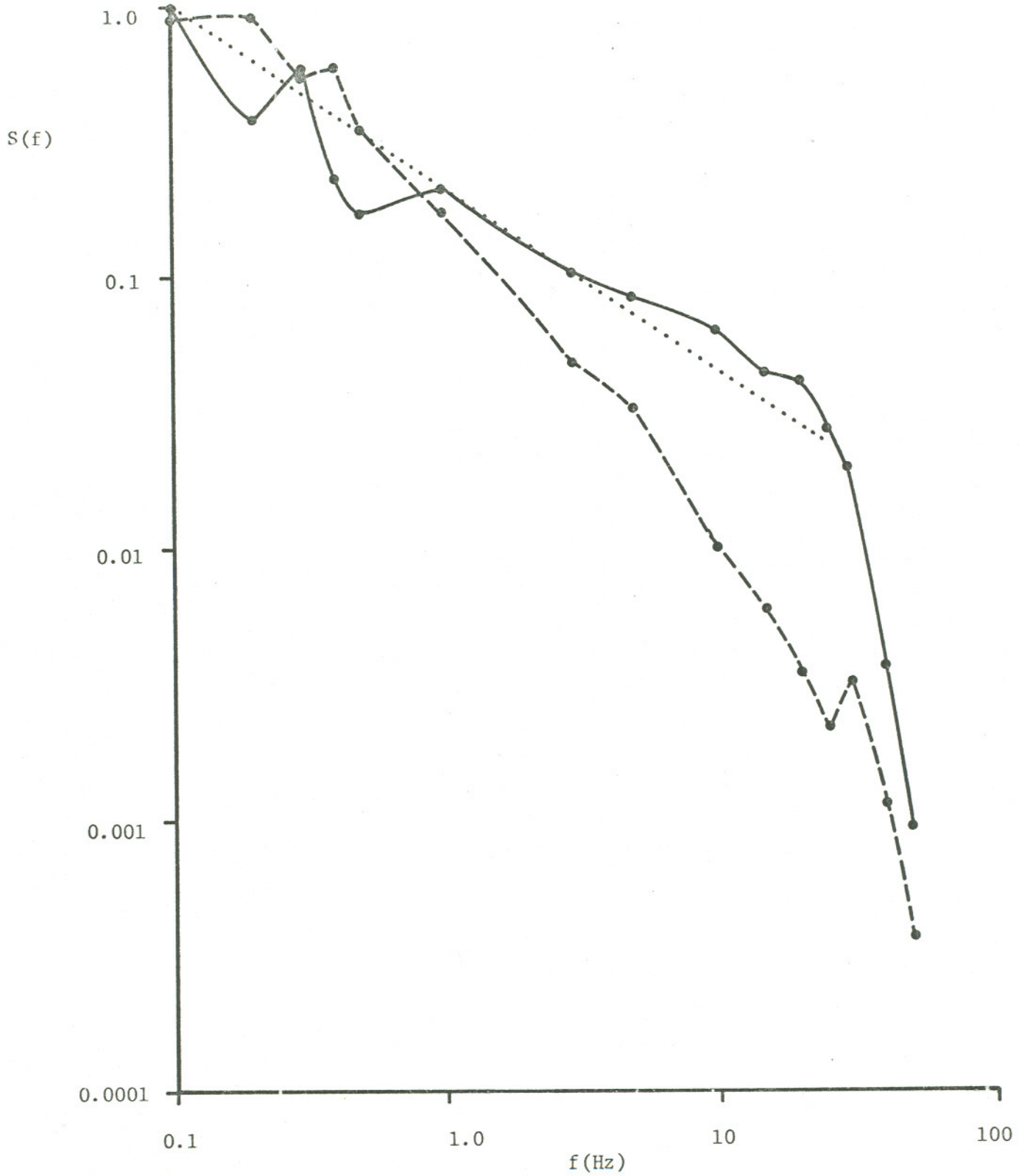

Figure 57. Power spectrum of horizontal (———) and vertical (-----) wander signals for significant horizontal wind. (.....) indicates $f^{-2/3}$ dependency.

Table XV. Wander Statistics

Φ	Skewness	Kurtosis	Correlation with C_n^2
Vertical	2.0×10^{-2}	2.76	0.90
Horizontal	2.3×10^{-2}	2.89	0.36
Total			0.97

illustrates a case when $f_1 < f < f_2$, and the log-log slope was approximately (-2/3). Fig. 58 provides data fitting the third criterion ($f > f_2$), and a spectral decay of about $f^{8/3}$ was found. Finally, there were cases which did not support these predictions as is evident in Fig. 59. However, this conclusion may be due to the limited bandwidth considered.

III.D. CONCLUSION

The experiments described by this chapter have provided the most comprehensive study of beam wave propagation characteristics yet accomplished. Measurements of important quantities showed detailed dependencies on a very fundamental parameter, D_g/ρ_o. In fact, the maximum increase in the on-axis mean irradiance as a result of tracking occurred when D_g/ρ_o was of order unity. Data indicated that the tracking advantage will be negligible if the transmitter aperture is not adjusted to fit the turbulence conditions stipulated by ρ_o. Furthermore, a maximum decrease in the fluctuations about the mean irradiance occurred for tracking when D_g/ρ_o was,

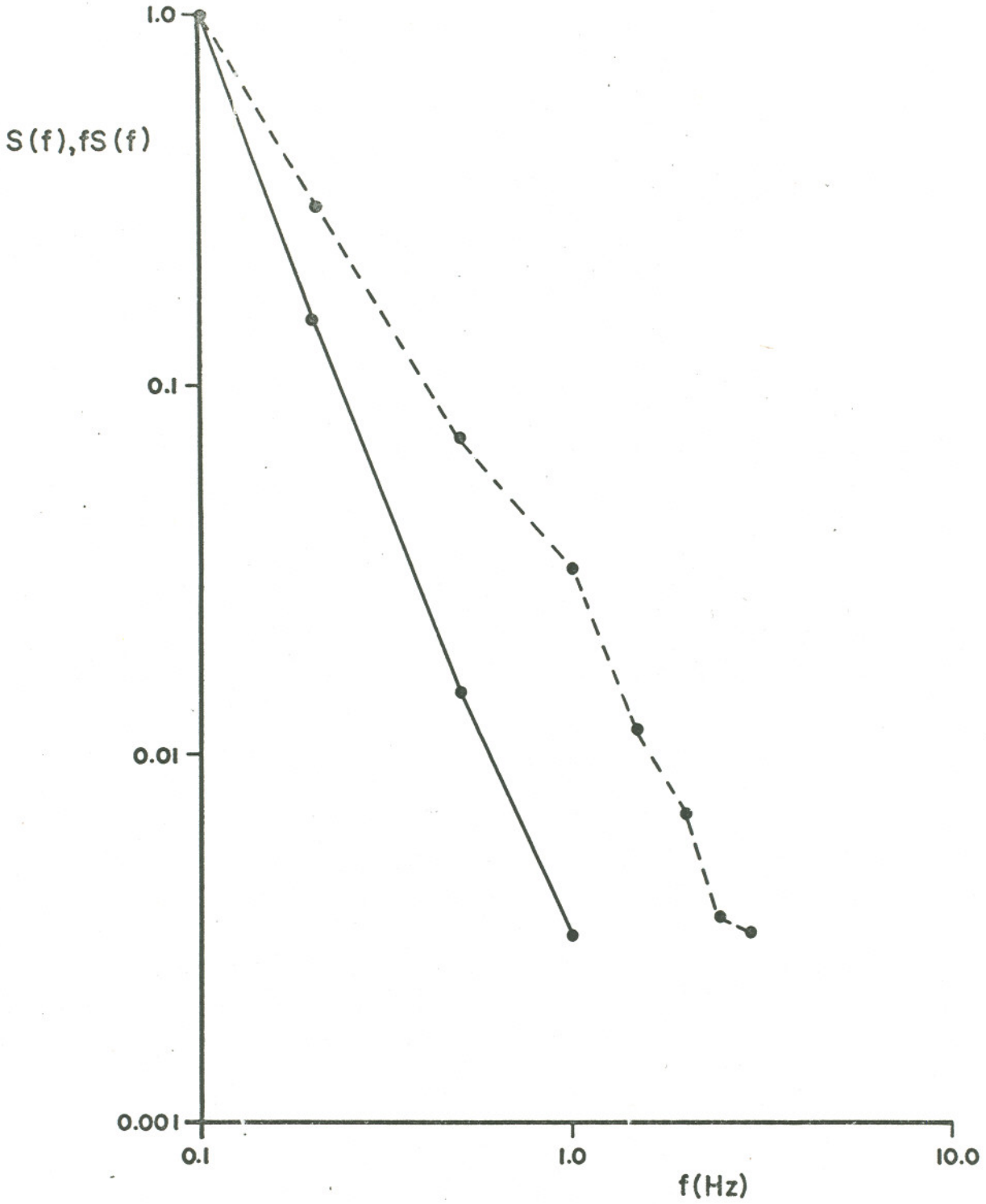

Figure 58. Power spectrum S(f) (———) and frequency-weighted spectrum fS(f) (-----) for wander signal of Fig. 54.

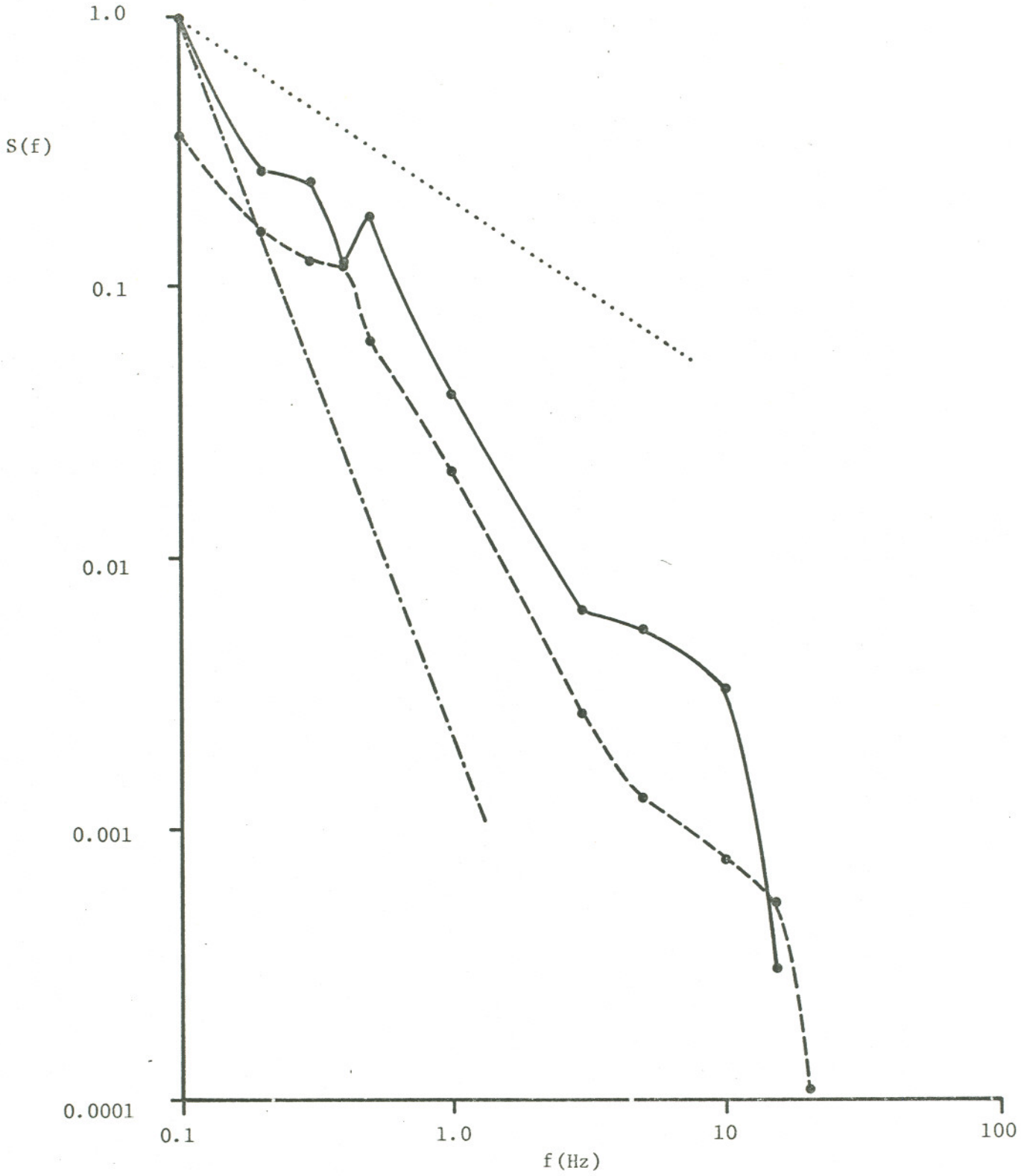

Figure 59. Power spectrum of horizontal (———) and vertical (-----) wander signals for low wind speed, exhibiting slopes intermediate to the theoretical values of -2/3 (.....) and -8/3 (-.-.-.-.-.).

again, of order unity. These two facts suggest that D_g/ρ_o of order unity is a special combination of beam-geometry and turbulence conditions that generates maximum beam wandering. The detailed parametric effects of D_g/ρ_o on the mean irradiance and the fading of a beam wave were found to be in good agreement with recent theoretical accomplishments.

In addition, temporal spectra of the target detector signals corroborated that reciprocity-tracking effectively reduced wander. Cancellation of specific low frequency peaks was found, especially during weak turbulence. During strong turbulence the spectra showed significant broadening due to the break-up of the beam into independently scintillating patches. Finally, tracking tended to increase the log-normality of the intensity fluctuations.

The tracking servo system's error signals provided an indirect analysis of wander. Typically, wander was observed to be nonisotropic. But generally, theoretical predictions of the magnitude and the statistics of wander did agree with measurements. Also verified were theoretical descriptions of the wander spectra.

In conclusion, beam wave propagation may now be considered to be well understood for virtually all important atmospheric propagation conditions.

CHAPTER IV: SUMMARY AND SUGGESTIONS

Chapter I provided unique experimental results regarding the propagation of quasi-point laser sources through the turbulent atmosphere. The covariance function was discovered to be drastically modified by conditions of strong turbulence. Further, the log-amplitude variance at 10.6 μm was observed to saturate for the first time. The experimental measurements were found to be in good agreement with recent theoretical models. Hence the combined progress of the experiment described in Chapter I and recent theoretical work has led to a nearly complete understanding of optical propagation during conditions of strong atmospheric turbulence. Two details, however, are fundamental to the total description: supersaturation and related probability distributions. Since the long-path measurements of this dissertation may be biased by spatial and electronic filtering, an additional experiment should be performed utilizing a much smaller receiver size and a much larger receiver bandwidth. This new experiment could then provide the remaining information. In addition, the covariance function and ρ_o should be measured directly to test whether the covariance scale size goes exactly to ρ_o at saturation. If this is verified, then the effects of receiver aperture averaging should be completely detailed for the new covariance function dependence.

With respect to finite beam wave propagation, Chapter II showed that a passive beam provided no advantage over the fade characteristics

of the quasi-point laser source. In addition, it was found that the wander phenomenon was not included in the Rytov approach to beam wave propagation. In Chapter III this wander effect was cancelled by use of a fast-tracking transmitter, and the finite transmitter aperture averaging effect was still unobservable.

However, D_g/ρ_o dependencies were observed as predicted by the new comprehensive, unified theory. Not only does this fact prove that reciprocity is valid in the turbulent atmosphere, but the data of Chapter III indicates nearly universal curves for predicting the propagation behavior of beam waves. This is emphasized by the fact that the normalized variance of the linear irradiance for the non-tracked case exhibited a pronounced peak at D_g/ρ_o of order unity. By reciprocal arguments, this critical point could be used to measure ρ_o over any path (vertical or horizontal and inhomogeneous) provided that a point or edge type source is available for imaging in a simple telescope with a variable aperture. Consequently, most beam wave effects could be predicted for the representative conditions.

Extensions of the beam wave study should include a CO_2 tracking experiment to determine L_o effects and any possible deficiencies in the theoretical model of the turbulent spectrum. Further, an extensive study of the statistical nature of ρ_o should be conducted. In addition to these experimental suggestions, there remain theoretical details to be solved. For instance, the issue of whether or not a MTF_{ST} really exists should be

resolved along with its complete solution for the truncated gaussian weighting case. Some insight may be obtained by understanding why the results of Kon do not agree with the results discussed herein. Finally, the effects of receiver aperture averaging on the angle of arrival and its power spectrum should be theoretically detailed.

APPENDIX I. DESIGN OF A RECIPROCITY TRACKER FOR CANCELLATION OF BEAM WANDER

Introduction

In Chapter II experimental investigations showed that wander induced by the atmosphere hindered statistical measurements of fluctuations – or lack of fluctuations – in the central maximum of a nearly diffraction-limited beam. This situation is illustrated in Fig. 60a. The goal of this appendix is to describe the design of a tracking system to cancel this atmospheric effect.

Supposing that there is some additional uninterrupted channel (Fig.60b) between the transmitter and the receiver, the centering error detected by a special receiver (divided into quandrants) could be used to adjust the transmitter steering via the scanners S. Hence an appropriate feedback system could be designed to alleviate the wander problem. However, for many potential applications in communications, ranging and remote sensing, the additional receiver-transmitter link is unavailable. A different method of beam wander cancellation must be devised.

The answer may be in a combination of reciprocity principles and the use of a retro-reflector. The output of a retro is at the same angle as the received radiation. Hence, one is able to set up reciprocity relations between points T_x and R_x in Fig. 61a. Centering errors sensed by a detector at the transmitter location can be used in a feedback system whose

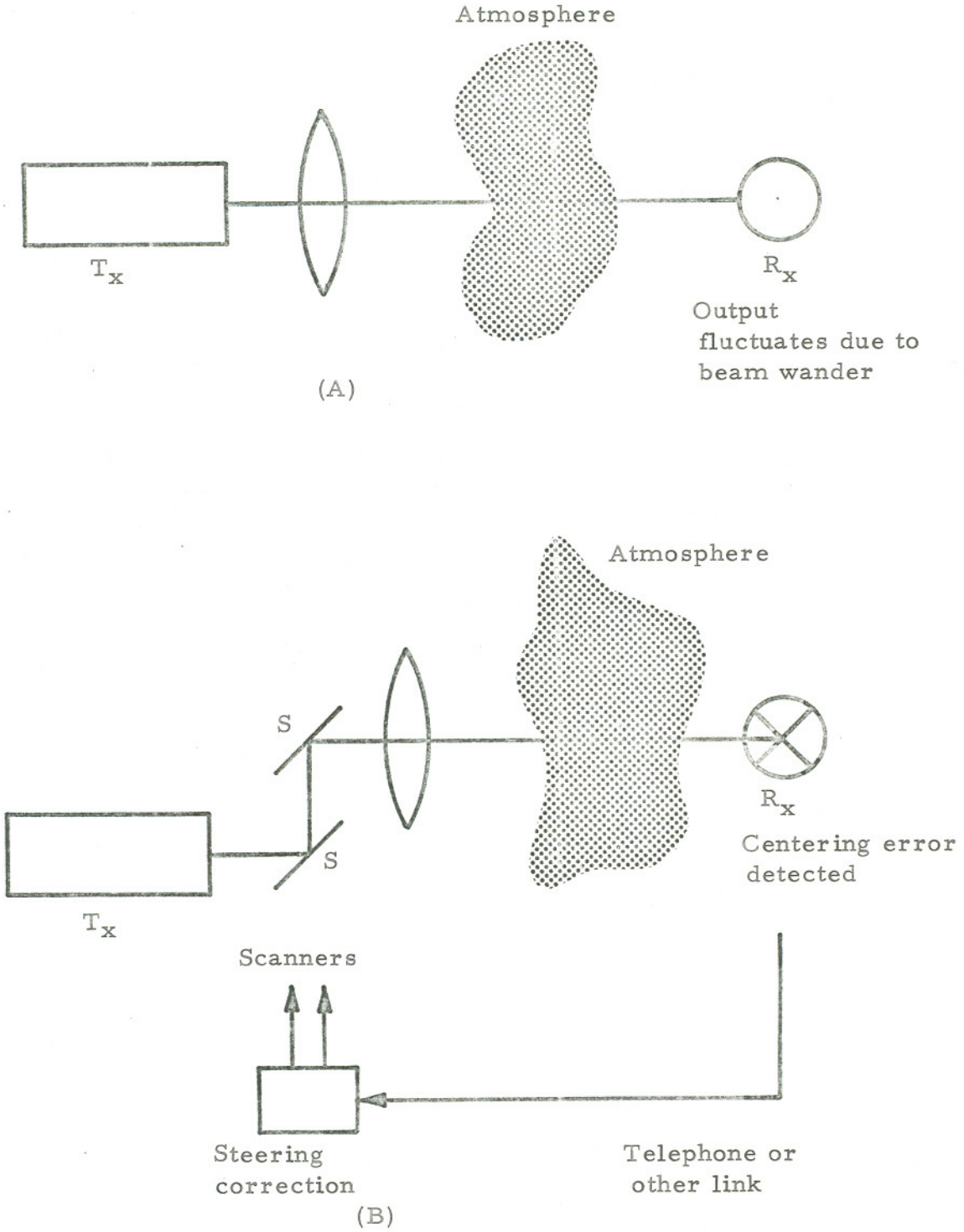

Figure 60. Wander and its cancellation via an uninterrupted channel.

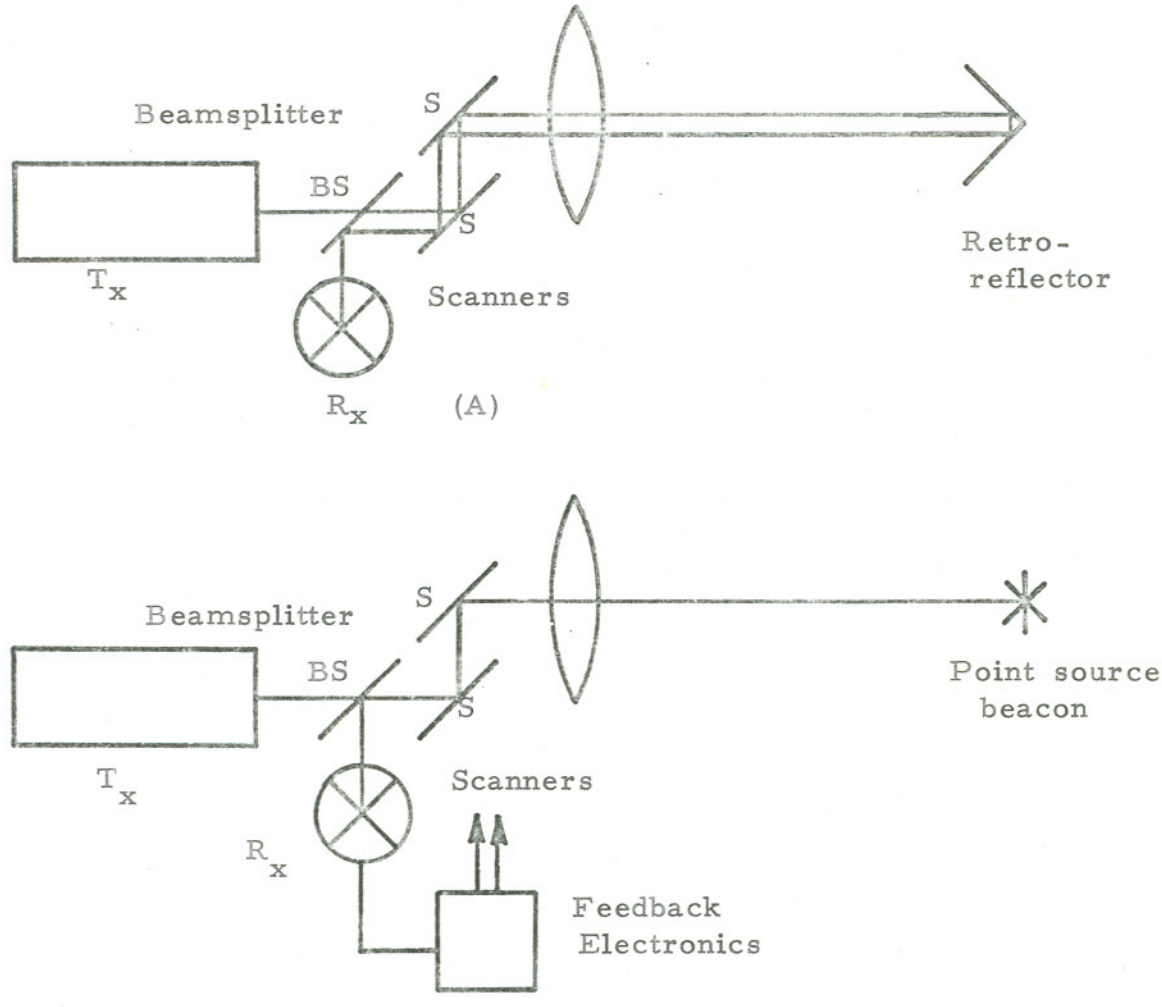

Figure 61. Wander cancellation through the atmosphere using reciprocity.

net result is elimination of beam wander at the retro-target. The actual system utilized a quasi-point source beacon in place of the retro (Fig. 61b). This was done to provide a clean set of experiments void of ambiguity due to possible unsolved tracking problems related to the use of a retro,[128-133] and untested complications related to folded paths.[134-136] In addition this approach would allow measurements of the point source angle of arrival fluctuations as spatially filtered by the tracking transmitter aperture. These measurements, reciprocal to the finite transmitter beam wander in the target plane would provide quantitative analysis of the beam wander phenomenon, per se. A key feature of this approach is the application of reciprocity through the turbulent atmosphere.

A. Reciprocity Through the Turbulent Atmosphere

Originally, Shapiro[137] set limits on the applicability of the theory of reciprocity through a turbulent medium. However, Fried and Yura[138] favor a generalization that allows immediate insight into the understanding of the propagation characteristics of a finite beam[107] via earlier analyses of optical heterodyne receivers,[111,114,116,139] and image resolution.[94,108] Subsequently, the concept was tested[140] and the conclusion drawn that reciprocity did apply to the turbulent atmosphere.

To illustrate the concept of reciprocity as applied to the problem of wander cancellation, we follow a discussion similar to that given by Brown.[141]

In Fig. 62 the diagram is divided into a turbulent and a non-turbulent region by an optical system. For the case of interest, this optical system is a receiver and/or transmitter telescope. The angle of arrival of wavefronts from radiation emitted by P_1 is randomly tilted at the lens position by the intervening turbulence. The lens or optical system transforms this random tilt into a random wandering of the image of P_1 which is noted as P_2. If we have a tracking system capable of placing a radiator at the point P_2, then by reciprocity the centroid of this new radiator's power distribution (in the plane of P_1) will be precisely centered about P_1. This will be true regardless of wavefront distortions impressed on the radiation by the turbulence.

Now, we apply a more practical tracking scheme, as illustrated by Fig. 63. A position sensing detector is placed on the optical axis of the system. If the image of P_1 tends to wander the detector will sense a position error. A feedback system using this error signal can drive a servo system that will steer P_2 back on to the system's optic axis. In this fashion P_2 is forced to remain stationary. Then, the trivial extension is to couple in a laser beam at P_3. The irradiance distribution of the laser will now have its power centroid actively steered to intercept P_2 in the target plane. The conceptual design of the required feedback system will be discussed next.

B. Conceptual Design of the Feedback System

If we model the wander of the target beacon image in Fig. 63 as a steady-state position change, then a type-1 system response is specified.[142]

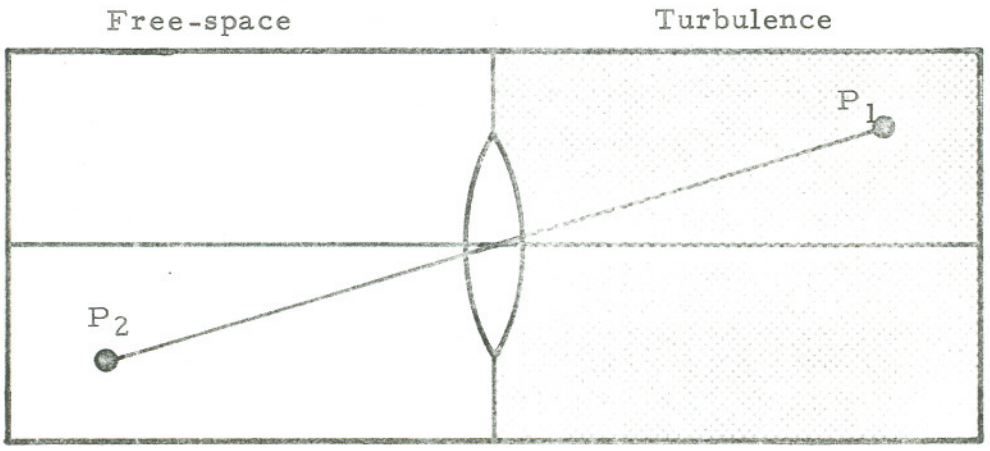

Figure 62. Reciprocity and tracking of an image.

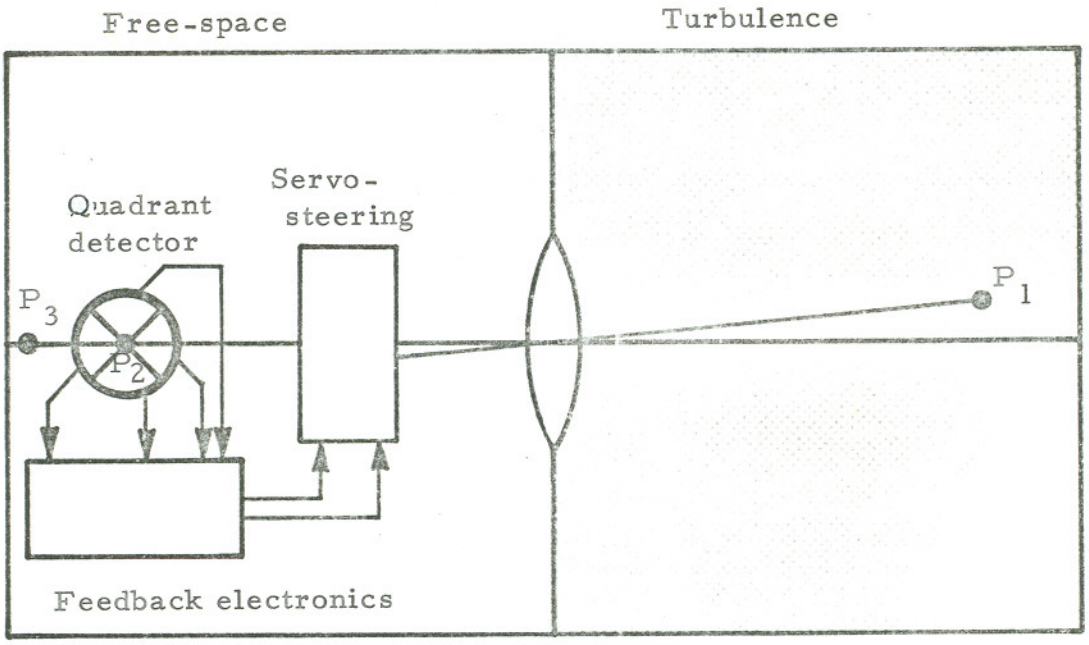

Figure 63. A practical tracking system.

Error analysis shows that for a stable type-1 unity feedback system the steady-state position error (steady-state error when the input is a unit step function) approaches zero. The s-domain diagram of our proposed system is given in Fig. 64. The open loop transfer function is

$$GH = G \propto \frac{1}{S} \tag{41}$$

which implies a single integration for the open loop in the time domain. To further define the constants involved with our system design, let us consider the system in the time domain.

A simplified schematic diagram of the electronic system is provided by Fig. 65. The photodiode, PD, is modelled to convert the angular position change in the beacon image into an electrical current change. This is done by observing that

$$i(t) = D_2 P(t) \tag{42}$$

where D_2 is the responsivity of the diode (units of amp/watt) and $P(t)$ is the incident power. But there is also a position-angle to incident power conversion, such that the diode current is given by

$$i(t) = D_1 D_2 \theta_i(t) \tag{43}$$

in which D_1 is a geometrically derived conversion of angle to incident power (units of watt/radian). Thus the conversion from an angular position to an electrical current is fully modelled.

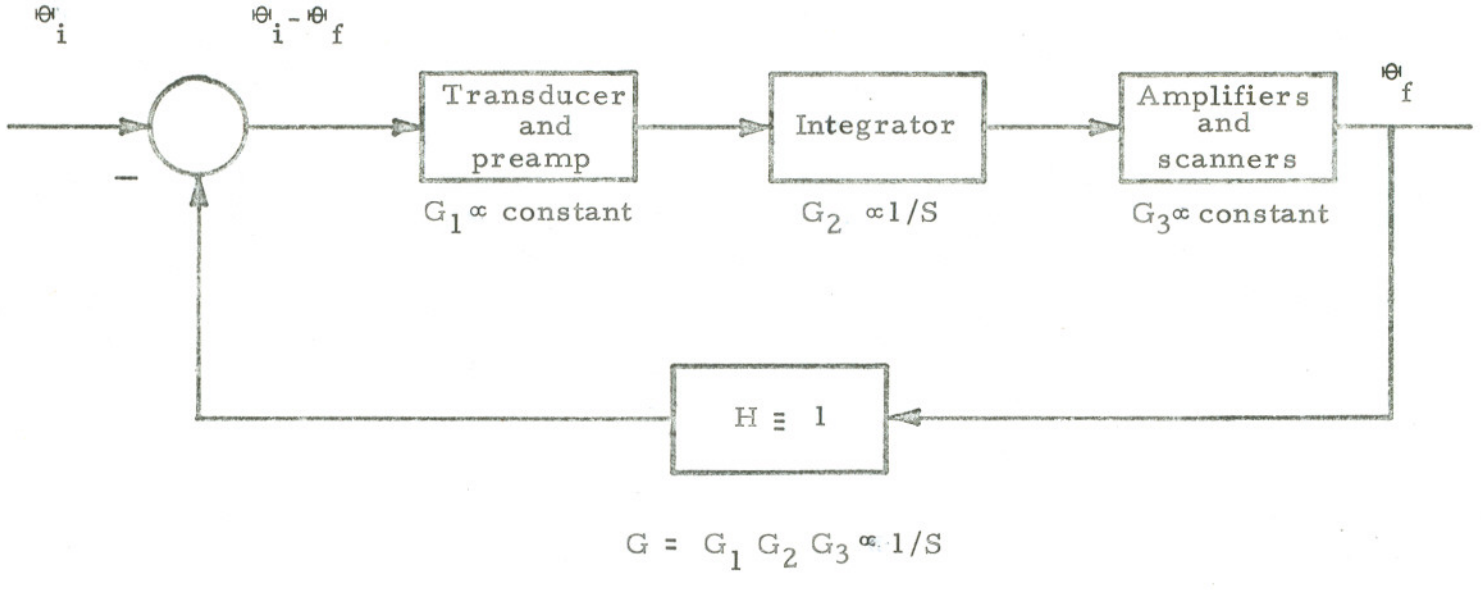

Figure 64. S-plane diagram of basic tracking system.

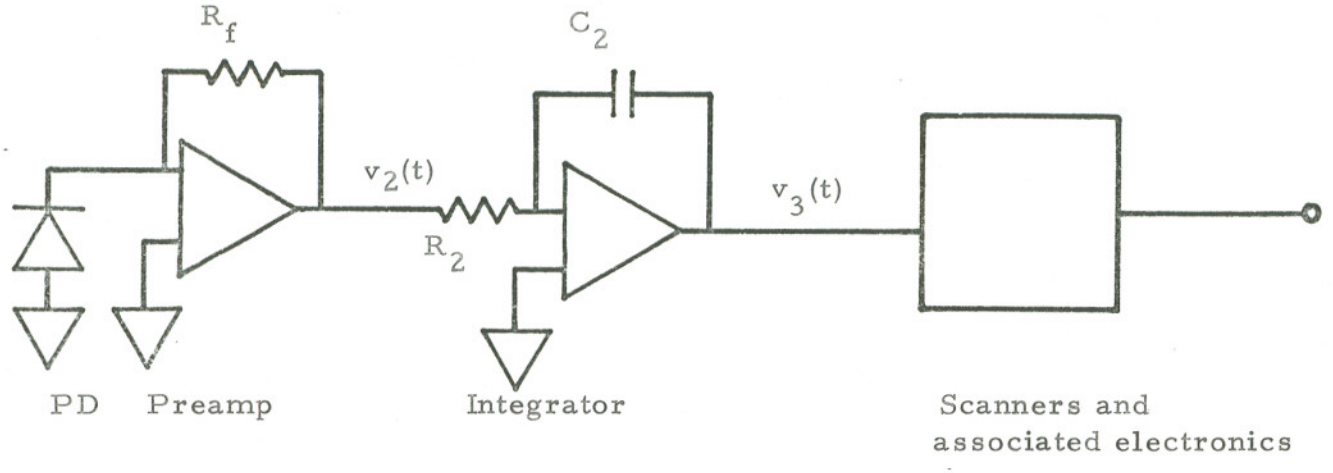

Figure 65. Basic schematic of tracking electronics.

The role of the servo-scanners is to convert the modified position error from an electrical signal back into an angular position. This is accomplished by the conversion

$$\theta_f(t) = D_3\, v_3(t) \tag{44}$$

where D_3 is the sensitivity of the scanners (units of volt/radian).

With these basic constants defined the response of the electronics of Fig. 65 is determined by a set of three equations

$$\begin{aligned} v_3(t) &= D_3\, \theta_f(t) \\ i(t) &= D_1 D_2 \theta_i'(t) \\ \theta_i'(t) &= \theta_i(t) - \theta_f(t) \end{aligned} \tag{45}$$

Hence the intermediate voltage, $v_3(t)$, can be described as

$$v_3(t) = \frac{R_F}{R_2 C_2} \int i(t)\, dt \tag{46}$$

Combining Eqs. (45) and (46)

$$\theta_f(t) = \frac{R_F D_1 D_2}{R_2 C_2 D_3} \int [\theta_i(t) - \theta_f(t)]\, dt \tag{47}$$

This last expression allows one to obtain a detailed differential equation for the system.

Transforming back into the s-domain we observe a simple result

$$S\, \Theta_f(s) + K\, \Theta_f(s) = K\, \Theta_i(s) \tag{48}$$

where

$$K \equiv \frac{R_F D_1 D_2}{R_2 C_2 D_3}$$

Hence the system transfer function is

$$P(s) = \frac{K}{s+K} \tag{49}$$

To check the stability of the system, observe that the characteristic equation is

$$(s+K)\,\Theta_f(s) = 0 \tag{50}$$

The root is $s = -K$ indicating that the system is stable.

The closed loop gain of the system is

$$P(j\omega) = \left(\frac{K^2}{\omega^2+K^2}\right)^{1/2} \tag{51}$$

In terms of Bode-analysis

$$\text{so } \log_{10}\left|P(j\omega)\right| = 20\log_{10}\left(\frac{1}{\omega^2/K^2+1}\right)^{1/2} \tag{52}$$

So for $\omega << K$

$$20\log_{10}\left|P(j\omega)\right| = 10\log_{10}(1) = 0 \tag{53}$$

Or for $\omega >> K$

$$20\log_{10}\left|P(j\omega)\right| = 20\log_{10}(\omega/K) \tag{54}$$

The resulting Bode diagram is given in Fig. 66, where the straight line approximation gives a slope of 20 db/decade with a maximum error of 3 db (at $\omega = k$).

The loop gain parameter, K, is set by the frequency response requirements of our goal to cancel wander. From Fig. 67 it is clear that one desires the cutoff frequency to be about 20 Hz. Thus $\omega = k$ yields

$$2\pi(20\ \text{Hz}) = \frac{R_F D_1 D_2}{R_2 C_2 D_3} \tag{55}$$

A basic power analysis of the entire system will provide the final information to define the values of R_F and $R_2 C_2$.

C. Basic Power Analysis

C.1. Source Capabilities

Fig. 68 contains a very basic schematic of the optical system. The minimum power available to the quadrant detector will be

$$P_{o_{min}} = T_1 T_2 P_B \left(\frac{A_T}{A_B}\right) \tag{56}$$

where T_1 and T_2 are the transmission coefficients of the system components and the atmosphere, respectively. P_B is the output power of the laser beacon, and A_T/A_B is the ratio of the receiving telescope area to the area illuminated by the beacon in the receiver plane. T_1 is approximately 0.32 if the transmission of the lens and mirrors are taken to be 0.92 and 0.94, respectively, and the beamsplitter is of 50-50 type.

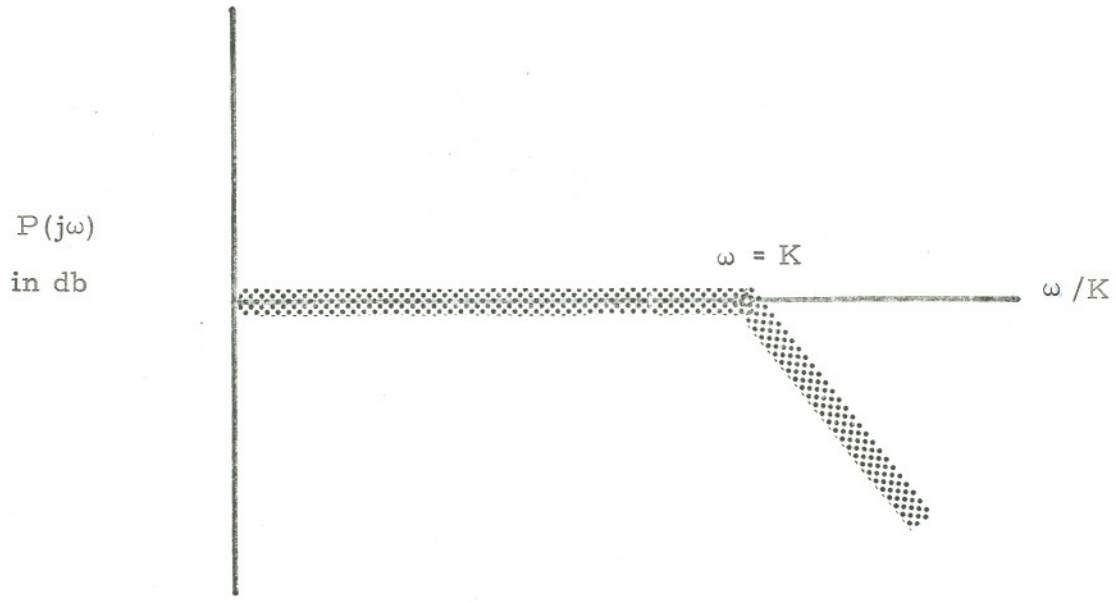

Figure 66. Closed loop transfer function.

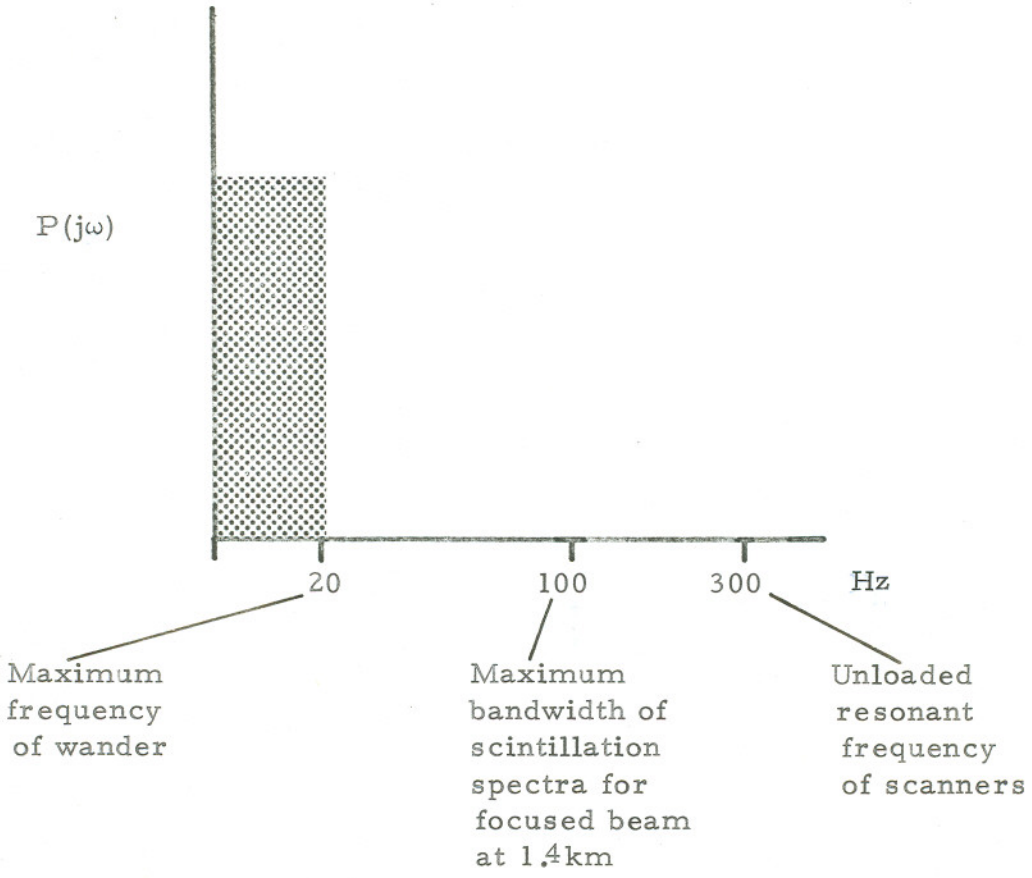

Figure 67. Bandwidth considerations.

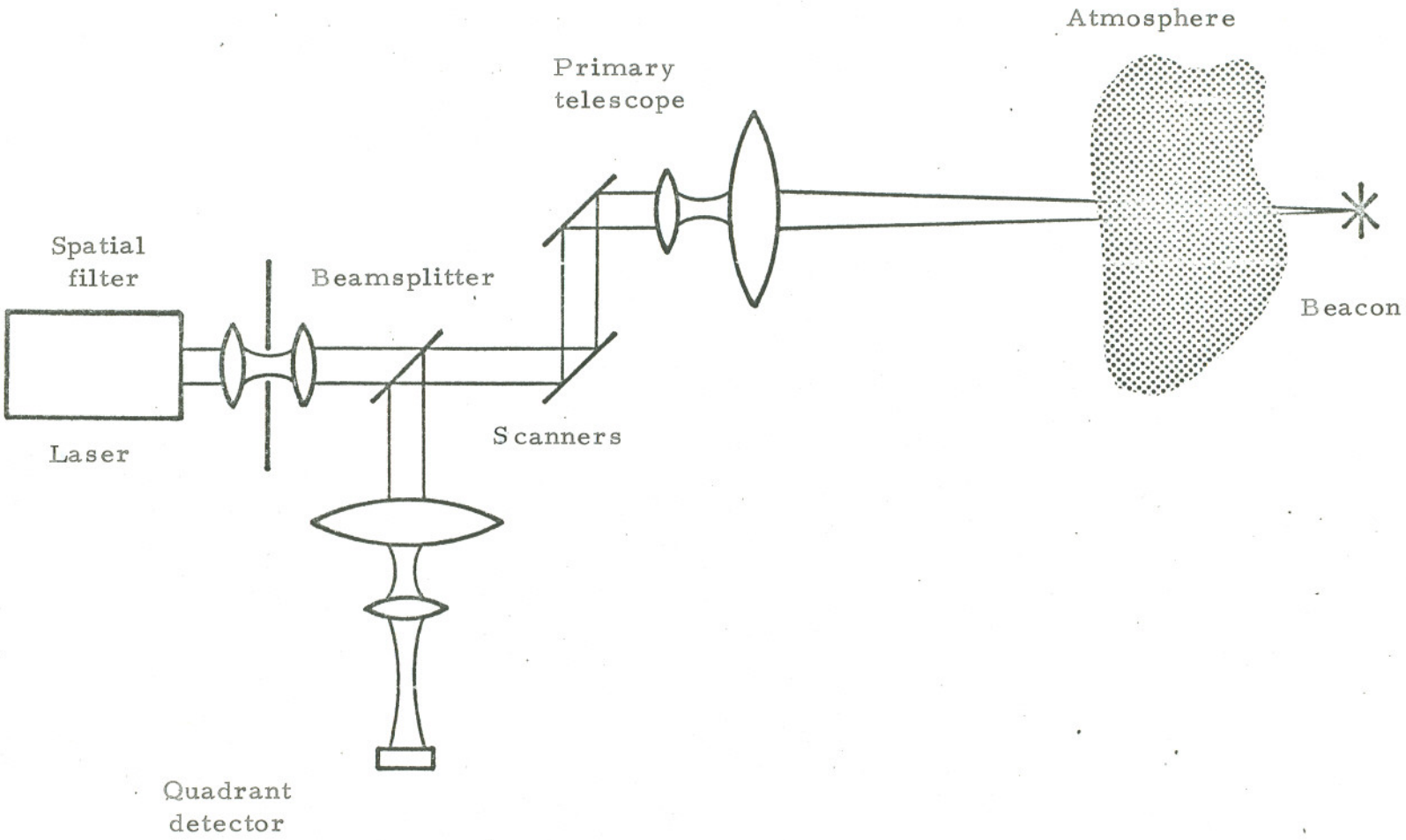

Figure 68. Schematic of basic optical system.

It should be noted that in calculating T_2, the special condition of receiver aperture averaging must be included. Then

$$T_2 = \frac{1}{T_2' G} \tag{57}$$

where G is the aperture averaging factor of the large receiver and T_2' is potential fluctuation due to the atmosphere. To obtain a representative value for T_2, note that a point detector under saturated conditions observes $\sigma_\chi^2 \sim 0.5$. The mean square intensity fluctuation is then given by [143]

$$\sigma_I^2 = e^{4\sigma_\chi^2} - 1 \tag{58}$$

and results in $\sigma_I^2 \sim 600\%$. This implies that the linear intensity level will fluctuate about a factor of $[\sigma_I^2 \times 10]$ below and above the mean level with reasonable probability. Therefore let $T_2' = 2.45 \times 10^2$. The expression for T_2 then becomes

$$T_2 = \left\{ 2.45 \times 10^2 \left[\left(\frac{r_a}{D} \right)^2 \times 10 \right] \right\}^{-1} \tag{59}$$

where r_a is the correlation length of the intensity distribution and D is the receiving aperture diameter. The factor of 10 is an approximate correction of theory to fit experiment, because it has been found that during strong turbulence, receiver aperture averaging is not as effective as predicted (see Chapter I). Eq. 59 gives $T_2 \cong 0.16$ for the case of interest.

A_B is defined by the divergence of the laser beacon. For the Spectra Physics Model 120 that was used, the divergence half-angle is 8.5×10^{-4} rad. Hence, for the 1.6 km path $A_B = 5.81\ m^2$. On the other hand, A_T is just the area of the tracking transmitter: $A_T = 1.8 \times 10^{-2}\ m^2$.

Consequently, the minimum expected power available to the entire quadrant detector surface is $P_{o_{min}} \sim 8 \times 10^{-7}$ watts. This implies that on a single quadrant we have $P_D \sim 2 \times 10^{-7}$ watts.

C.2. Detector Capabilities

The present design calls for the application of a UDT SPOT 8D quadrant detector. Its responsivitity is S = 0.4 amp/watt. The minimum current from a single section of the detector will be

$$i = SP_D = 8 \times 10^{-8} \text{ amp} \tag{60}$$

If it is desirable to obtain approximately one volt from the preamp for the above input current, then we estimate that the value of the preamp feedback resistance be $R_F = 1.25 \times 10^7\ \Omega$.

C.3. Geometric Conversion of Angular Position to Power

The angle of arrival of the beacon wavefronts at the receiving optics of the tracker will vary. Since the receiving optics consist of two telescopes, M_2 and M_1, the angles (θ_1) incident on the primary telescope are converted to angles (θ_2) at the detector by

$$\theta_2 = M_2 M_1 \theta_1 \tag{70}$$

To proceed, we must determine how θ_2 affects the power distribution on the detector. For a centered image on the detector we have the geometry of Fig. 69a. If the image is not centered, then the angular position error signal will be proportional to

$$D_1 = \frac{P' A'(\theta_2)}{\theta_1} \tag{71}$$

where $A'(\theta_2) \equiv A_1(\theta_2) - A_2(\theta_2)$ and P' is the energy density of the image on the detector. The geometry of this condition is suggested by Fig. 69b. It follows that

$$\frac{A'(\theta_2)}{\theta_1} \cong M_1 M_2 d_8 r_2 \tag{72}$$

where d_8 is the distance from M_2 to the detector and r_2 is the radius of the image on the quadrant detector. To obtain this result it was assumed that the system loop was closed, maintaining only small centering error. Finally, D_1 can be defined in detail.

$$D_1 = P' M_1 M_2 d_8 r_2 \tag{73}$$

The geometric conversion of angular position is now complete and can be applied to system calculations of Section C.

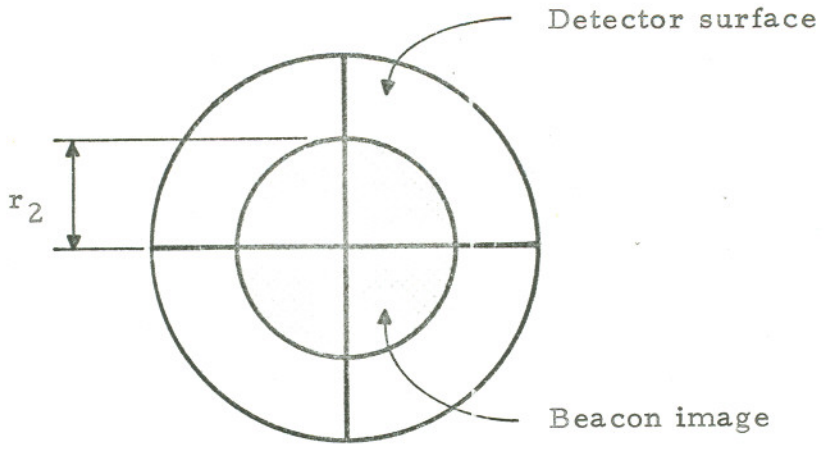

(A)

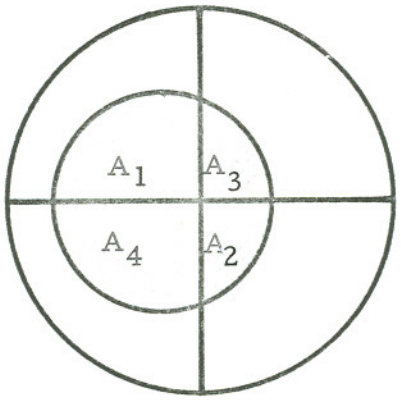

(B)

Figure 69. Angular position to power conversion.

D. Complete Optical Design

A review of preceding Sections B and C indicates that the remaining parameters required for full definition of the basic reciprocity tracking system depends on the optical system design. It is the goal of this section to detail that design. At the outset there are a few basic requirements:

1. Maximum field of view: 2 mrad
2. Utilization of 6 in. telescope objective
3. Spatially filtered beam at transmitting telescope
4. Beacon image size about 1/2 of active area of the quadrant detector
5. Utilize scanners with peak to peak angular swing of about 0.1 rad.

D.1. Basic Transmitter

Consider the basic system of Fig. 70. If the output angle is to be 2 mrad for an input of 0.1 rad, then the power of the primary telescope is given by

$$\theta_{out} = \frac{1}{M_1} \theta_{in}; \quad M_1 = 50 \tag{74}$$

The 6 in. objective, L_1, that is available has a focal length of 48 in., hence the second element, L_2, of the telescope is defined by

$$f_2/f_1 = M_1 \tag{75}$$

Resulting in $f_2 = 1$ in.

Now that the primary transmitting telescope, M_1, has been fully defined, the laser must be matched into it via a 3.8 mil pinhole. Further, $d_1 = 30$ in. to accomodate the components between the pinhole and M_1. Next,

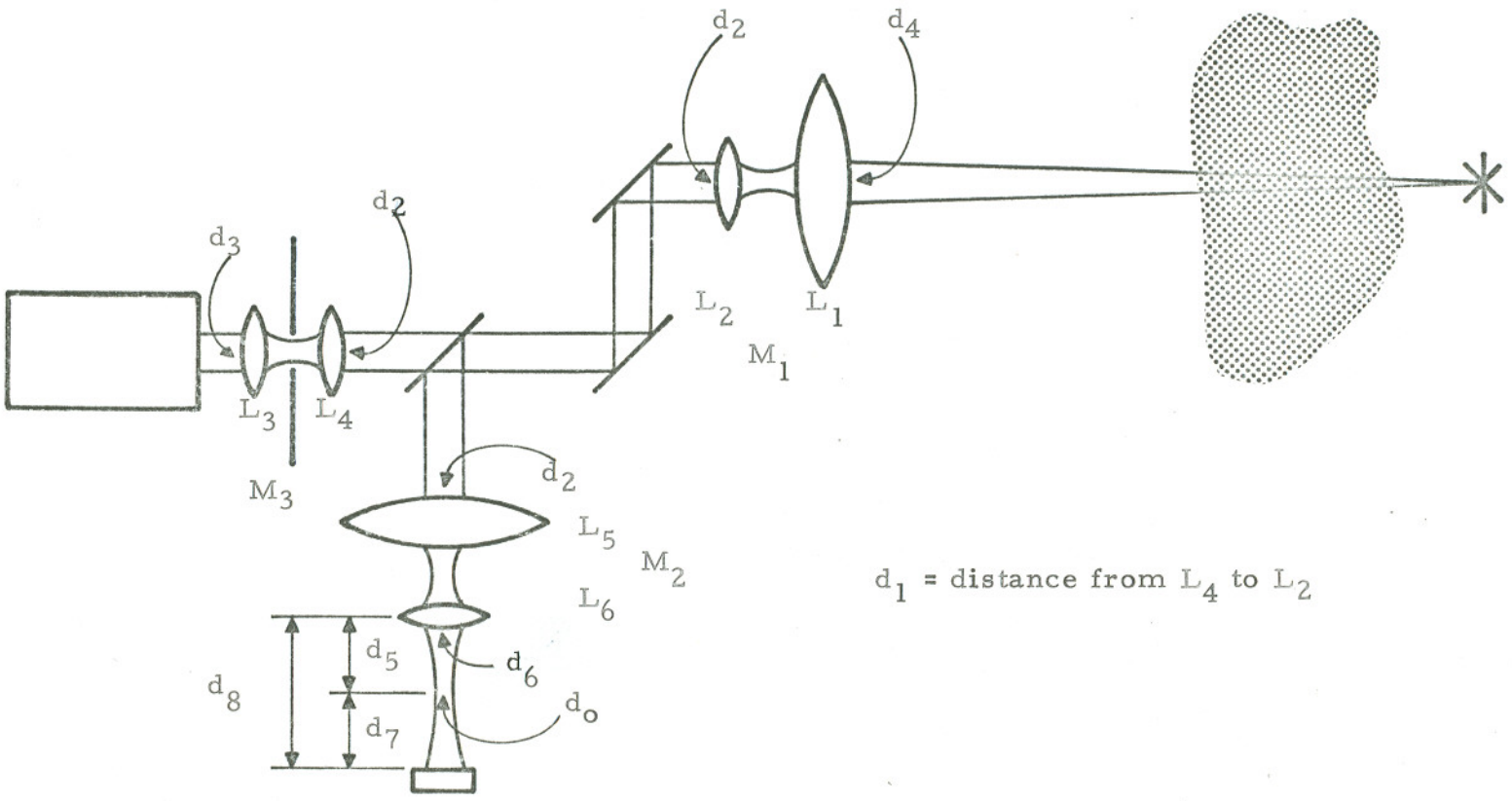

Figure 70. Complete optical diagram of the tracker.

to fill the primary telescope M_1 we must have an input beam size of d_2 at L_2, such that

$$d_4 = d_2 M_1 \tag{76}$$

with $d_2 = 1/8$ in. It is then required that the laser beam be focused through the pinhole in such a way as to fit a geometric f-cone of

$$f\# = \frac{d_1}{d_2} = \frac{30 \text{ in}}{1/8 \text{ in}} = 240 \tag{77}$$

This f# defines L_3 by

$$f_3/d_2 = 240 \tag{78}$$

(if no L_4 is assumed). An alternative method, and somewhat more flexible approach, is to use a unity power telescope to get the beam through the pinhole. Using two lenses with focal lengths of about 3 in., one can adjust the beam diameter at L_2 to d_2, then position the pinhole at the internal focus of M_3. The quality of the spatially filtered beam will be maintained if the lens L_4 is functioning at a high f#.

D.2. Basic Receiver

To develop a flexible receiver that allows for potential modifications with only simple changes we utilize a secondary telescope, M_2. If the lenses L_5 and L_6 are separated by a distance equivalent to the sum of their focal lengths, then the beacon image will be placed at infinity. For beam wave considerations this is equivalent to being outside the Rayleigh range of the beam exitting L_6. With this arrangement a large image size

can be obtained merely by going sufficiently far, d_7, from the beam waist at d_5. The large image size is desirable because we would like to fill about half of the quadrant detector's active area.

If the active region of the detector is approximately 0.4 in. in diameter, then at one Rayleigh range from the waist of the beam from M_2 we desire an image about 0.2 in. in diameter. This requires that

$$\theta_F = \frac{0.2}{Z_R} \tag{79}$$

where θ_F is the full angle subtended by the image for the one Rayleigh range, Z_R, from the waist. But inherently, θ_F is defined by diffraction and the waist size at d_5, such that

$$\theta_F \simeq \frac{\lambda}{\pi d_o} \tag{80}$$

Further, the waist, d_o, is defined by the diameter of the beam exitting M_2 at L_6, is,

$$d_o \sim \frac{2\lambda L}{d_6} \tag{81}$$

where d_6 is given by

$$d_6 = d_2 M_2 \tag{82}$$

and d_2 is the initial beam diameter entering M_2. Combining Eqs. 80, 81, and 82 we see that for the nominal $d_2 = 1/8$ in. that $M_2 = 10$. This receiver is now sufficiently flexible to place the image at any convenient position along the optical bench.

D.3. Basic Steering

The 2-dimensional steering of the tracking system is implemented with the use of two galvanometrically driven scanner mirrors. Their responsivity is approximately $R_{scan} = 1.4 \times 10^{-1}$ (rad/volt). But since these are mirror-type scanners, the output angle will be twice the actual scanned angle. Hence, the compound responsivity is $R_{opt} = 2.8 \times 10^{-1}$ (rad/volt).

Finally, the transmitting angle will be given by

$$R'_{opt} = \frac{2.8 \times 10^{-1}}{M_1} \text{ (rad/volt)} = 5.6 \times 10^{-3} \text{ (rad/volt)} \qquad (83)$$

D.4. Transfer Function Constants

In the design Section B, two of the important constants were not available. The preceding analysis provides sufficient data to define D_1, D_2 and D_3.

Constant D_3 is just the sensitivity of the scanners as referred through the transmitting telescope. Hence, from Eq. 83

$$D_3 = \frac{1}{R'_{opt}} = 1.79 \times 10^{2} \text{ (volt/rad)} \qquad (84)$$

Next, D_2 is just the responsivity of the quadrant detector: 0.4 amp/watt.

At last, we find D_1 by

$$D_1 = P' M_1 M_2 d_8 r_2 \qquad (85)$$

where P' is the energy density of the image on the detector. If

$$P' = \frac{P_{o_{min}}}{\pi r_2^2} \tag{86}$$

then $$D_1 = 1.27 \times 10^{-2} \quad .$$

From Section B we obtained the expression

$$2\pi\,(20H_z) = \frac{R_F D_1 D_2}{R_2 C_2 D_3} \tag{87}$$

We now have sufficient data to observe that $R_2C_2 = 2.82$ s. With the choice of $C_2 = 10\mu f$, $R_2 = 2.82 \times 10^5\,\Omega$. However, gains can be adjusted at will to provide a wide range of time constants to work with. A complete schematic of the tracking transmitter electronics is given in Fig. 71.

E. Performance

Measurements on the completed system indicate that the noise limited tracking angle is about 2% of the diffraction width of the transmitter beam. This will be sufficient resolution to perform the experiments of Chapter III.

Fig. 72 is an example of the difference signal for the up and the down quadrants, contrasting the tracked and the non-tracked beacon image wander. Figs. 32, 36 and 40 indicate the qualitative effect on target signals when this system is used to cancel beam wander. The quantitative advantages are explained in Section III.C.

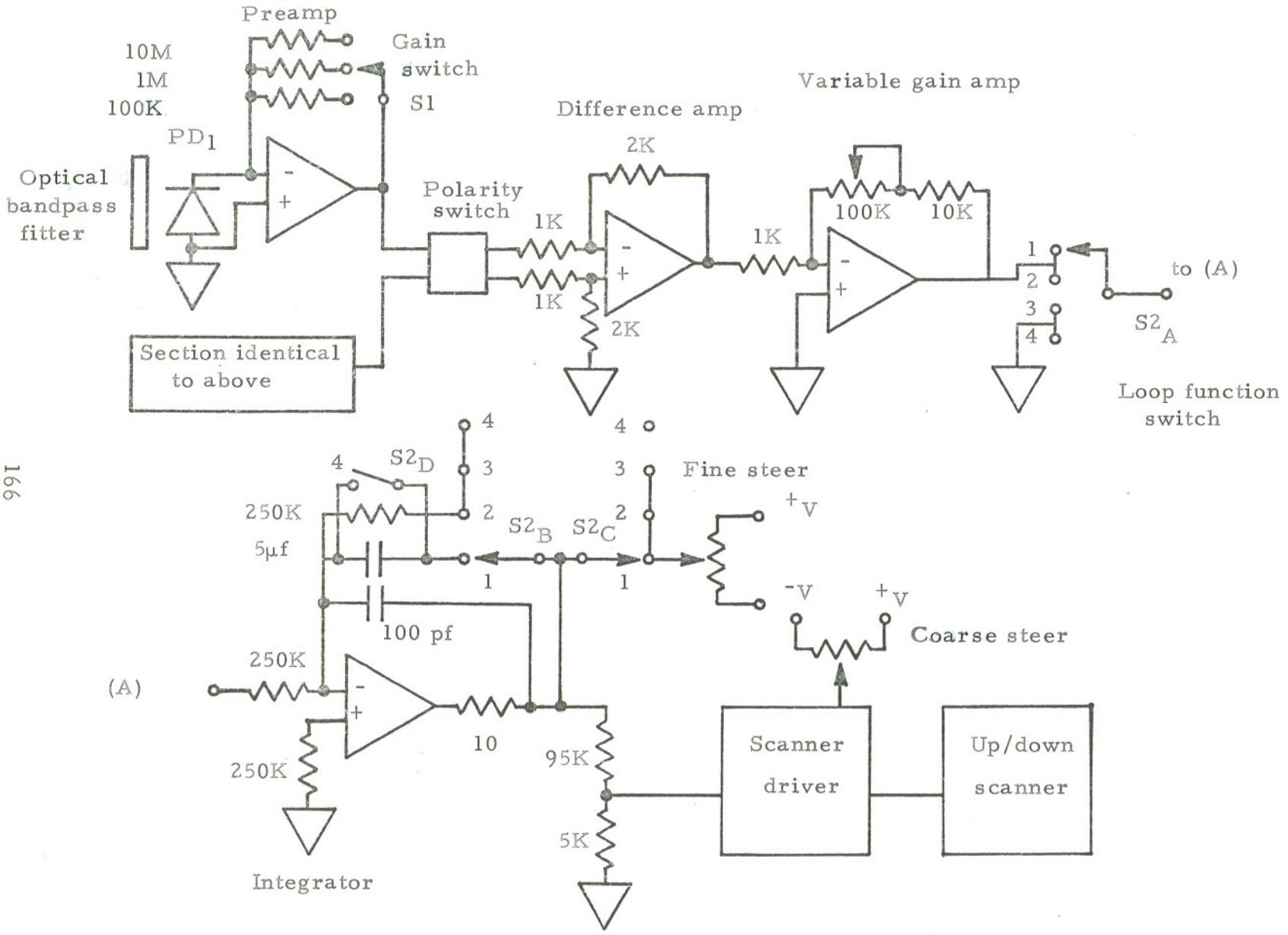

Figure 71. Complete electronics schematic of the tracker (vertical axis).

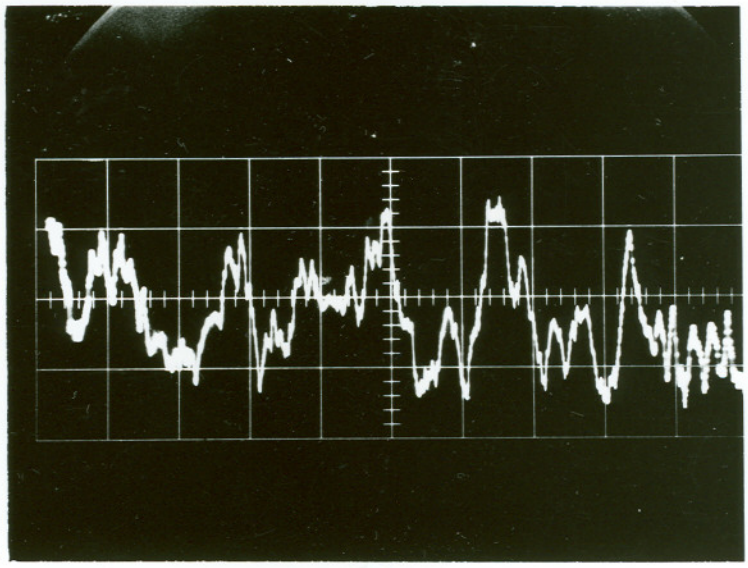

(A)

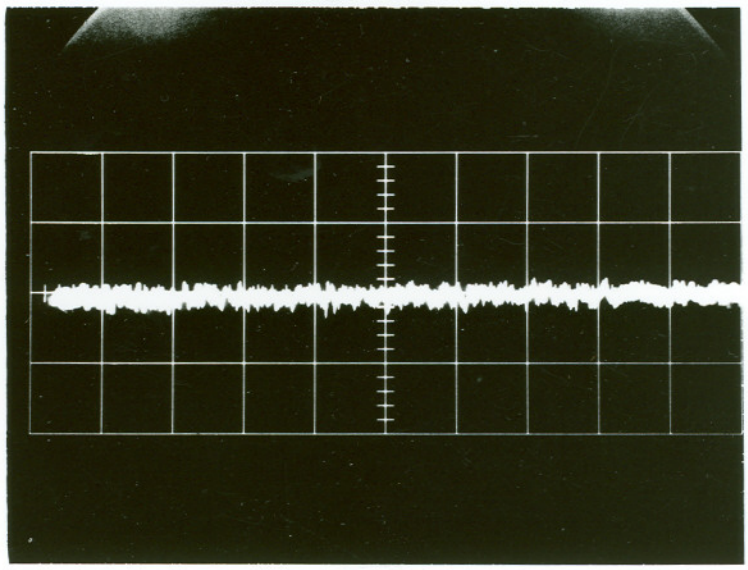

(B)

Figure 72. Difference signal from the up and down quadrants of the quadrant detector for tracking out wander (B) and no tracking (A) with a low pass filter function reducing high frequency fluctuations (f_{co} = 10 Hz) due to scintillation. Abscissa: 2 sec/div.

REFERENCES

1. M. Schwartz. Information Transmission, Modulation, and Noise: a Unified Approach to Communication Systems. 2nd ed. (McGraw-Hill, New York, 1970).

2. M. Ross. Laser Receivers: Devices, Techniques, Systems. (John Wiley & Sons, New York, 1966).

3. C.E. Shannon, Proc. I.R.E. 37, 10 (1949).

4. D.L. Fried and R.A. Schmeltzer, Appl. Opt. 6, 1729 (1967).

5. J.C. Hancock and P.A. Wintz. Signal Detection Theory. (McGraw-Hill, New York, 1966).

6. W.P. Brown, Jr., "Wave Propagation and Multiple Scattering in Random Media," Addendum to Final Report, Contract No. AF 49 (638)-1607, United States Air Force, Office of Scientific Research, Arlington, Virginia 22209, 1972.

7. R.B. Muchmore and A.D. Wheelon, Proc. IRE 43, 1437 (1950).

8. L.A. Chernov, Wave Propagation in aRandom Medium (McGraw-Hill, New York, 1960).

9. V.I. Tatarskii, Wave Propagation in a Turbulent Medium (McGraw-Hill, New York, 1961).

10. V.I. Tatarskii, The Effects of the Turbulent Atmosphere on Wave Propagation (Nauka, Moscow, 1967), Trans. U.S. Department of Commerce National Technical Information Service, Springfield, Va.

11. J.W. Strohbehn, Proc. IEEE 56, 1301 (1968).

12. R.S. Lawrence and J.W. Strohbehn, Proc. IEEE 58, 1523 (1970).

13. D.L. Fried and J.D. Cloud, JOSA 56, 1667 (1966).

14. D.L. Fried, J. Opt. Soc. Am., 57, 175 (1967)

15. D.A. deWolf, J. Opt. Soc. Am., 58, 461 (1968)

16. J.R. Kerr, J.Opt.Soc.Am. 62, 1040 (1972).

17. J.R. Kerr, "Multiwavelength Laser Propagation Study --II", Quarterly Progress Report No. 2, Contract N00014-68-0461-0001, monitored by the Office of Naval Research for the Advanced Research Projects Agency (ARPA Order No. 306), Department of Defense, Washington, D.C., 20301, January, 1970.

18. J.R. Dunphy and J.R. Kerr, J.Opt.Soc.Am., 63, 981 (1973).

19. V.I. Tatarskii and M.E. Gertsenshtein, Soviet Physics--JETP (USSR) 44, 676 (1963).

20. V.I. Tatarskii, Soviet Physics--JETP (USSR) 46, 1399 (1964).

21. W.P. Brown, Jr., IEEE Trans. Antennas Propagat. AP-15, 81 (1967).

22. D.A. deWolf, Radio Sci. 2, 1379 (1967).

23. D.A. deWolf, J.Opt.Soc.Am., 59, 1455 (1969).

24. D.A. deWolf, "Effect of Turbulence Instalibilities on Laser Propagation," Technical Report RADC-TR-72-204, Rome Air Development Center. Griffiss Air Force Base, New York, July 1972.

25. D.A. deWolf, J.Opt.Soc.Am. 63, 171 (1973).

26. M.I. Sancer and A.D. Varvatsis, JOSA 60, 654 (1970).

27. W.P. Brown, Jr., J.Opt.Soc.Am. 61, 981 (1971).

28. W.P. Brown, Jr., J. Opt.Soc.Am., 62, 45 (1972).

29. W.P. Brown, Jr., J. Opt.Soc.Am., 62, 966 (1972).

30. A.M. Whitman and M.J. Beran, J.Opt.Soc.Am., 60, 1595 (1970).

31. V.I. Tatarskii, Soviet Physics--JETP (USSR) 56, 2106 (1969).

32. V.I. Klyatskin and V.I. Tatarskii, Soviet Physics--JETP (USSR) 58, 624 (1970).

33. J.W. Strohbehn, and T.I. Wang, J. Opt.Soc.Am., 62, 1061 (1972).

34. H.T. Yura, Appl. Opt. 11, 1399 (1972).

35. R.F. Lutomirski and H.T. Yura, Appl. Opt. 10, 1652 (1971).

36. D.S. Bugnolo, J. Appl. Phys. 31, 1176 (1960).

37. R.L. Fante, IEEE Trans. Antennas Propagat. AP-21, 687 (1973).

38. V.I. Tatarskii, Soviet Physics--JETP (USSR) 49, 1518 (1965).

39. A. Ishimaru, IEEE Trans. Antennas and Propagat. AP-21, 47 (1973).

40. D.J. Torrierri and L. S. Taylor, J.Opt.Soc.Am. 62, 145 (1972).

41. J.R. Kerr, J.Opt.Soc.Am. 62, 916 (1972).

42. A.T. Young, Astron. J. 72, 747 (1967).

43. A.T. Young, J.Opt.Soc.Am. 60, 248 (1970).

44. A.T. Young, J.Opt.Soc.Am. 60, 1495 (1970).

45. H.T. Yura, J.Opt.Soc.Am. 62, 889 (1972).

46. R.L. Fante and J.L. Poirier, Appl. Opt. 12, 2247 (1973).

47. Note that Eq. (T13) of Ref. 12 has an incorrect coefficient. The correct value is 2.24.

48. J.C. Wyngaard, Y. Izumi, and S.A. Collins, Jr., J.Opt.Soc.Am. 61, 1646 (1971).

49. R.H. Kleen and G.R. Ochs, J.Opt.Soc.Am. 60, 1695 (1970).

50. H.T. Yura, Aerospace Corp., Los Angeles, Calif., private communication.

51. H.R. Carlon, Appl. Opt. 4, 1089 (1965).

52. M.E. Gracheva, A.S. Gurvich, S.S. Kashkarov, and V.V. Pokasov, "Similarity Correlations and Their Experimental Verification in the Case of Strong Intensity Fluctuations of Laser Radiation," (Akademia Nauk USSR, Otdelenie Oceanalogii Fiziki, Atmosfery i Geografii, Russian preprint Moscow, 1973). English translation available from the Literature Research Group, The Aerospace Corp., Library Services, No. LRG-73-T-28.

53. S.F. Clifford, et al., J.Opt.Soc.Am. 64, 148 (1974).

54. H.T. Yura, J.Opt.Soc.Am. 64, 59 (1974).

55. H.T. Yura, "Irradiance Fluctuations of a Spherical Wave Propagating under Saturation Conditions," Electronics Research Laboratory, The Aerospace Corporation, Los Angeles, Calif., preprint, May 1974.

56. H.T. Yura, J.Opt.Soc.Am. 64, 357 (1974).

57. S.F. Clifford and H.T. Yura, "Physical Equivalence of Two Theories of Strong Optical Scintillation," a paper presented at OSA Conference on Optical Propagation Through Turbulence, Boulder, Colo., July 1974.

58. H.T. Yura, "Supersaturation: effect of a high frequency cutoff on strong optical scintillation measurements," The Aerospace Corporation, Los Angeles, Calif., preprint, May 1974.

59. D.A. deWolf, "Waves in Turbulent Air: A Phenomenological Model," RCA Laboratories, Princeton, N.J., preprint, Jan. 1974.

60. D.A. deWolf, "Waves in Turbulent Air: New Results and Modelling," RCA A paper presented at OSA Conference on Optical Propagation through Turbulence, Boulder, Colo., July 1974.

61. D.A. deWolf, J.Opt.Soc.Am. 63, 1249 (1973).

62. D.A. deWolf, J.Opt.Soc.Am.64, 360 (1974).

63. T. Wang and J.W. Strohbehn, J.Opt.Soc.Am. 64, 583 (1974).

64. J.W. Strohbehn, T. Wang and G.E. Homstad, "Probability Distributions and Aperture Averaging Effects in Optical Scintillations," a paper presented at OSA Conference on Optical Propagation through Turbulence, Boulder, Colo., July 1974.

65. R.L. Fante, J.Opt.Soc.Am. 64, 592 (1974).

66. A. Ishimaru, Proc. IEEE 57, 407 (1969).

67. A. Ishimaru, Radio Sci. 4, 295 (1969).

68. J.R. Kerr and R. Eiss, J.Opt.Soc.Am. 62, 682 (1972).

69. F.P. Carlson, J.Opt.Soc.Am. 59, 1343 (1969).

70. D.L. Fried and J.B. Seidman, J.Opt.Soc.Am. 57, 181 (1967).

71. Y. Kinoshita, T. Asakura, and M. Suzuki, J.Opt.Soc.Am.58,1040 (1968).

72. R.W. Lee and J.C. Harp, Proc. IEEE 57, 375 (1969).

73. D.L. Fried, Appl. Opt. 10, 721 (1971).

74. J.R. Kerr, "Propagation of Multiwavelength Laser Radiation Through Atmospheric Turbulence," Technical report: RADC-TR-73-54, Rome Air Development Center, Griffiss Air Force Base, N.Y., January 1973.

75. J.R. Kerr and J.R. Dunphy, J.Opt.Soc.Am. 63, 1 (1973).

76. R.L. Mitchell, J.Opt.Soc.Am. 58, 1267 (1968).

77. J.R. Kerr and J.R. Dunphy, "Propagation of Multiwavelength Laser Radiation through Atmospheric Turbulence," Technical Report: RADC-TR-74-183, Rome Air Development Center, Air Force Systems Command, Griffiss Air Force Base, New York, May 1974.

78. J.R. Dunphy and J.R. Kerr, J. Opt. Soc. Am., 64, 1015 (1974).

79. D.L. Fried and H.T. Yura, J.Opt.Soc.Am. 62, 600 (1972)

80. H.V. Hance and D.L. Fried, J. Opt. Soc.Am. 63, 1015 (1973).

81. R.F. Lutomirski and R.G. Buser, Appl. Opt. 12, 2153 (1973).

82. R.E. Hufnagel and N.R. Stanley, J.Opt.Soc.Am. 54, 52 (1964).

83. J.W. Goodman, Introduction to Fourier Optics (McGraw-Hill, New York, 1968).

84. T.A. Brackey, "Application of Spatial Diversity to Atmospheric Optical Line-of-Sight Communications Systems," Technical Report 2156-12, Air Force Avionics Lab., Air Force Systems Command, Wright-Patterson AFB, Ohio, October 1969.

85. T. Chiba, Appl. Opt. 10, 2456 (1971).

86. Z.I. Feizulin and Y.A. Kravtsov, Izvestiya VUZ. Radiofizika, 10, No. 1, 68 (1967).

87. A.I. Kon, Izvestiya VUZ. Radiofizika, 13, No.1, 66 (1970).

88. D.A. deWolf, "Effects of Turbulence Instabilities on Laser Propagation," Technical Report: RADC-TR-71-249, Rome Air Development Center, Air Force Systems Command, Griffiss Air Force Base, N.Y., October 1971.

89. P. Beckmann, Radio Sci. 69D, 629 (1965).

90. H. Hodara, Proc. IEEE 54, 368 (1966).

91. H. Hodara, Proc. IEEE 56, 2130 (1968).

92. A.D. Varvatsis and M.I. Sancer, Canadian J. Phys. 49, 1233 (1971).

93. D.A. deWolf, "Effects of Turbulence Instabilities on Laser Propagation," Technical Report: RADC-TR-72-204, Rome Air Development Center, Air Force Systems Command, Griffiss Air Force Base, N.Y., July 1972.

94 D.L. Fried, J.Opt.Soc.Am. 56, 175 (1966).

95. R.A. Muller and A. Buffington, "Real-time Correction of Atmospherically Degraded Telescope Images Through Image Sharpening," preprint, January 1974.

96. J.R. Kerr, "Propagation of Multiwavelength Laser Radiation through Atmospheric Turbulence," Technical Report: RADC-TR-73-322, Rome Air Development Center, Air Force Systems Command, Griffiss Air Force Base, N.Y., August 1973.

97. K. Furutsu, J.Opt.Soc.Am. 62, 240 (1972).

98. P.J. Titterton, Appl. Opt. 12, 423 (1973).

99. D.L. Fried, Appl. Opt. 12, 422 (1973).

100. J.A. Dowling and P.M. Livingston, J. Opt. Soc.Am. 63, 846 (1973).

101. J.W. Strohbehn, IEEE Trans.Antennas and Propagat. AP-22, 303 (1974).

102. S.F. Clifford, J. Opt. Soc. Am. 61, 1285 (1971).

103. L.R. Zintsmaster and S.A. Collins, Jr., "Angle of Arrival Calculations at 10.6 μm," Technical Report: RADC-TR-71-124, Rome Air Development Center, Air Force Systems Command, Griffiss Air Force Base, N.Y., June 1971.

104. A.J. Huber, "Measurements of the Temporal Power Spectra of a Propagated 10.6 Micron Wavefront," a thesis, Rome Air Development Center, Griffiss AFB, N.Y., 1973.

105. S.A. Collins, private communication.

106. Rheinhardt and S.A. Collins, "Laser Propagation Temporal Spectra," Technical Report: RADC-TR-73-66, Rome Air Development Center, Air Force Systems Command, Griffiss Air Force Base, N.Y., February 1973.

107. H.T. Yura, J.Opt.Soc. Am. 63, 567 (1973).

108. D.L. Fried, J.Opt.Soc. Am. 55, 1427 (1965).

109. G.O. Olaofe, J.Opt.Soc.Am. 60, 1654 (1970).

110. P.J. Titterton, et al., "Optical Propagation Tests Study," Technical Report: AFAL-TR-72-307, Air Force Avionics Laboratory, Air Force Systems Command, Wright-Patterson Air Force Base, Ohio, September 1972.

111. G.R. Heidbreder and R.L. Mitchell, "The Effect of a Turbulent, Medium on a Wavefront Tracking Circular Aperture," preprint.

112. R.F. Lutomirski, "The Tilt Corrected MTF," preprint.

113. G.R. Heidbreder, IEEE Trans. Antennas and Propagat. AP-15, 90 (1967).

114. D.L. Fried, IEEE J. Quantum Elect. QE-3, 213 (1967).

115. R.E. Warren, "Scintillation of Arbitrary Optical Beams in a Weakly Random Medium" Technical Report: AFAL-TR-73-372, Air Force Avionics Laboratory, Air Force Systems Command, Wright-Patterson Air Force Base, Ohio, October 1973.

116. D.L. Fried, "Effects of Atmospheric Turbulence on Static and Tracking Optical Heterodyne Receivers/Average Antenna Gain and Antenna Gain Variation," Technical Report: No. TR-027, Optical Science Consultants, Yorba Linda, Calif., August 1971.

117. V.A. Banakh, et al., J.Opt.Soc.Am. 64, 516 (1974).

118. D.L. Fried and G.E. Mevers, "Evaluation of r_o for Propagation Down Through the Atmosphere," Technical Report: No. TR-120, Optical Science Consultants, Yorba Linda, Calif., November 1973.

119. J.P. Titterton, "Beam Spread Statistics from Reciprocity," paper presented at OSA Special Topical Meeting on Optical Propagation through Turbulence, Boulder, Colo., July 1974.

120. A.L. Buck, Appl. Opt. 6, 703 (1967).

121. S.S. Khmelevtsov, Appl. Opt. 12, 2421 (1973).

122. P.M. Livingston, private communication.

123. T.J. Gilmartin and J.Z. Holtz, "Focused Beam and Atmospheric Coherence Measurements at 10.6 μm and 0.63μm ," preprint, M.I.T. Lincoln Laboratory, Lexington, Massachusetts, October 1973.

124. D.P. Greenwood and D.O. Tarazano, "A Proposed Form for the Atmospheric Microtemperature Spatial Spectrum in the Input Range," Technical Report: RADC-TR-74-19, Rome Air Deveoopment Center, Air Force Systems Command, Griffiss Air Force Base, N.Y., February 1974.

125. P.J. Titterton, J. Opt.Soc.Am.,63,439 (1973).

126. R.S. Lawrence, G.R. Ochs, and S.F. Clifford, J.Opt.Soc.Am.,60,826(1970).

127. D.L. Fried, private communication.

128. J.H. Dunn, D.D. Howard, and A.M. King, Proc. IRE 47, 855 (1959).

129. R.H. Delano, Proc. IRE 41, 1778 (1953).

130. R.B. Muchmore, IRE Trans. Antennas and Propagat. 48, 201 (1960).

131. L. Peters,Jr., and F.C. Weimer, IRE Trans. Antennas and Propagat. AP-9, 110 (1961).

132. R.B. Muchmore, IRE Trans. Antennas and Propagat. AP-9, 112 (1961).

133. R.F. Lutomirski, "A Model for the Atmospheric Distortions in a Laser-Retro-Receiver Configuration," Technical Report: PSR Note 53, Pacific Sierra Research Corp., Santa Monica, Calif., April 1974.

134. A. Consortini, G. Fidanzati, A.Mariani, and L. Ronchi, Appl. Opt. 11, 1229 (1972).

135. J. Smith, T.H. Pries, K.J. Skipka and M.A. Hamiter, J.Opt.Soc. Am. 62, 1183 (1972).

136. J. Smith, J.Opt.Soc.Am. 63, 1095 (1973).

137. J.H. Shapiro, J.Opt.Soc.Am. 61, 492 (1971).

138. D.L. Fried and H.T. Yura, Proc. IEEE 62, 600 (1972).

139. D.M. Chase, J.Opt.Soc.Am. 56, 33 (1966).

140. H.V. Hance and D.L. Fried, J.Opt.Soc.Am. 63, (1973).

141. W.P. Brown, "Research in Interaction of Coherent Light with Solids and with Turbulent Atmospheres," Final Scientific Report, Contract, F44620-71-C-0048, Air Force Office of Scientific Research, Air Force Systems Command, Arlington, Virginia 22209, May 1972.

142. J.A. Aseltine, Transform Method in Linear System Analysis (McGraw-Hill, New York, 1958).

143. D.L. Fried, "Optical Propagation Measurements at Emerson Lake," Final Report on Contract NAS 1-7705, for Langley Research Center, Autonetics, North American Rockwell, Anaheim, Calif., 1968.